Magnetic Tweezers for Force-extension Measurements

by

Luis Ramírez-Ramírez

B.Sc., University of Costa Rica, 2021

Thesis Submitted in Partial Fulfillment of the
Requirements for the Degree of
Master of Science

in the
Department of Physics
Faculty of Science

SIMON FRASER UNIVERSITY
Fall 2024

Declaration of Committee

Name:	**Luis Ramírez-Ramírez**
Degree:	**Master of Science**
Title:	**Magnetic Tweezers for Force-extension Measurements**
Committee:	**Chair:** **Gopolang Mohlabeng** Assistant Professor, Physics
	Nancy Forde Supervisor Professor, Physics
	John Bechhoefer Committee Member Professor, Physics
	Erol Girt Examiner Professor, Physics

Abstract

In this thesis, I establish the foundational methods for conducting single-molecule force experiments on biopolymers using Magnetic Tweezers (MT). By integrating MT with Total Internal Reflection Fluorescence (TIRF) microscopy and precise temperature control, as a research group we aim to explore the interplay between mechanical forces, temperature variations, and molecular processes such as binding dynamics. A key achievement of this work is the enhancement of bead-height position analysis, accomplished through modifications to existing algorithms and improvements in sample illumination. These advances are essential for accurately monitoring the mechanical response of biopolymers such as DNA and collagen under tension, thereby providing deeper insights into their behavior. The methods developed in this thesis lay the groundwork for future investigations into the complex interactions and environmental influences on biopolymers at the single-molecule level, with the potential to significantly advance our understanding of these fundamental biological processes.

Keywords: Magnetic Tweezers; Force-extension; Single-molecule; Biopolymers; DNA

Acknowledgements

First and foremost, I extend my deepest gratitude to my supervisor, Nancy, whose passion for conducting rigorous yet accessible science never stop surprising me. Thanks for your patience and guidance throughout these years. Your humility and kindness as a scientist are qualities that not only inspire me but should serve as an example for anyone in science.

To my lab mates: Kosuhik, who has been more than a friend—a true brother—reminding me of what truly matters in life; Alaa, a remarkable model of resilience in so many ways; and Janine, our chemist, who was always willing to assist with tethering experiments and whose scientific rigor continually pushed me to grow. To the rest of you, with such bright and inspiring minds that I still find it hard to believe I had the privilege to meet and work alongside: Alyssa, Karmen, Daniel, Juliette, Jody, Shetal, Michael, Ryan, and Nik—thank you for making this journey so enriching.

To Eric Lin, I am incredibly grateful for teaching me not only about optics and instrumentation but also about the nuances and challenges of the academic environment.

To my friends, from whom I have learned so much—your shared laughter and moments of frustration helped me forget the difficulties and made this journey possible.

To my family, the unwavering foundation upon which all of my achievements rest—thank you for your constant support and love.

Finally, to all the people who fight every day against injustice and oppression, striving for a better future for everyone, not just for themselves, even when the path ahead seems dark—your resilience and dedication inspire me more than words can express.

Table of Contents

List of Figures

List of Acronyms

AFM	Atomic Force Microscope
AFS	Acoustic Force Spectroscopy
BSA	Bovine Serum Albumin
CFM	Centrifuge Force Microscopy
COM	Center of Mass
eWLC	Extensible Worm-Like Chain
FFT	Fast Fourier Transform
FJC	Freely Jointed Chain
FRAP	Fluorescence Recovery after Photobleaching
FRET	Fluorescence Resonance Energy Transfer
MAGIC	Microsphere Adhesion by Gravity, Inversion, then Counting
MHT	Multiple Hypothesis Tracking
MINFLUX	Minimal Fluorescence Photon Fluxes Microscopy
MLE	Maximum-Likelihood Estimation
MT	Magnetic Tweezers
NPC	Nuclear Pore Complex
OT	Optical Tweezers
PALM	Photoactivated Localization Microscopy
PSF	Point Spread Function
QPD	Quadratic Photodiode
RMS	Root Mean Square
ROI	Region of interest
SA	Succinic Anhydride
SPDP	Succinimidyl 3-(2-pyridyldithio)propionate
STED	Stimulated Depletion Microscopy
STORM	Stochastic Optical Reconstruction Microscopy
TIRF	Total Internal Reflection Fluorescence
WLC	Worm-Like Chain

Chapter 1. Introduction

In this thesis, I establish the groundwork to perform single-molecule force experiments on biopolymers using Magnetic Tweezers (MT). Through the integration of MT, Total Internal Reflection Fluorescence (TIRF) microscopy, and precise temperature control, we want to study the interplay between mechanical forces, temperature variations, and molecular processes like binding dynamics. My primary focus lies in the implementation of MT, a technique that is used to mechanically probe biopolymers[1–6]. In our experiments, we seek to use MT to exert tension on thread-like biomolecules such as DNA and collagen, tracking their behavior under such mechanical stress.

1.1. Biophysics

Biophysics studies the intricate interplay between biological systems and the fundamental principles of physics. The insights gathered from this field have not only deepened our understanding of life at its molecular and cellular levels but have also served as catalysts for revolutionary advances in fields such as medicine, biotechnology, material science, and beyond. From the discovery of the double-helical structure of DNA[7,8] by Rosalind Franklin, Watson, and Crick to the revelation of quantum coherence phenomena in photosynthesis[9,10], biophysics has provided the scientific community with profound insights into the mechanisms governing life itself. Through rigorous experiments, theory, and computational modeling, biophysicists have uncovered the secrets of biomolecular interactions, cellular mechanics, and the dynamics of living organisms. For example, biophysics approaches enabled the study of how molecular-scale forces underlie all types of biological motion and structure[3,11–18], which is also a focus of studies in our laboratory specifically with collagen. Expanding this biophysics knowledge will continue shaping our understanding of the natural world.

1.1.1. Collagen

Collagen, a thread-like structural protein, is a fundamental component of the extracellular matrix in various tissues throughout the human body. Constituting a large part of the body's total protein content (15% to 17% according to Tarnutzer *et al.*[19]), the significance of this molecule lies in its ability to provide tensile strength, resilience, and

structural integrity to many tissues such as skin, bones, tendons, and cartilage. Collagen molecules possess a unique triple-helix structure composed of three α chains, each with an amino acid sequence of primarily Glycine-X-Y, where X and Y represent any amino acid. Frequently, X and Y are proline and hydroxyproline[12,20,21], as shown in Figure 1-1. Beyond its structural functions, collagen is also involved in cell signaling and regulation, contributing to processes like wound healing[22], cell adhesion[23], and tissue development[24]. The diversity of collagen types (more than 28[12,21,25,26]), each with distinct tissue distributions and functional roles, emphasizes its significance in a wide variety of physiological processes.

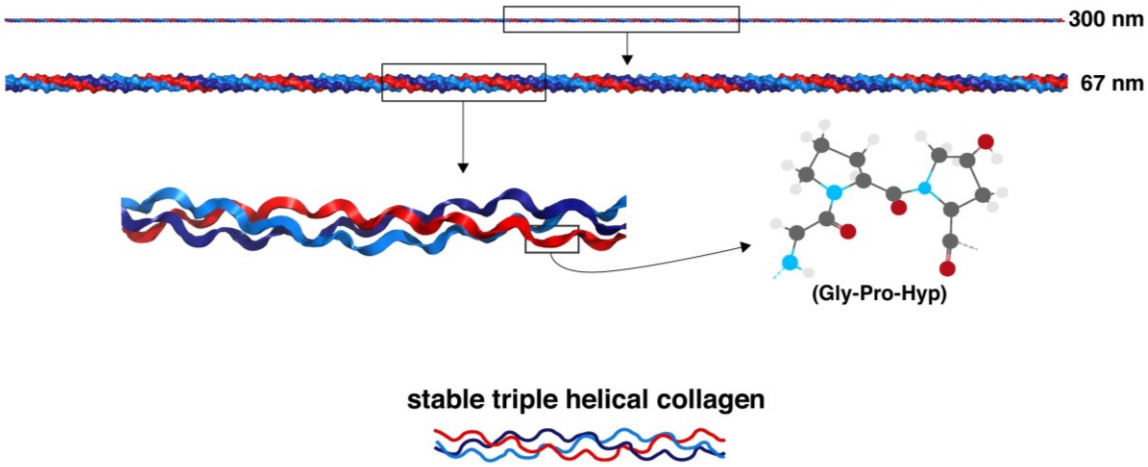

Figure 1-1 Collagen structure.
This figure shows collagen structure at different scales: the triple helix (tertiary structure) of three α chains (secondary structure), and a tripeptide sequence glycine-proline-hydroxyproline (primary structure). The full-length structure of collagen type I is 300 nm long.[1]

Studying collagen presents a variety of experimental challenges, including its size, lack of solubility, tendency for self-association, hierarchical organization, and out-of-equilibrium dynamics[21,27–29]. These obstacles hinder single-molecule collagen studies and limit the application of many biochemical and biophysical methods, leaving critical aspects of collagen's mechanisms poorly understood. Because of these limitations, researchers have used collagen-related peptides (CRPs)—shorter model peptides—to determine its structure[12,21,30,31].

[1] Reprinted from Current Opinion in Chemical Biology, Vol 53, M Kirkiness, K Lehmann, N Forde, Mechanics and structural stability of the collagen triple helix, Pages No. 98-105, Copyright (2019), with permission from Elsevier.

One of the most relevant aspects of collagen in our bodies lies in its mechanical functions; nevertheless, collagen mechanics are still poorly understood. While some characteristics of collagen mechanics are known, they primarily rely on bulk measurements focusing on collagen fibrils or collagen embedded in tissue. These investigations aim to uncover important mechanical characteristics such as Young's modulus, and fracture strength, observed[32–34] or simulated[35] under various conditions.

Single-molecule mechanics of collagen are less well characterized. Studies on bending flexibility, for example, have yielded inconsistent results in terms of persistence length[12,36]. Twist elasticity remains largely unexplored, with only indirect inferences drawn from stretch-twist coupling mechanisms[12,16]. Extensibility has had more attention, but studies have been done predominantly under low forces (<10 pN)[37–41]. An aspect of collagen mechanics that is an ongoing debate and involves studies in our laboratory is the impact of force on collagen's triple helix: while some findings suggest force enhances its rate of cleavage[42–44], others report the opposite[16]. Mechanical deformations of collagen have been studied through molecular dynamics simulations[45,46], but there is still very little experimental characterization. Additionally, collagen's behavior is heavily influenced by factors such as environmental acidity, tension, collagen type, temperature, and others[12,28,36,47–50]. However, there are still many aspects to understand on how these factors—like temperature—affect collagen behavior[28], especially on a single molecule level. This incomplete understanding of molecular collagen leaves an opportunity for investigation and discovery of its mechanics, which will offer relevant insights into how it behaves and how it provides its physiological functions.

Our research team focuses on examining the mechanical features of collagen at different scales. For example, single-molecule imaging experiments using Atomic Force Microscopy (AFM) [36,47] have demonstrated variations in the bending flexibility, characterized by a change in the persistence length along collagen. These variations depend on the sequence, particularly evident in collagen IV, where regions with interruptions in the (Gly-X-Y) pattern exhibit greater flexibility[47]. The development of a Centrifuge Force Microscope (CFM) in our laboratory allowed the study of collagen's proteolytic susceptibility by measuring thousands of collagen molecules in just a few experiments[42]. Additionally, investigations into collagen using microrheology methods revealed that telopeptides play a role in facilitating transient intermolecular interactions

among collagen proteins,[40,51–53] and have shown how the viscoelastic properties vary between collagen molecules and fibrillar collagen[40,53,54].

Collagen research continues to yield insights into different applications[55] such as clinical trials using collagen[25], biological materials[56], tissue engineering[57], regenerative medicine[58], and age-related diseases[59], making it a focal point of interest in biological, materials, and biomedical sciences. Our research group aims to continue contributing to the expanding understanding of collagen by conducting novel single-molecule studies. Using advanced biophysics techniques, we seek to observe the binding dynamics of other molecules to collagen under different forces and temperatures, which could elucidate aspects of the mechanisms of regulatory proteins and collagen itself.

1.1.2. Biophysics techniques

In recent years, the field of biophysics has generated advances in the development of innovative tools and techniques that enable researchers to study biological systems in greater detail. Among these tools, many single-molecule techniques have revolutionized our understanding of molecular structure and dynamics by enabling the observation and manipulation of individual molecules.

Imaging and force spectroscopy methods are indispensable tools in experimental biophysics to reveal different mechanisms. On one hand imaging techniques, such as AFM and fluorescence microscopy, allow the visualization of biological structures and processes at high resolution[60–62]. These techniques let us study the spatial organization of biomolecules, dynamic interactions within cellular environments, and structural changes during biochemical processes. On the other hand, force spectroscopy techniques, including optical tweezers (OT), MT, and AFM force spectroscopy provide means to manipulate, apply, and measure mechanical forces while tracking molecular responses at the single-molecule level[3,63–65].

1.2. Imaging techniques

AFM is one of the most versatile and high-resolution techniques to visualize and mechanically probe surface-supported samples at the nanometer scale. It is mainly used to study morphology and topology of a sample, revealing insights into biomolecular

structures and mechanisms[3]. This technique uses a sharp tip mounted on a flexible cantilever, and by moving this probe across the sample surface, AFM detects small forces between the probe and the specimen, such as van der Waals forces or electrostatic interactions. When the tip interacts with the sample, it causes the cantilever to deflect. This deflection is measured by a laser that reflects off the back of the cantilever and is detected by a quadratic photodetector (QPD).

AFM has been used to study different biological samples. In the case of collagen, for example, it has enabled us to see the sub-fibrillar structure of collagen[66], study the thermal denaturation of collagen fibrils,[67] and map the bending stiffness along a fibril-forming collagen molecule (collagen III, shown in Figure 1-2, measured in our group[47]).

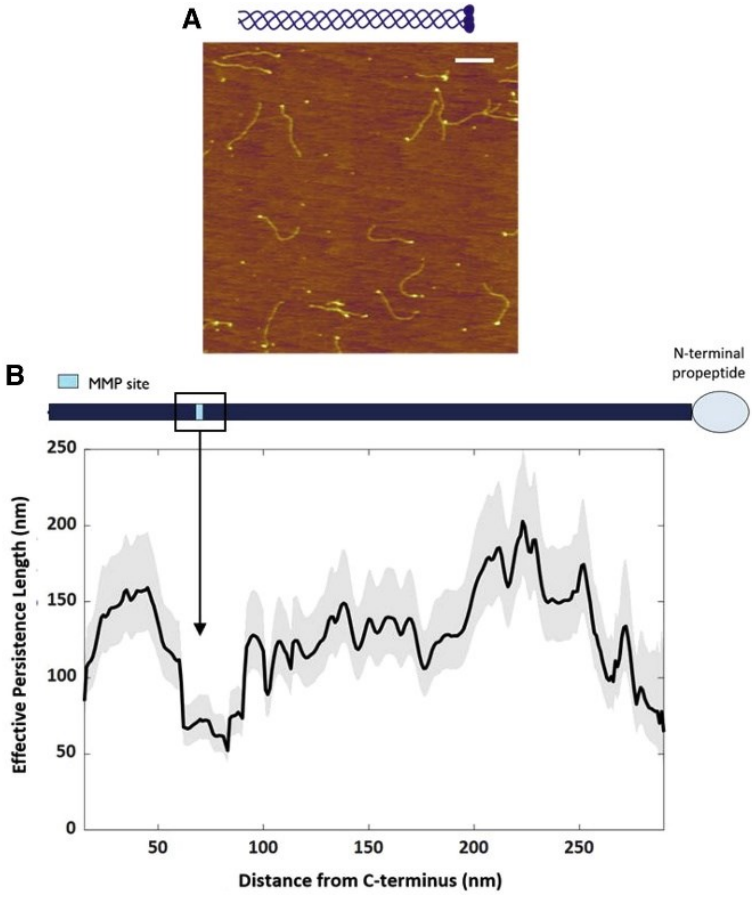

Figure 1-2 Collagen AFM image.
A) AFM image of bovine collagen pN-III proteins, indicated schematically above. The scale bar is 200 nm. B) Position-dependent persistence length, demonstrating that one region of the triple

helix (the so-called MMP site, important for collagen remodeling) is more flexible than the rest of the triple helix.[2]

Optical microscopy is the most common approach for imaging biophysical systems at the molecular and cellular levels. From bulk visualization to single-molecule analysis, optical microscopy spans a wide range of temporal and spatial dimensions. However, when conventional optical microscopy is used to examine nanoscale molecules, it is constrained by the diffraction limit, which is in the order of hundreds of nanometers, restricting its resolution[68]. This limit is defined by the Abbe diffraction limit:

$$\mathrm{d} = \frac{\lambda}{2\mathrm{n}\sin\theta}. \qquad [1]$$

Here, λ is the wavelength of the light, n is the index of diffraction, and θ is the angle of the objective lens aperture.

Overcoming the diffraction limit is crucial for the precise localization of nanoscale objects. The more common approaches involve fitting a point-spread function to the diffraction-limited image of the object: the center of the distribution serves as the indicator for the actual position of the object[69–71]. Various specialized super-resolution methods enable the acquisition of sub-diffraction-resolution images, allowing us to observe nano-scale systems. These methods include stochastic optical reconstruction microscopy (STORM)[71], photoactivated localization microscopy (PALM)[70], minimal photon fluxes MINFLUXF[72], and stimulated emission depletion (STED) microscopy[69,73] shown in Figure 1-3.

[2] Reprinted from Biophysical Journal, Vol 120, A Al-Shaer, A Lyons, Y Ishikawa, B Hudson, S Boudko, N Forde, Sequence-dependent mechanics of collagen reflect its structural and functional organization, Pages No. 4013-4028, Copyright (2021), with permission from Elsevier.

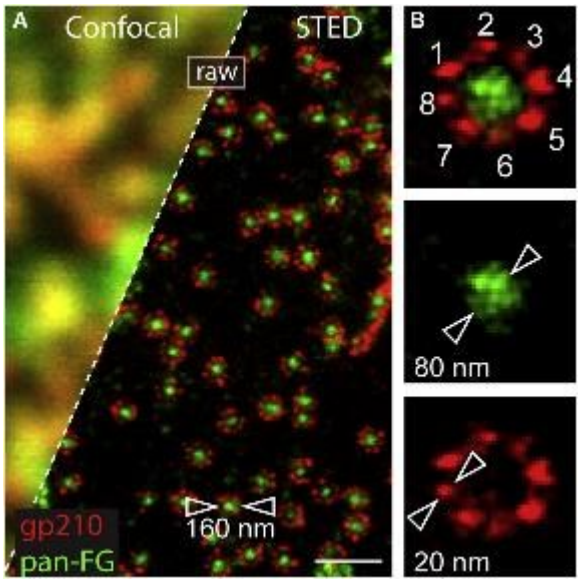

Figure 1-3 Super-resolution STED compared with confocal microscopy.
This image shows nuclear pore complexes (NPC). The scale bar in A is 500 nm and B shows that STED microscopy reveals subunits of this protein complex. This figure was taken from[73].

There is a wide variety of optical techniques that nowadays could be chosen to fit the specific experiment that is to be performed. In our experiments, we aim to track molecular binding events occurring near an interface and minimize the background fluorescence. For this aim, we have chosen TIRF microscopy, a technique that selectively excites fluorescent molecules in close proximity to the sample surface.

1.2.1. TIRF Microscopy

TIRF microscopy is an optical technique that enables the visualization of individual fluorescent molecules with exceptional precision and sensitivity. Using the principle of total internal reflection, TIRF microscopy takes advantage of light's interaction with interfaces to illuminate only those molecules in immediate proximity to a surface[74,75]. TIR excitation of the sample is distinct from epifluorescence microscopy, which illuminates throughout the depth of the sample as shown in Figure 1-4.This selective illumination provided by TIR minimizes background fluorescence coming from molecules situated farther from the interface, thereby providing a clearer view of molecular behaviors happening within 100-nanometer-scale distances from the surface.

The operation of TIRF microscopy involves directing a laser beam at an angle that exceeds the critical angle of incidence θ_c onto the interface between a medium with

a higher refractive index n_1, usually glass, and a medium with a lower refractive index n_2, such as water, a biological sample, or a buffer solution:

$$\sin\theta_c = \frac{n_2}{n_1}. \qquad [2]$$

After it interacts with this interface, the laser light undergoes total internal reflection, forming an evanescent wave that penetrates the medium to a depth of hundreds of nanometers depending on the index of refraction of the media and the incidence angle[74,76,77]. Fluorophores situated within this region become excited and then emit fluorescence that is directed by optics to be captured by a microscope's camera.

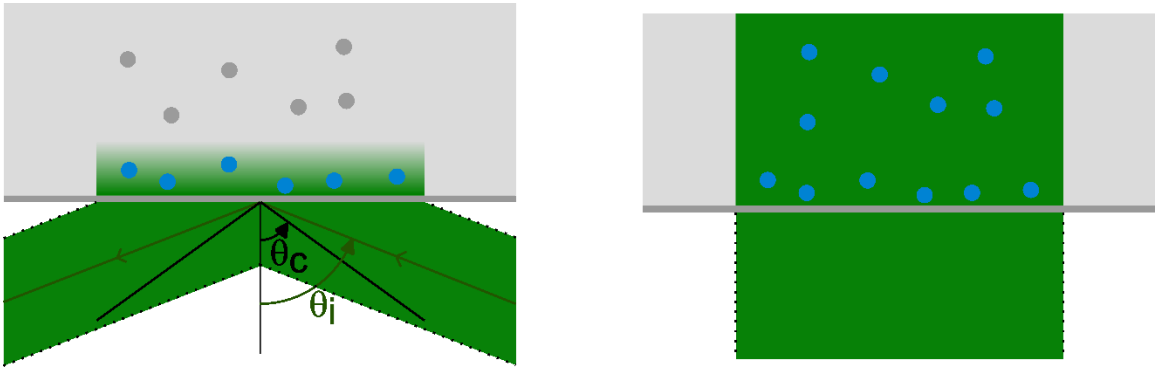

Figure 1-4 TIRF vs epi-illumination fluorescence microscopy.
This figure illustrates total internal reflection fluorescence (TIRF, left) versus epi-illumination (right) microscopy. TIRF occurs when the incident angle (θ_i) exceeds the critical angle (θ_c), exciting only particles near interfaces (blue circles) and not particles away from the surface (gray circles). In epi-illumination, particles close and away from the edge (blue circles) are excited. The dotted lines indicate the edges of the light beam.

TIRF microscopy has been used to reveal details about fundamental cellular mechanisms such as diffusion[78], interactions between proteins[79], dynamics of cell membranes[79], and how signals are transmitted within cells[80], with great clarity and detail. Moreover, TIRF has been integrated with other fluorescence techniques, including Fluorescence Recovery After Photobleaching (FRAP)[81] and Förster Resonance Energy Transfer (FRET)[80,82]; and it has also been combined with force spectroscopy techniques AFM[83] and Magnetic Tweezers[6,84,85].

1.3. Force spectroscopy

Studies that probe the response of a system to different amounts of force are known as force spectroscopy. They enable us to investigate different systems[3,68] like, for example, the intricate multi-stage unfolding processes of individual proteins[17,86] and nucleic acid structures[87,88]. Also, they have been used to assess the binding dynamics between different molecules[14–16,86,89], which is part of what our research group aims to study about collagen.

Force experiments have used and sometimes motivated the development of theoretical approaches[90,91], which have been fundamental in enhancing the extraction of important features of biological systems. Examples include thermodynamic and kinetic parameters obtained from inherently non-equilibrium force-extension experiments[1,13,83,92]. As a result, our ability to obtain insights from systems studied under different forces has improved.

There are several force spectroscopy techniques used to perform single-molecule force experiments (Figure 1-5), like the ones we want to perform. These include Centrifuge Force Microscopy (CFM)[42,93], Acoustic Force spectroscopy (AFS)[94], Atomic Force Microscopy (AFM)[3,14,15,89], Optical Tweezers (OT)[13,87,95] and Magnetic Tweezers (MT)[1,2,4,5,17,89,96]. We have chosen MT as our preferred technique for conducting these experiments, as it aligns best with our experimental requirements.

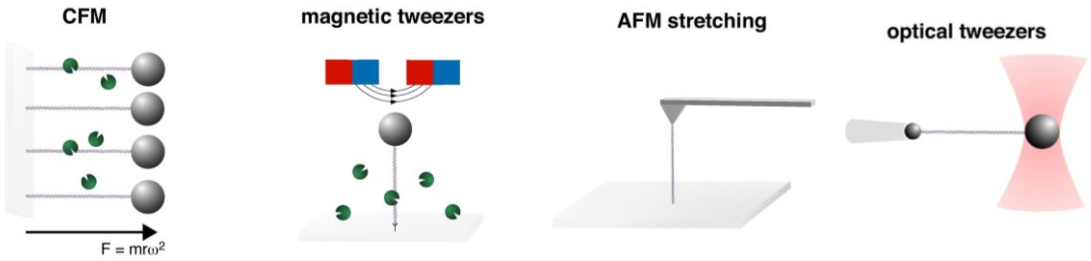

Figure 1-5 Force spectroscopy techniques.
This figure illustrates four techniques used in single-molecule force spectroscopy measurements. From left to right: centrifuge force microscopy (CFM), magnetic tweezers (MT), atomic force microscopy (AFM), and optical tweezers (OT).[3]

Magnetic tweezers operate based on the manipulation of magnetic beads that are functionalized to bind to specific target molecules. These beads serve as handles to exert controlled and precise forces by using external magnetic fields[2,3]. The resulting responses provide valuable insights into the underlying biophysical mechanisms. One of the key advantages of magnetic tweezers lies in their ability to apply both forces and torques to biological samples, making them suitable for investigating a wide range of mechanical properties. The magnetic field's strength and direction can be adjusted to apply forces from a few to hundreds of picoNewtons[1,2,4–6], covering a biologically relevant force regime. This is usually done by approaching or withdrawing permanent magnets from the sample. Moreover, the rotational control offered by magnetic tweezers enables the measurement of torsional properties, thereby facilitating the study of mechanisms such as DNA supercoiling[92,97] or the twisting dynamics of protein filaments[98].

Furthermore, MT have been shown to offer an exceptional spatial resolution, down to the nanometer scale, and temporal resolution in the range of hundreds of Hz[2,4,5]. These characteristics make them well-suited for real-time investigation of some dynamic processes. By precisely tracking the position and movement of the magnetic beads, quantitative data could be extracted from MT experiments including parameters like stiffness[5,92,96], DNA linking number[1,5], binding constants[89] , and relaxation timescales of biomolecules. This information plays a crucial role in understanding the mechanics of

[3] Reprinted from Current Opinion in Chemical Biology, Vol 53, M Kirkiness, K Lehmann, N Forde, Mechanics and structural stability of the collagen triple helix, Pages No. 98-105, Copyright (2019), with permission from Elsevier.

cellular processes, including DNA replication, protein folding, binding kinetics, and molecular motor mechanisms[1,4,5,18,99,100].

Another of the most commonly used techniques to perform single-molecule force-extension tests is AFM[3,14,15,89]. For this type of experiment, a molecule is tethered —either nonspecifically or via specific chemical interactions— between a sharp tip on a cantilever and a surface. Then the sample is withdrawn to induce tension in the molecule. The cantilever deflection provides information about the extension and force, which is then analyzed to mechanically characterize the molecule under study.

While AFM is a widely used technique, instead, we want to perform force-extension experiments using MT which offers several advantages over AFM. MT typically has higher force sensitivity compared to AFM at low forces, allowing for the detection of small force ranges and extensions that might be relevant to the study of collagen behavior. Also, MT has multiplexing capabilities: it can simultaneously manipulate multiple molecules under identical conditions, enabling higher-throughput data acquisition and parallel experimentation. This capability accelerates data collection and lets us study larger experimental datasets.

OT have also become a widely used force spectroscopy technique. They use radiation pressure that generates a force gradient to trap and manipulate particles[101]. In a typical OT setup, a laser beam is focused by a microscope objective lens, creating a tightly focused spot known as an optical trap. When a microscopic particle, such as a bead, encounters this trap, the intensity gradient of the laser beam generates a force that pushes the particle toward the center of the beam. This force is proportional to the gradient of the light intensity and causes the trapped particle to be confined within the focal region of the laser[13]. To measure the force exerted by OT, it is necessary to determine the trap stiffness by doing a calibration. When the trap is calibrated, the force can be inferred from the displacement of the particle from the trap center. This displacement is often detected using the interference pattern created by the scattered light from the bead and the unscattered light, measured by a quadrant photodiode (QPD)[3,13]. The precision and versatility of OT depend on the ability to control the position of the trap by manipulating the laser beam[90]. Changing the position and intensity of the laser allows the user to move, position, and manipulate individual particles with high accuracy. This capability enables OT to exert precise picoNewton forces on individual

molecules, facilitating real-time investigation of molecular responses under force[3] and offering insights into dynamic processes such as folding and unfolding of proteins[11].

Even though OT is widely used, MT offers several advantages over OT. One notable benefit is that due to the relatively stable magnetic field gradient in MT (i.e., over hundreds of μm), experiments can be conducted at nearly constant force without the need for a complex feedback loop, as required in the case of OT[3,13]. Furthermore, MT selectively acts on magnetic objects, such as superparamagnetic beads, without affecting other non-magnetic objects like cells, biological molecules, or even sample contaminants. This is a practical problem when OT are used because other undesired particles can get trapped by the focused beam. Additionally, MT eliminates issues of heating and photodamage since it does not need intense radiation. As mentioned before, MT also allows for the possibility of performing multiplexed single-molecule measurements by simultaneously manipulating different beads on the same sample which enables the collection of sufficient statistics in a shorter time frame[1,3,17].

A relatively new technique called Centrifuge Force Microscopy (CFM)[42,93,102] can also be used to perform single-molecule force experiments. CFM uses centrifugal force to apply mechanical stress to polymer molecules immobilized on a substrate. Initially, polymers are tethered at one end to a glass surface and at the other end to a bead. Once the molecules are tethered, they are subjected to centrifugal forces by spinning the sample at high speeds, typically using a centrifuge that holds the CFM. As the sample rotates, the centrifugal force stretches the molecules radially outward along the axis of rotation. Monitoring the beads attached to the molecules with a camera allows for the detection of when they go out of focus, indicating large polymer extension or rupture. This enables the study of rupture forces, the influence of force on cleavage, and interactions with other molecules, among other mechanical features. The main advantage of CFM is its high throughput [42,102]: it can simultaneously track thousands of molecules in a single experimental run. Our laboratory has been a pioneer in the development of CFM and it aims to complement experiments performed with CFM with experiments conducted using MT. The additional advantage offered by MT is that it provides information about the polymer extension, which is crucial for studying some mechanisms underlying molecular behavior.

Table 1. Comparison between force spectroscopy techniques.

	Optical Tweezers (OT)	Atomic Force Microscopy (AFM)	Centrifuge Force Microscopy (CFM)	Magnetic tweezers (MT)
Spatial resolution (nm)	0.1–2	0.5–1	2	5–10
Temporal resolution (s)	10^{-4}	10^{-3}	10^{-2}	10^{-1}–10^{-2}
Force Range (pN)	0.1–100	10–10^{4}	0.1–100	10^{-3}–10^{2}

Values for OT, AFM, and MT are taken from Neuman and Nagy[3] and values for CFM are taken from Yang et al.[102]

Each force spectroscopy technique has its own set of advantages and limitations in aspects like spatial resolution, temporal resolution, and force range; the comparison between them is outlined in Table 1. It is important to note that some of these techniques might have better resolutions than those presented in the Table 1 due to technological advancements since the publication of Neuman and Nagy[3]. In our research, MT was chosen as the technique to use due to some practical advantages and the relatively easy implementation with TIRF, which will be described later in this chapter. I aimed to refine the experimental setup and data acquisition processes associated with MT to conduct force-extension experiments, a common application in single-molecule force spectroscopy.

1.3.1. Single-molecule force experiments

Single-molecule experiments in biophysics are important because they can isolate individual components of biological systems and probe their processes with more precise control. Analyzing single-molecule force experiments is a suitable approach to get insights into various aspects of the system under investigation. These insights include equilibrium binding constants[89], mechanical features such as stiffness[103], free energy landscapes[14,89,91], unfolding and folding dynamics[13,95], among other relevant physical characteristics.

While traditional ensemble approaches offer information about the overall behavior of biological systems, specific molecular mechanisms might be masked due to the inherent complexity of ensemble behavior in biology. In contrast, single-molecule biophysics experiments allow for the observation of mechanisms and events occurring at

the molecular level, which may remain hidden in ensemble measurements. The direct probing of these molecular behaviors with one or a few molecules lets us understand better dynamic processes occurring at the molecular scale.

Within our bodies, an intricate interplay between forces such as electrostatic interactions, covalent bonding, hydrogen bonding, and hydrophobic interactions operates at the molecular level, presenting a profound challenge to understand them individually when ensemble approaches are used. From protein folding to molecular binding dynamics, these forces are key players in fundamental physiological processes. Single-molecule force experiments provide a unique advantage in dissecting molecular interactions, offering a way to disentangle the behavior of these forces and make it easier to understand their role individually.

Collagen is a good example to illustrate the significance of single-molecule force experiments in understanding biological processes. This protein plays a crucial role in different physiological processes such as providing tensile strength and structural integrity to tissues[104]. The complex hierarchical structure of collagen and its interactions with other molecules present a challenge for traditional ensemble techniques to fully comprehend its mechanical properties and interactions as individual molecules. However, single-molecule force experiments offer a unique opportunity to dissect collagen's behavior at the molecular level. Subjecting individual collagen molecules to controlled mechanical forces using techniques like MT could reveal some of the intricate response mechanisms of collagen such as unfolding, stretching and twisting, as well as how these affect the binding dynamics of partner molecules. Insights gained from single-molecule force experiments on collagen will get us a step closer to understanding the role of collagen in various important physiological processes such as wound healing and tissue development.

1.3.2. Polymer mechanics models

Understanding the mechanical behavior of polymers, particularly in the context of single-molecule force experiments, requires the use of specific models that describe the relationship between force and extension. These models are fundamental for interpreting experimental data and gaining insights into the physical properties of biomolecules such as DNA, collagen, and other polymers. Among the most widely used models are the

Freely Jointed Chain (FJC), Worm-Like Chain (WLC), and Extensible Worm-Like Chain (eWLC).

Freely Jointed Chain (FJC) Model

The FJC model is one of the simplest models used to describe the mechanical properties of polymers. In this model, the polymer is considered as a series of rigid segments, that are freely connected by joints with no preferred direction, allowing for complete rotational freedom[105]. The FJC model is used to describe polymer behavior in the entropic regime[106] and it is useful for describing polymer response at low forces where the thermal energy is comparable to or greater than the energy associated with stretching the polymer.

Mathematically, the extension of a polymer under force in the FJC model is described by the Langevin function[105],

$$\langle z \rangle = L\left(\coth\left(\frac{F \cdot b}{k_b T}\right) - \frac{k_b T}{F \cdot b}\right), \quad [3]$$

where $\langle z \rangle$ is the average end-to-end extension, L is the contour length of the polymer, F is the applied force, k_b is the Boltzmann constant, T is the temperature and b is the Khun length which is the length of the rigid rods. The FJC model is particularly suitable for describing polymers with a high degree of flexibility but may not accurately capture the mechanical behavior of stiffer polymers or those that exhibit significant bending stiffness.

Worm-Like Chain (WLC) Model

The WLC model offers a more realistic description of polymer behavior[103], especially for semi-flexible polymers like DNA and collagen. Unlike the FJC model, the WLC model accounts for the bending stiffness of the polymer. Thermal fluctuations enable backbone bending, which introduces a persistence length (l_p) as a key parameter in this model. The persistence length is a measure of the polymer's stiffness and is defined as the length over which the polymer's direction becomes uncorrelated (Figure 1-6):

$$\langle \hat{t}(s) \cdot \hat{t}(s+l) \rangle = e^{-\frac{l}{l_p}}. \quad [4]$$

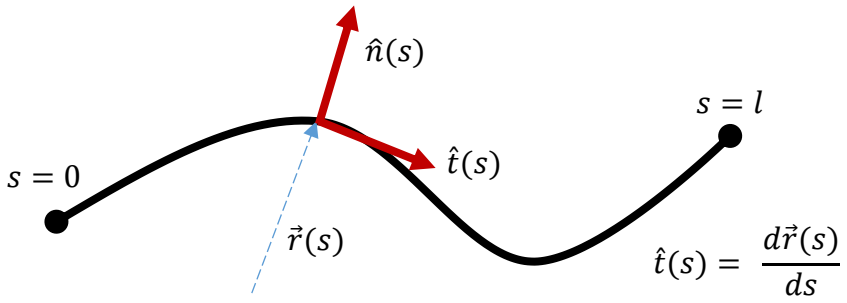

Figure 1-6 Persistence length.
Geometry of a WLC of a segment of a polymer, showing tangent vectors and arc lengths used in equation [4].

In the WLC model, the often-used interpolation formula[107] relates the force applied to stretch the polymer to the extension *z* between its ends:

$$\frac{Fl_p}{k_bT} = \frac{1}{4\left(1-\frac{z}{L}\right)^2} - \frac{1}{4} + \frac{z}{L}. \quad [5]$$

The WLC model is particularly effective at describing the mechanical response of polymers over a range of forces where the polymer is not completely straightened, because it assumes that the polymer is inextensible. This is the regime where the force applied to the polymer is pulling against the entropic force.

Extensible Worm-Like Chain (eWLC) Model

The eWLC model is an extension of the WLC model that incorporates the elasticity of the polymer backbone[108]. This model is particularly relevant for polymers that experience significant elongation under high forces, where the assumption of inextensibility in the WLC model becomes invalid. The eWLC model adds an additional term *K* to account for the enthalpic stretching of the polymer backbone, where *K* is the stretch modulus, representing the stiffness of the polymer backbone:

$$\frac{Fl_p}{k_bT} = \frac{1}{4\left(1-\frac{z}{L}\right)^2} - \frac{1}{4} + \frac{z}{L} + \frac{F}{K}. \quad [6]$$

This model is particularly useful for describing the mechanical behavior of biomolecules that exhibit both bending stiffness and significant elongation under high forces.

These polymer mechanics models can be further improved to include additional response mechanisms such as twisting [95]. They are crucial for interpreting force-extension experiments[3,89] performed in different techniques like AFM[14,15], OT[13,38,95,108], and MT[1,96,109]. Fitting experimental data with these models allows us to extract valuable information about the mechanical properties of the molecules, such as their persistence length, contour length, and stretch modulus. This understanding is key to revealing the molecular mechanisms underlying biomolecules under mechanical stress, which is particularly important in many different physiological contexts.

1.3.3. Force-extension experiments

Force-extension experiments allow us to investigate the mechanical properties of biomolecules such as DNA, collagen, and other polymers at the single-molecule level. These experiments involve subjecting individual molecules to controlled mechanical forces and measuring their response in terms of extension[14,15,38,87–89,103,108,110]. This kind of experiment typically involves the use of specialized instrumentation such as OT, MT, or AFM, as previously described.

During a force-extension experiment, a single molecule is typically tethered between two surfaces, for example between a glass surface and a magnetic bead in the case of MT, as shown in Figure 1-5. The molecule is then subjected to mechanical forces by manipulating the position of this bead. As a force is applied, the molecule may undergo conformational changes, depending on its mechanical properties and interaction with its surroundings. These structural transitions are reflected in the force-extension curve (Figure 1-7) and provide insights into the molecule's structural stability, folding dynamics, and interactions with ligands or other molecules. In our case, we want to perform force-extension experiments on collagen with and without binding partners using MT.

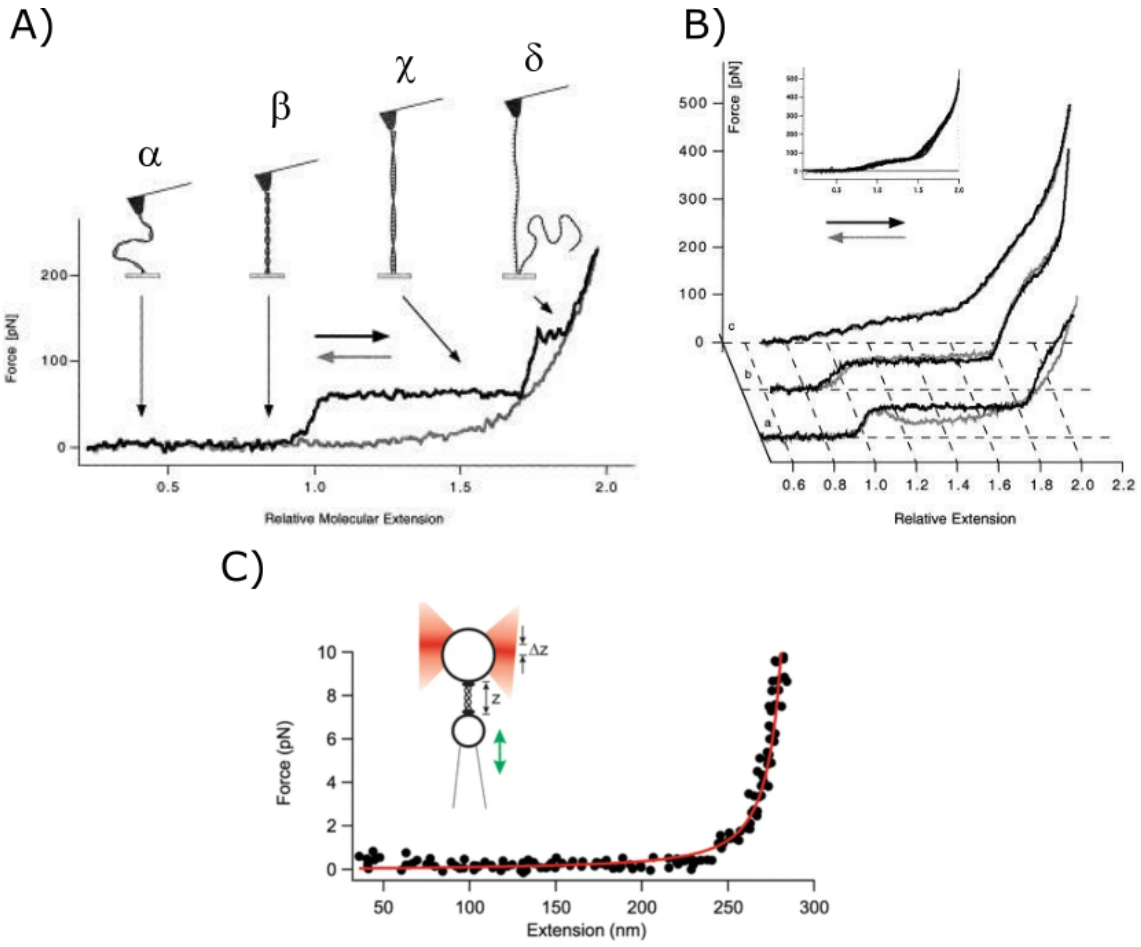

Figure 1-7 Force-extension curves.
(A and B) double-stranded DNA pulled using AFM taken from[111], and (C) force-extension curve of collagen type II using OT taken from [41]. (A) shows the structural changes in free DNA under applied force: α) the entropic region, β to χ)the enthalpic region, and δ) the regime where the double strand separates into single strands. (B) shows the force-extension curves of DNA interacting with the anti-cancer agent cisplatin, measured at different time intervals: a) immediately after its introduction, b) 1 hour later, and c) after 24 hours, illustrating the impact of cisplatin interaction on DNA's mechanical properties. (C) shows a force-extension curve of collagen type II, fitted using the worm-like chain (WLC) model.

1.4. Integration of MT and TIRF microscopy

Many previously unknown molecular behaviors in biological systems have been revealed because advanced techniques are merged together. This allows the simultaneous extraction of different features of the system under study, for example, to mechanically manipulate and observe the system at the same time. Among these techniques, magnetic tweezers (MT) have emerged as a versatile and powerful tool to be combined with others like TIRF microscopy[6]. This combination allows for the

application of highly controllable forces, precise measurement of mechanical responses, and simultaneous fluorescence visualization[1–5].

Magnetic tweezers have been combined with additional techniques to explore different systems and mechanisms. For instance, integrating them with flow cells[112] and fluorescence techniques[1,5,6] enables researchers to monitor additional mechanisms like the binding of other molecules while applying force on the primary biopolymer. Previous studies have demonstrated that applying force along biopolymers like DNA and collagen influences interactions with other molecules, reflected in force-extension curves[15,43,44,113,114]. Our research group aims to study such interactions, specifically focusing on how force and temperature affect the binding dynamics of other molecules to collagen.

Combining Magnetic Tweezers (MT) and Total Internal Reflection Fluorescence (TIRF) microscopy enhances our capacity to study the behavior of single-molecule biopolymers across different conditions. MT enables the application of controlled mechanical forces on targeted molecules, while TIRF microscopy allows simultaneous observation from the bottom of the sample. This integrated methodology is primarily employed towards probing the binding kinetics of regulatory proteins, providing us the means to reveal the molecular mechanisms governing these interactions under different mechanical perturbations and temperature fluctuations.

1.5. Outline of the Thesis

This thesis is organized into five chapters, each addressing different parts of the experimental design, methodology, and findings related to Magnetic Tweezers (MT) and force-extension measurements.

In Chapter 2, I describe the instrument used in this research, with a focus on the MT setup. Special attention is given to characterizing the magnetic field generated by the MT and how it is used to apply forces on superparamagnetic beads. Additionally, I discuss the integration of Total Internal Reflection Fluorescence (TIRF) microscopy with the MT system, detailing how the combination of these two techniques enhances the study of molecular binding events at the single-molecule level.

Chapter 3 explores the assays used to tether DNA molecules to the glass surface and magnetic beads. Two different tethering approaches are highlighted, outlining the methods used to functionalize the surfaces and attach DNA in the experimental setup. The chapter also introduces the microsphere adhesion assay (MAGIC assay), which was used to assess the specific binding and success of the tethering protocols.

In Chapter 4, I present the methodology for performing force-extension measurements using the MT system. Key variables that need to be measured for accurate force-extension analysis are discussed, including bead fluctuation, bead height, and temperature. This chapter also covers the modifications made to the optical and computational systems, such as the improved illumination path and the development of a correlation-based algorithm, which significantly enhances the bead height detection and force measurements.

Chapter 5 summarizes the main findings of the research and discusses the broader implications of the results. I also outline potential further improvements and future research directions using the MT and TIRF system to study single-molecule polymers

Chapter 2.

Instrumentation description

Our instrument combines the advantages of TIRF, providing high spatial resolution and detection efficiency near the surface, with the precision of magnetic tweezers to manipulate biomolecules, as shown in Figure 2-1. TIRF microscopy selectively illuminates a thin section of the sample above the bottom surface, enhancing the visualization of molecular events (e.g. binding dynamics). Simultaneously, magnetic tweezers enable the controlled application of forces and torques on individual molecules, allowing the investigation of mechanical properties. The merging of these techniques in a single instrument enables us to study the interaction between binding dynamics and mechanical forces, potentially elucidating the relations between molecular structure, kinetics, and function. This instrument was purchased from and designed by MadCity Labs; I assisted with its installation, and my work has focused on calibrating and further improving it for single-molecule experiments. A list of the relevant components of the instrument is presented in Appendix A.

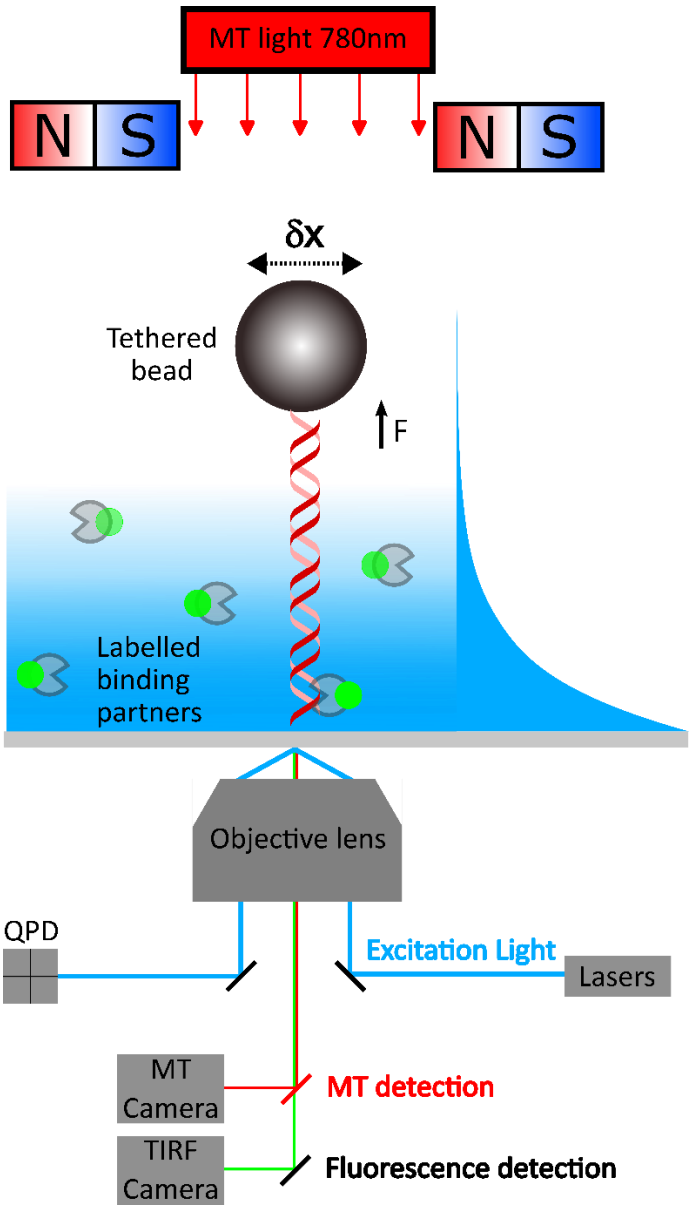

Figure 2-1 Instrument set-up.
Total internal reflection fluorescence (TIRF, bottom) and magnetic tweezers (MT, top) are integrated into a single instrument. MT applies force (*F*) on the polymer via permanent magnets pulling the magnetic bead. TIRF tracks the fluorescence of labeled binding partners, which are molecules of interest that bind to the polymer. The instrument uses 780 nm LED transillumination to image the magnetic beads and TIRF with different lasers (405/488/561/638 nm) excite and detect the binding partners. The laser excitation includes feedback control via a Quadrant Photo Diode (QPD; Mad City Labs, TIRF-Lock™) to correct small changes in the excitation angle using a piezo stage (Mad City Labs, Nano-Drive®). A dichroic mirror (Chroma, ZT775sp-2p) separates the long-wavelength light (> 775 nm) directed to the MT camera from the short-wavelength light (< 775 nm) directed to the TIRF fluorescence camera. *δx* represents the fluctuation of a bead tethered by the biopolymer of interest. The figure is not to scale.

2.1. Magnetic tweezers

The primary experimental technique of this thesis is magnetic tweezers (MT), a widely used tool in biophysics for various studies that require mechanical manipulation[1,5,18]. For example, it has been applied to investigate structural changes in proteins[17,86], intracellular mechanics[115,116], proteolysis[16,43,44], and the binding of other molecules to biopolymers[6,89]. In our project, the technique will be applied to the study of single-molecule polymers under force. The ultimate goal of our research group is to use magnetic tweezers to pull on single molecules and observe binding to them using TIRF microscopy.

For my thesis as a proof of concept and to explore the instrument's capabilities, I develop our new magnetic tweezers (MT) instrument and associated experiments to apply force and stretch DNA. This well-studied biopolymer offers standardized tethering procedures. DNA's response to stretching forces has been extensively investigated [13,15,95,108], revealing different phases in its behavior. Distinct regions of its force-extension response are modeled in different ways [95,103,108]. In the low-force regime (< 10 pN), the force-extension behavior is well described by the inextensible Worm-Like Chain (WLC) model (Section 1.3.2)[103,107]. In contrast, at moderate to high forces, additional mechanisms such as extension and twist come into play[14,87,88,95,103,108]. Given the low force range of our instrument, I anticipate that it will be well suited to observing WLC behavior of DNA.

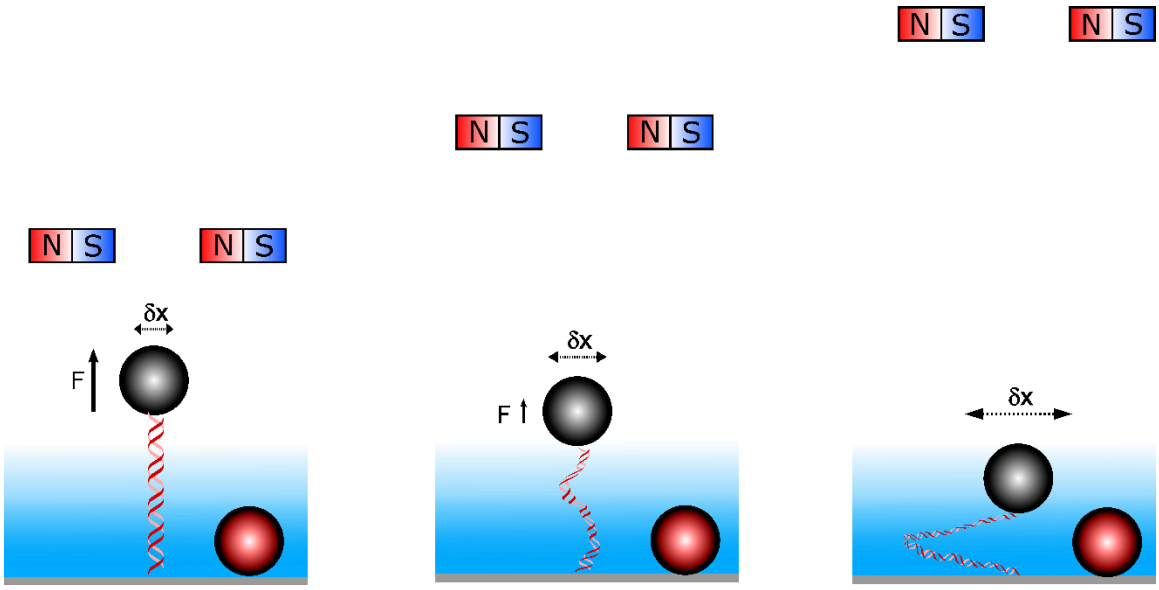

Figure 2-2 Magnetic Tweezers diagram.
Different magnet heights produce distinct forces on a superparamagnetic bead (black), leading to a change in the extension of a tethered DNA molecule. The red sphere is a fiduciary bead affixed on the surface, and the black sphere is the functionalized bead tethered to the DNA. The figure is not to scale.

Magnetic tweezers exert force on objects with a magnetic moment using a magnetic field gradient[117],

$$\vec{F} = \nabla \cdot (\vec{m} \cdot \vec{B}), \qquad [7]$$

where $\vec{m}$ is the magnetic moment of the object (bead) and $\vec{B}$ is the applied magnetic field (in our case, from permanent magnets). In our setup, superparamagnetic beads are attracted by the higher gradient of a magnetic field toward two permanent neodymium magnets (N52). Specifics of the magnet dimensions, magnetic field, magnetization of the beads, etc., are provided in the two next sections. The magnets pull on superparamagnetic beads tethered to the bottom surface of the sample chamber via the polymer under study, inducing tension in the polymer. Adjusting the magnets' proximity to the sample changes the tension: it increases when the magnets are moved closer to the sample and decreases when they are withdrawn away from the sample, as depicted in Figure 2-2. The distance to the sample can be changed in small steps using a stepper motor (MCL-μS2544, 95 nm step size), controlling the height of the magnet holder, as shown in Figure 2-3.

2.1.1. Imaging path

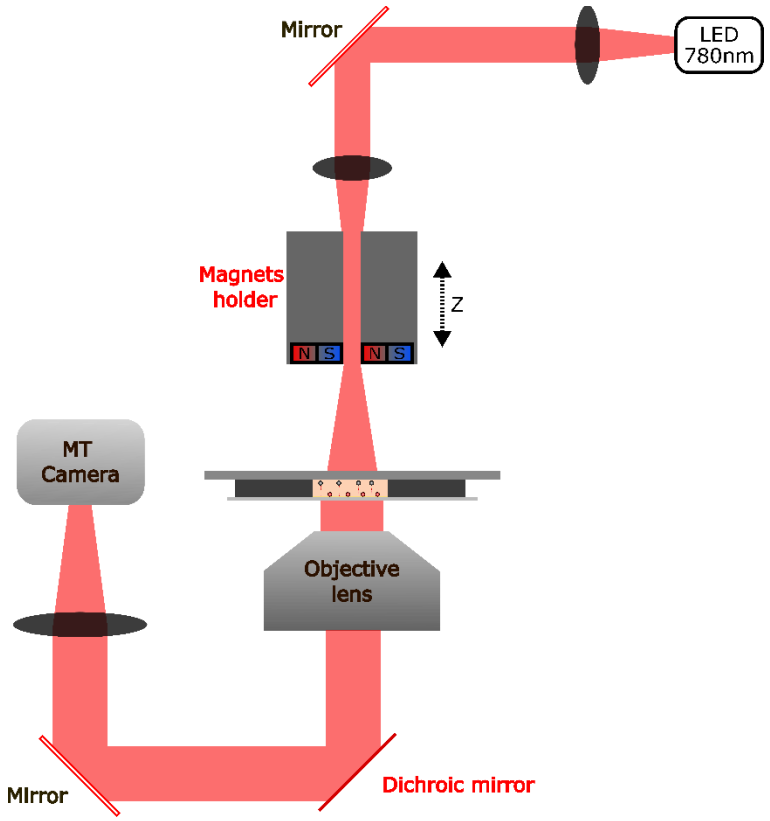

Figure 2-3 Magnetic Tweezers imaging path diagram.
The excitation path includes a 780 nm LED, a flat mirror, and two converging lenses. The detection path consists of a dichroic mirror, a flat mirror, a converging lens, a bandpass filter, and a high-speed camera.

The illumination comes from above the sample and originates from an LED that emits near-infrared light centered at a wavelength of 780 nm with a maximum power of 300 mW (Thorlabs M780L3). The light passes through a sequence of optical components: a converging lens, a steering mirror, and another converging lens, before passing through a 1 mm diameter aperture in the center of the magnet holder. During my experiments, I discovered some issues with the imaging path and made several modifications. Specifics of the optics in the illumination path and the adjustments I made are detailed in Section 4.2.2.

When it reaches the sample, the light scatters off the beads, generating a diffraction pattern that depends on the distance between the beads and the focal plane of the objective lens (see Chapter 4). The scattered light is then separated by a short-pass dichroic mirror (Chroma ZT775sp-2p, shown for the MT detection branch in Figure

2-1): the transmitted light is directed to the fluorescence camera (TIRF detection; Hamamatsu ORCA-Fusion BT C12440-20UP) and the reflected light to the high-speed MT camera (Basler acA1440-220um). Before reaching the camera, the light is focused by a converging lens (f = 100 mm) and passes through a band-pass filter (775 nm ± 25 nm) to ensure relatively monochromatic light and reject any background light from the TIRF portion of the instrument.

2.1.2. Magnetic Fields

Choosing the appropriate magnet configuration is essential when constructing magnetic tweezers to study a specific system. Different magnet arrangements produce different magnetic fields and forces, directly impacting the versatility and strength of an instrument. Our instrument setup incorporates two N52 permanent magnets, which are Nd_2Fe_3B with a maximum energy product of $(BM)_{max}$ = 52MGOe. The magnets are each 8 x 5 x 3 mm^3, arranged as shown in Figure 2-4 and separated by one millimeter. They are fixed in a vertically adjustable rotational stage that enables changes in force via height changes of the magnets and torque application through the rotation relative to the sample. In contrast, when MT has a single cylindrical permanent magnet, it lacks the ability to apply torque and rather allows free rotation of the bead because of the axial symmetry of the generated field, but it can be beneficial for studies requiring a decoupling of stretch and twist[1]. Moreover, if three-dimensional manipulation of the beads is necessary, a more complex magnetic field configuration is required, for example using electromagnetic tweezers[96]. The selection of the magnet setup is therefore tailored to the specific needs of the study and the desired manipulation capabilities.

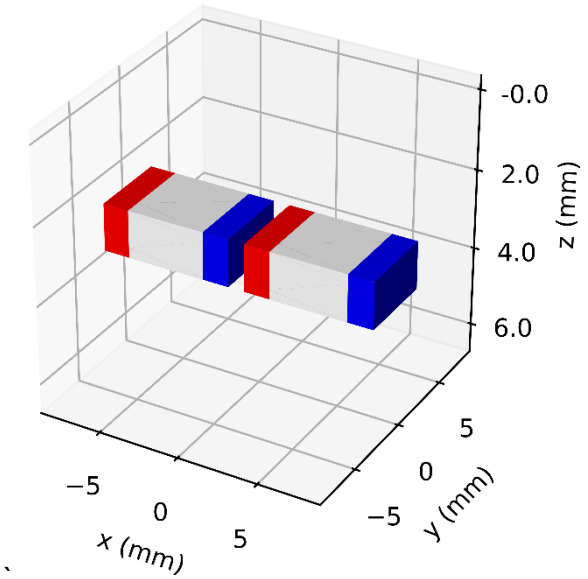

Figure 2-4 Magnet configuration.
The south poles are represented by the color blue while the north poles are represented by the color red. The dimensions of the magnets are 8 mm x 5 mm x 3 mm.

The configuration of the magnets in our instrument is NS NS as shown in Figure 2-4. This arrangement produces a magnetic field that decays in the vertical (*z*) direction away from the magnets. For our setup, a requirement for parallelized measurements — interrogating multiple beads in the imaged sample chamber — is the uniformity of the magnetic field across the sample. I wanted to understand how the exerted force would vary if the beads were not precisely positioned at the midpoint between the magnets. Additionally, I aimed to determine the range of magnet heights over which forces in the physiologically relevant range of picoNewtons could be exerted. To answer these questions, I used two approaches: one was to measure the magnetic field generated by the magnets and the other was to use a simulation to confirm the trends of the measurements. This analysis will give us important information about the behavior of the magnetic field and its implications for our experimental setup.

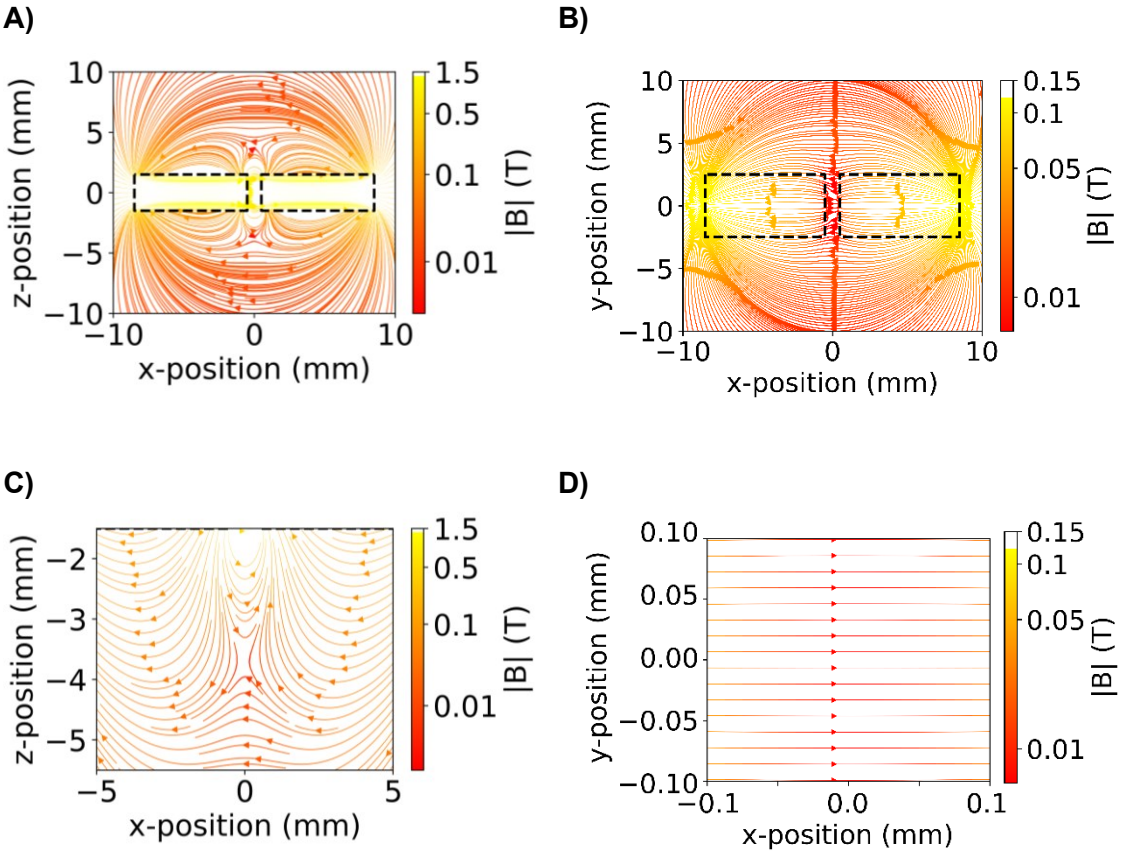

Figure 2-5 Magnetic field lines from simulation.
This figure represents the NS NS configuration of two permanent magnets. The rectangles with dotted lines represent the locations of the magnets. The plots in A and C illustrate the plane perpendicular to the sample (at y = 0 cm), while the plots in B and D depict planes parallel to the sample (at z = 3.6 mm). Zoomed-in views C and D offer detailed insights into key regions.

I used the Python library Magpylib©[118] which is an object-oriented program that uses analytical approaches[119–121] to predict magnetic fields generated by permanent magnets. In my case, this involved inputting the geometry (8x5x3 mm^3) and remanence (1.45 T) of the magnets provided by the manufacturer. Figure 2-5 shows the magnetic field in two distinct cross-sections: one perpendicular to the sample at the midpoint of the magnets (y= 0 cm), and another parallel to the sample, located 1 cm away from the edge of the magnets (z= 4 cm). This simulation reveals a distinct feature of the field in the (x,z) plane: beneath the midpoint of the magnets, the magnetic field changes direction.

The magnetic field of the permanent magnets in our MT was measured using a Hall probe (Group 3, DTM-151 and MPT-237-75). The probe was attached to the stage near the location where the chamber containing the beads would be situated, oriented to

measure the x-component of the magnetic field (Figure 2-6 (A)). Using the stepping motor of the magnet holder, the magnets were incrementally moved away (z-direction) while the horizontal magnetic field (*x*-direction) was measured. The closest distance between where the Hall probe measures the field and the edge of the magnets is approximately 1.6 mm. As expected, the magnetic field decreased by increasing the distance between the magnets and the probe both for the measured and simulated magnetic field, as shown in Figure 2-6. It is important to note that I do not attempt a direct quantitative comparison between the simulated field and the measured data because of discrepancies in the values that are discussed later in this chapter, but rather to compare the trends of these two approaches.

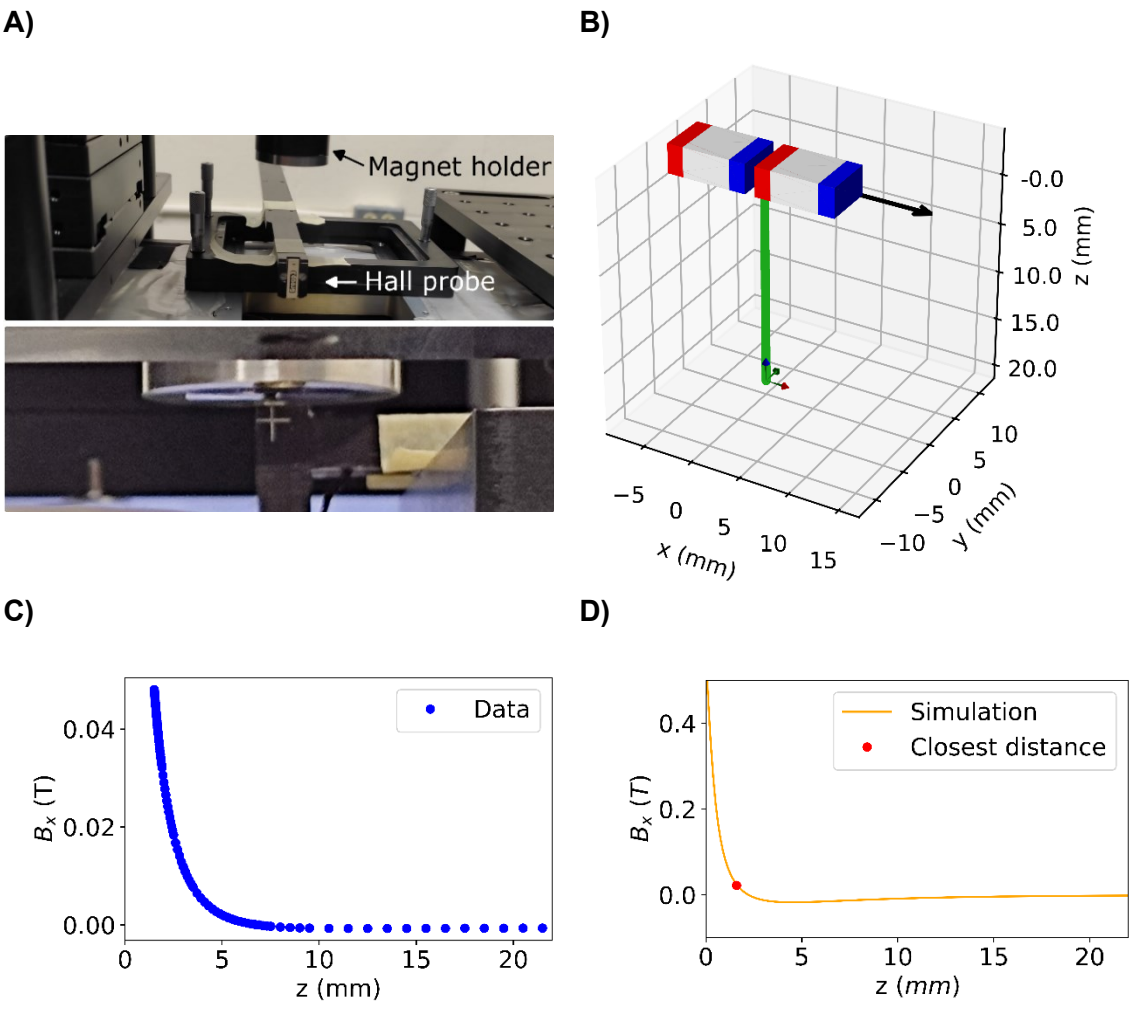

Figure 2-6 Magnetic field at different magnet heights (z).
This figure shows the magnetic field in the x-direction at various heights from the edge of the magnets (z = 0) for both the measured and the simulated field. On the left (A and C):

experimental measurements using a Hall probe. A shows the experimental setup and C presents the fields measured in the x-direction at a location centered between the two magnets. The error on the Hall probe measurements is ±0.000001 T (manufacturer's specifications), and the resolution of the magnets' z positioner encoder is 50 nm (manufacturer's specifications). On the right (B and D): simulation results. B displays the configuration of the magnets and the path (green line) along which the field is displayed in D as a function of height. The value at the closest distance allowed by the Hall probe geometry (1.6 mm) is 0.0219 T in the simulation, as indicated with a marker.

Assessing the uniformity of the magnetic field in the plane parallel to the sample chamber (x, y) involved measuring the *x* component of the field with the Hall probe. This was done by using the piezo stage to move the attached probe in the horizontal plane (x,y) with respect to the center of the magnets. The analysis revealed minimal variations within the range of our field of view (~100 μm): 0.29% along the x-axis and 0.026% along the y-axis. These findings are presented in Figure 2-7. I also simulated the field in that plane and the variation is less than 0.2% along the x-axis and less than 0.02% along the y-axis. In both experimental measurements and simulations these results show that the field does not change substantially over the field of view.

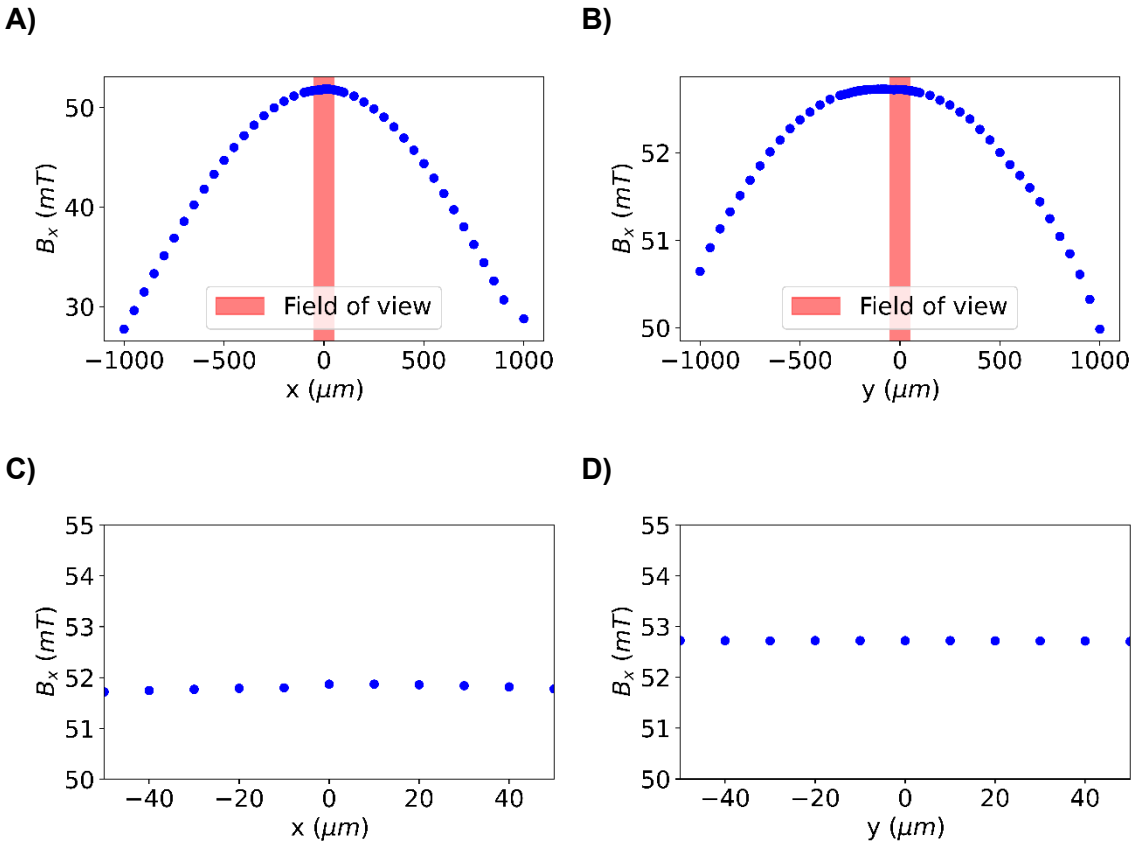

Figure 2-7 Measurement of magnetic field uniformity parallel to the sample. The x component of the magnetic field was measured as a function of displacements within the plane parallel to the sample. The top two plots span a wider range [2 mm], while the bottom two plots are zoomed in depicting the range of the camera's field of view [~100 μm]. The measurements were recorded approximately 1.6 mm below the bottom of the magnets, the closest distance to the magnets allowed by the Hall probe geometry. There is a discrepancy between the highest values of the magnetic field in (A) and (B) likely due to the time gap between measurements, during which some drift may have occurred.

2.1.3. Force calculation from magnetic fields

The force exerted by magnets on a bead can be determined by equation [7], where $\vec{m}$ is the magnetic moment of the bead and $\vec{B}$ is the magnetic field produced by the permanent magnets at the location of the bead. It is known that the magnetic moment of the superparamagnetic bead changes with the applied magnetic field, $\vec{m}(\vec{B})$. I used the magnetization data for amine Dynabeads® M270 and carboxyl Dynabeads® M280 provided by ThermoFisher obtained from the supplementary info in Grob et al.[122] (Figure 2-8). This was used to calculate the magnetic moment as a function of the magnetic field strength by multiplying *M* by the mass of one bead. These values are

subsequently used for force calculations with both the measured magnetic field and the simulated field. For most of the experiments that I have performed, I used amine Dynabeads® M270.

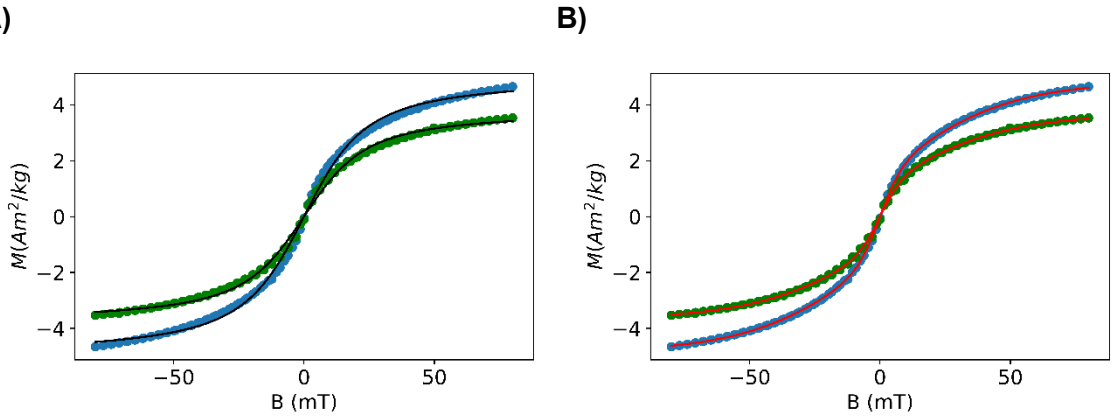

Figure 2-8 Magnetization of beads.
This figure shows the magnetization (*M*) of the amine beads (Dynabeads® M270, blue points) and the carboxyl beads (Dynabeads® M280, green points) for different magnetic fields obtained from Grob et al.[122] (values provided in their supplementary information) and fit with two different equations. (A) is fitted with equation [9] and (B) is fitted with equation [9] (lines; best-fit parameters are given in the text).

To obtain an analytical expression for this sigmoid-like relationship $M(\vec{B})$, a Langevin function can be used (Figure 2-8 (A)). This function represents how the magnetization of an ensemble of monodomain particles changes with an external magnetic field [123]:

$$M(B) = M_s \cdot \left[coth\, aB - \frac{1}{aB}\right]. \qquad [8]$$

Here $a = \frac{\mu H}{k_B T \cdot B}$, *H* is the auxiliar magnetic field, μ is the permittivity, $k_B T$ is the thermal energy, and M_s is the saturation magnetization. The best fit parameters for the amine beads are $M_s = 5.07$ A/m, $a = 0.108\, T^{-1}$ and for the carboxyl beads are $M_s = 3.86$ A/m, $a = 0.108\, T^{-1}$.

I also used an empirical relation with two logistic functions:

$$M(B) = \frac{A_0}{1+e^{-k_0 B}} + \frac{A_1}{1+e^{-k_1 B}} + C, \qquad [9]$$

(Figure 2-8 (B)). Best-fit parameters for the amine beads are $A_0 = 0.0414, k_0 = 6.73, A_1 = 2.98, k_1 = 0.246, C = -4.87$ and for the carboxyl beads are $A_0 = 0.0426, k_0 = 5.12$, $A_1 = 2.22, k_1 = 0.244, C = -3.67$, shown in Figure 2-8 (B),. With these expressions, calculating the product $\vec{m} \cdot \vec{B}$ for each separation between the magnets and beads becomes straightforward, which then allows me to compute the force exerted by the magnets on the beads (Figure 2-9).

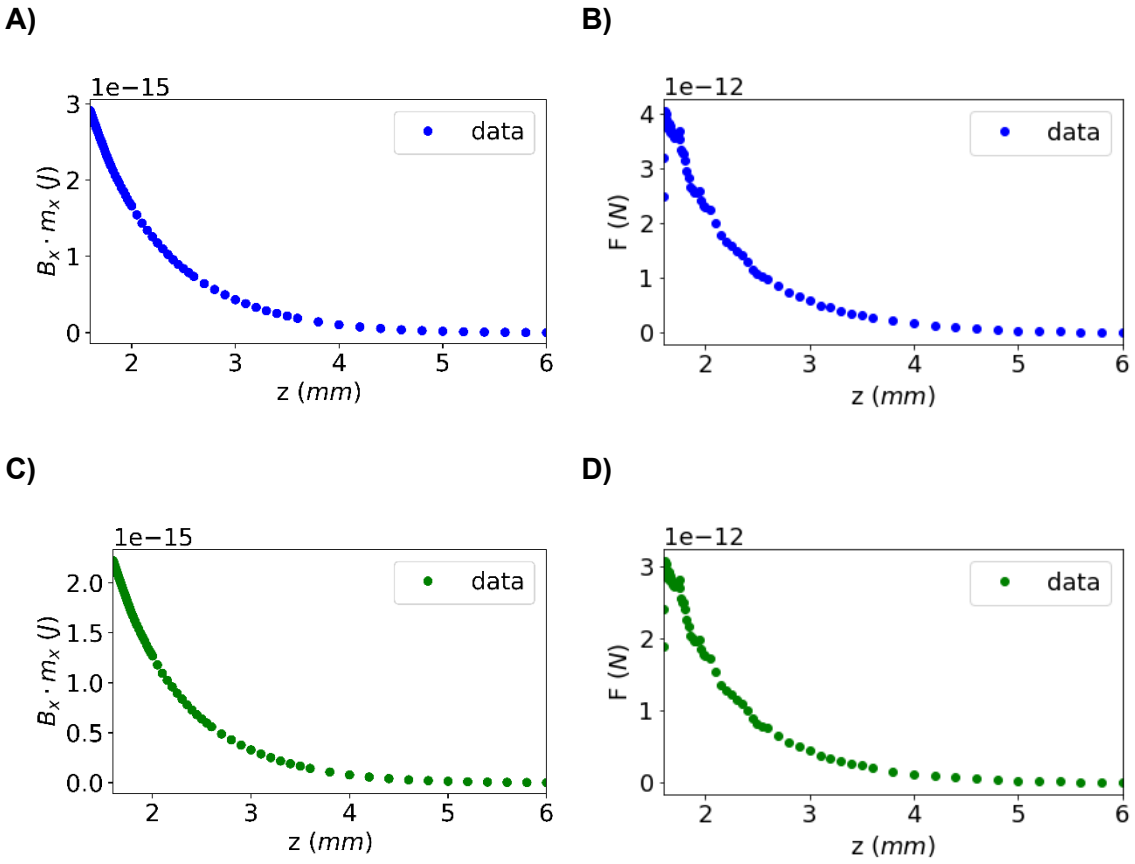

Figure 2-9 Force calculated from experimental magnetic field measurements. (A and B) are the plots for corresponding amine beads, (C and D) are the plots corresponding to the carboxyl beads. $B_x \cdot m_x$ (A and C) is the product of the magnetic field measured with the Hall probe and the magnetic moment of the beads at this magnetic field strength, calculated from [9]. The force (B and D) is calculated from the gradient of this product. *z*=0 mm represents the lower edge of the magnets.

From these results, I learned that the maximum force that can be exerted in the range of these experimental magnetic field measurements is approximately 4 pN. While this force range may be sufficient for some measurements, for others, such as investigating the elastic region of DNA force-extension curves or exploring high-force

regimes of single-molecule collagen behavior, higher forces will be necessary. This is a limitation of the use of the Hall probe for the magnetic field measurements: its closest approach is approximately 1.6 mm the magnet edge. Here, I obtain maximum forces of around 4 pN for amine beads and 3 pN for carboxyl beads, as illustrated in Figure 2-9. In an attempt to calculate the magnetic field measurements at closer separations between the beads and the magnets that were not accessible due to the Hall probe geometry, I used the simulations.

It would be ideal to have an analytic equation of the relation B(z), to fit the Hall probe measurements. However, due to the complexity of this relation shown by Xiao-Fan et al.[120] and Engel-Herbert et al.[121], I chose to use simulations for this purpose. These force calculations are based on the previously described magnetic field simulations that use Magpylib©. Figure 2-10 shows that the force on amine beads at a height level with the lower edge of the magnets (unachievably close in experiments) is above 60 pN. This upper limit matches the maximum forces that are typically reached in MT[1,4]. An important conclusion reached from these calculations is that the force exerted on the beads falls within the biologically relevant range of picoNewtons.

Proximity between the sample and the magnets is crucial for exerting high forces, due to the rapid decline in magnetic field intensity and hence force away from the magnets. One potential method to increase the maximum force accessible in our measurements involves changing the thickness of the top part of the sample chamber. Instead of using a chamber with a microscope slide on top and a cover glass on bottom, as depicted in Figure 2-10 with a distance of 1.264 ±0.006 mm between the outside top surface and the beads (these distances where measured using a micrometer in 3 different chambers and 10 different measurements per chamber). A more effective approach would be to use cover glass on both the upper and lower parts of the chamber, resulting in a distance of 0.351 ±0.002 mm between the top surface and the beads. This modification allows closer proximity to the magnets, and therefore significantly increases the maximum force exerted on the beads. Specifically, the simulation-predicted maximum force when the magnets make contact with the sample chamber would increase from 8.2 pN using a microscope slide and a coverslip to 42.6 pN using two coverslips. It is important to note that while high forces are desired for certain experiments, in practice direct contact between the magnets and the sample should be avoided to prevent potential damage to the objective lens situated immediately below the

sample chamber. It is also important to note that chambers with two coverslips are much more fragile than those including a glass slide.

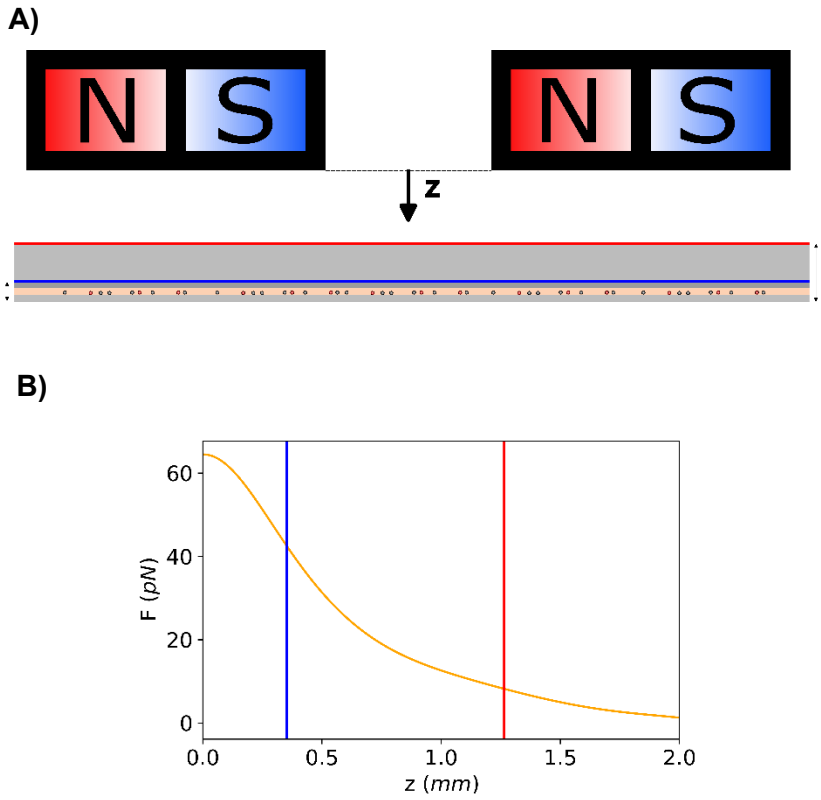

Figure 2-10 Forces from simulations.
A) Representation of the magnets and the beads inside a chamber made of a coverslip, double-sided tape, and another coverslip (blue line) or a microscope slide (red line), not to scale. If the chamber is made of two coverslips the distance between the top surface of the bottom coverslip and the top surface of the top coverslip is 0.351 ± 0.002 mm, and if the chamber is made of a cover slip and a microscope slide the distance between the top surface of the bottom coverslip and the top surface of the microscope slide is 1.264 ± 0.006 mm. B) Force on amine beads from the edge of the magnets (z=0 mm) from simulations. The vertical lines in the force plots represent the minimum distance from the magnets' edge to the lower surface within the sample chamber: the blue line represents a chamber assembled with two coverslips and the red represents a chamber assembled with a microscope slide and a coverslip.

One interesting and important result that arose from this analysis is that a change in the magnetic field direction occurs at a larger magnet-sample distance (Figure 2-11). Consequently, beyond this threshold —occurring at 7.1 mm and 2.2 mm for the measured and simulated fields respectively — the force will push the bead downward. Therefore, to provide a force that always stretches the tethered molecule in our setup, the experiments should be conducted within a range of 7.1 mm from the edge of the magnets.

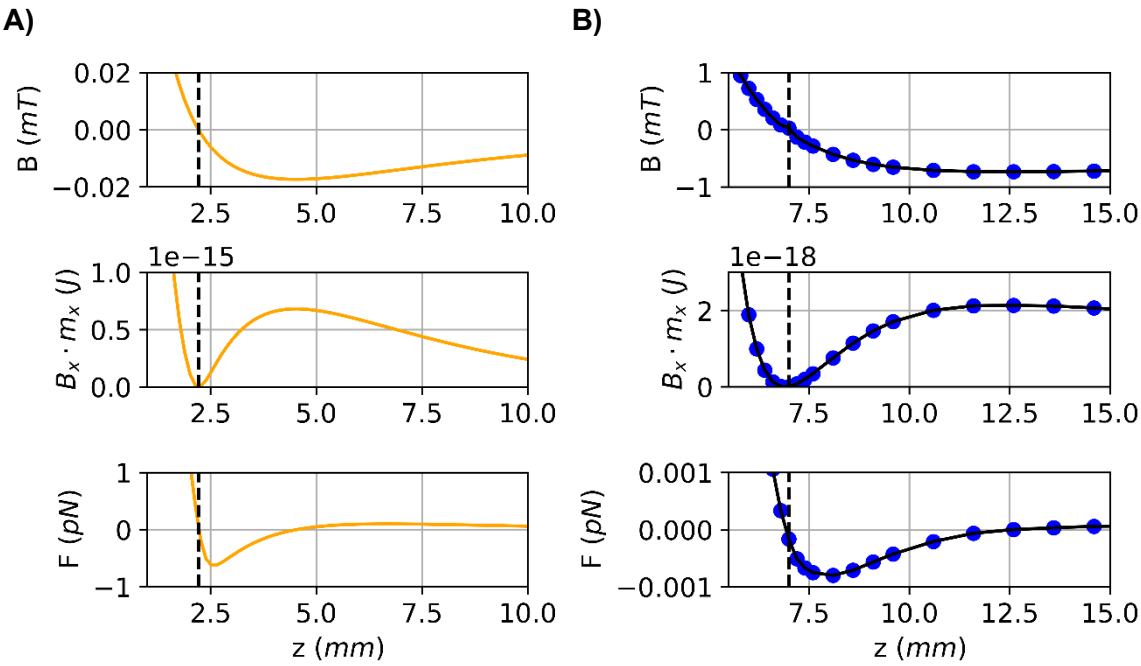

Figure 2-11 Region where the magnetic field changes direction.
Close-up highlighting the region where the force and magnetic field change direction when amine beads are used. A) Calculations derived from simulated magnetic field. B) Calculations derived from measured data (depicted by blue dots) with 20-degree polynomial fit (continuous black line). The dotted lines indicate transition points: 2.2 mm for the simulated field and 7.1 mm for the measured field. Here, a positive force pulls the bead up and a negative force pushes the bead down against the glass surface.

2.2. TIRF

One of the objectives of the overarching project is to detect binding events of other molecules to the tethered polymer. The technique selected for that purpose is TIRF microscopy. While this is not the focus of my thesis, it is a part of the instrument and so I describe it briefly here.

Our instrument has two methods of introducing the excitation light via total internal reflection, as shown in Figure 2-12. The first method uses a quad-band optical component (Chroma, ZT 405/488/561/640 rpcv2-uf2) that selectively reflects the laser lines towards the objective lens. The objective lens redirects the light to create an incident angle greater than the critical angle at the interface between glass and water (or buffer). Subsequently, fluorescent light emitted by the sample is captured by the objective lens and transmitted through the quad-band optical component. The second method uses two micromirrors: one to direct the excitation light toward a side of the

objective lens to achieve the necessary incident angle for TIRF, and the other to collect the laser light reflected at the interface between the glass and water. The main advantage of the second method is its capacity to use the light collected from the second micromirror and direct it to a Quadrant Photodiode (QPD; Thorlabs, SM2CP2). This could be used to create feedback with the piezoelectric system that controls sample height to maintains its stability with respect to the objective lens and hence also the desired incident angle of excitation.

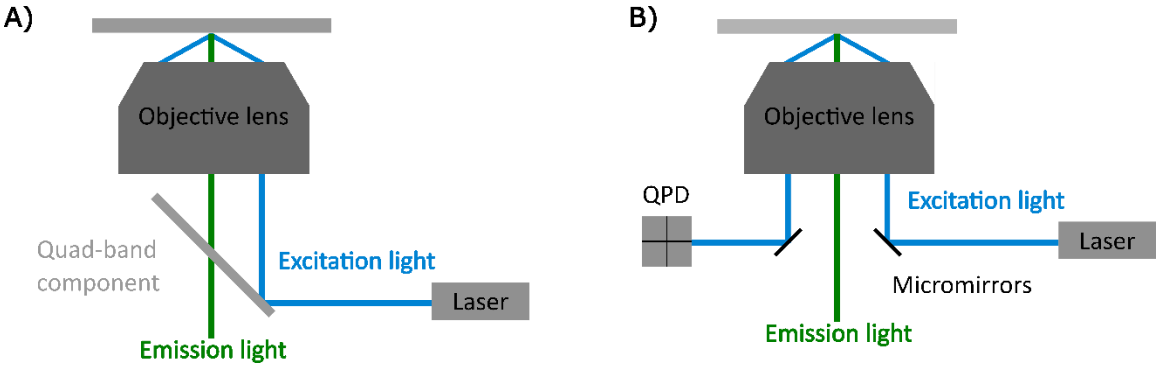

Figure 2-12 TIRF approaches.
This figure shows two ways that our instrument could achieve TIRF: (A) with the use of a dichroic mirror, and (B) with the use of micromirrors that include a feedback control with a QPD and a piezo stage to maintain the desired incident angle.

The reason that TIRF microscopy was chosen as the fluorescence microscopy method is that it can be easily combined with MT to detect binding events while simultaneously applying tension to the polymer. However, the superparamagnetic beads used for MT have autofluorescence that could potentially mask the signal from fluorophore-tagged molecules binding to collagen. We can address this by using a long DNA linker to position the tethering bead sufficiently far above the interface that the beads won't be significantly excited (Figure 2-13, right bead). Consequently, the background fluorescence from the bead will be minimized, facilitating the desired detection of single-molecule binding events. The length of the DNA tether required will depend on the extent of bead autofluorescence and the decay length of the evanescent field.

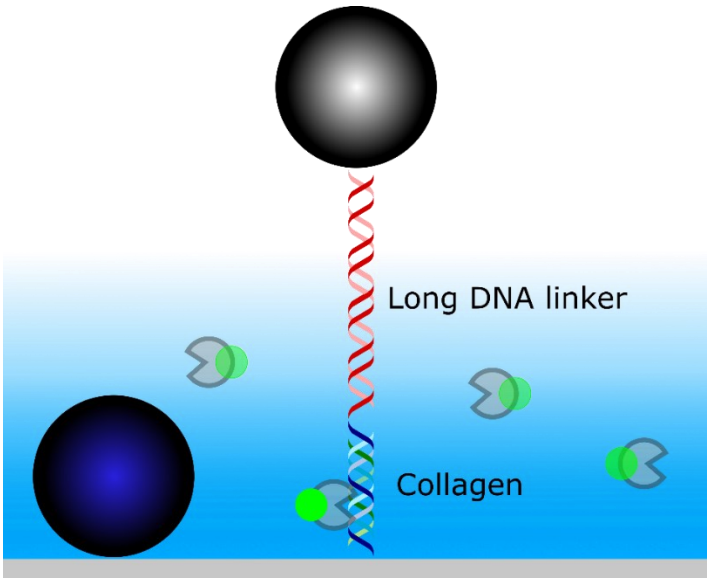

Figure 2-13 Effect of evanescent wave excitation on planned experiments. This image depicts a bead that has autofluorescence because is within the reach of the evanescent wave (left), and another one that is out of reach (right). It also includes binding molecules (Pacman shapes) and the fluorescent labels excited to different extents by the evanescent wave.

When total internal reflection happens at the boundary between two media with different indices of refraction, an evanescent wave is produced. The intensity of the transmitted wave decays exponentially with distance (Figure 2-13) as:

$$I(z) \propto e^{-\frac{z}{d_0}}, \quad [10]$$

where z is the distance from the interface and d_0 is the penetration depth[74,76,77]. Penetration depth depends on the index of refraction of the two media (n_1, n_2), the wavelength of the light in vacuum (λ), and the incident angle (θ)[74,76]:

$$d_0 = \frac{\lambda}{4\pi\sqrt{(n_1)^2 \sin^2\theta - (n_2)^2}}, \quad [11]$$

The penetration depth of the evanescent wave is presented in Figure 2-14 for the interface between water (n = 1.33) and glass (n = 1.51) at an incident angle of 63°, which is slightly above the critical angle (θ_c = 62.46°) calculated with Snell's law and for the four different laser lines in our instrument. While it is important to consider that the refractive index varies with wavelength, this variation was not included in my calculations. In both media—water[124] and borosilicate glass[125]—the change in refractive

index is less than 1% over the wavelength range of interest, making this effect negligible for our purposes.

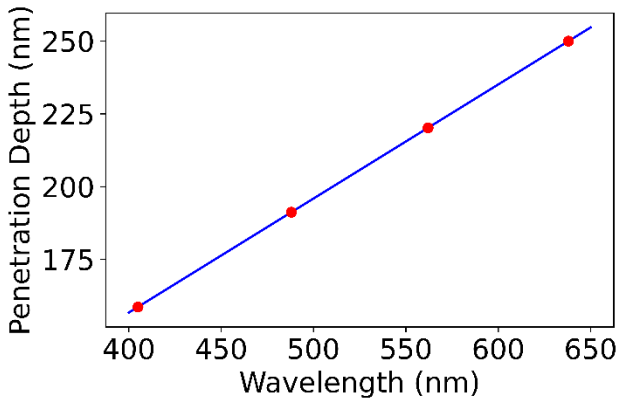

Figure 2-14 Penetration depth at different wavelengths.
The red points represent the laser wavelengths that we currently use: 406 nm, 488 nm, 562 nm, 638 nm and their respective penetration depths calculated for an incident angle of 63° using equation [11]: 244 nm, 294 nm, 338 nm and 385 nm.

The penetration depth is in a range similar to the length of a fully extended collagen molecule (300 nm), indicating that a DNA linker is essential to extend the bead well past the penetration depth and minimize the autofluorescence of the beads during binding dynamics measurements. Our ultimate aim is to have a tethered polymer of sufficient length to position the bead beyond the evanescent wave's excitation zone, as illustrated in Figure 2-13. Ideally, this tether will have collagen at the bottom and a DNA handle on top. With this configuration, the fluorescently labeled molecules binding to collagen would be close enough to the surface to be excited by the evanescent wave, allowing the camera to detect and track binding events. These events will be monitored by identifying increases in signal intensity in regions where molecules bind, which will contrast with the signal patterns observed when molecules diffuse in the sample.

Chapter 3.

Tethering of DNA

The ultimate aim of the broader project is to test the binding events of other molecules to collagen. To achieve that, it is crucial to develop a reliable tethering protocol. This protocol aims to bind one end of collagen to the glass surface, its other end to DNA, while the DNA free end subsequently binds to a magnetic bead as shown in Figure 2-13. Unfortunately, challenges encountered by different members of our research group in achieving the desired tethering of collagen and DNA constructs shifted my focus. I redirected my efforts towards exploring alternative approaches, specifically testing the tethering of only DNA.

For this thesis, I wanted to tether DNA with one end connected to the glass surface and the other end to a magnetic bead. I tried two different approaches, shown in Figure 3-1:

A. Approach A uses a 1-kilobasepair (kbp) DNA with a thiol group at one end and an amine group at the other end.

B. Approach B uses a 2 kbp DNA strand with a thiol group at one end and a biotin at the other end.

Detailed protocols are provided in Appendices C-D.

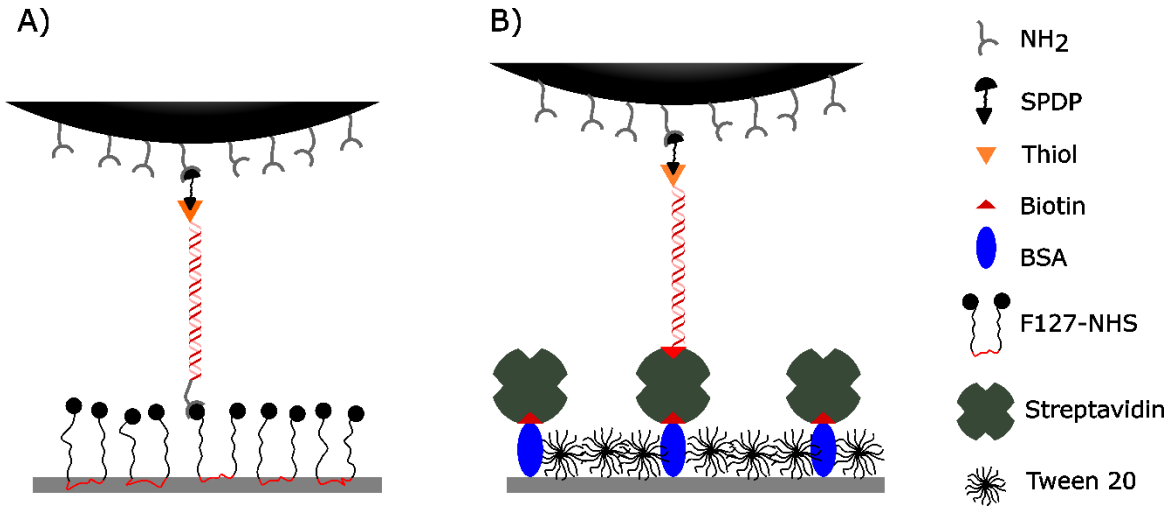

Figure 3-1 Two tethering approaches.
In Approach A, F127-NHS is used to functionalize the glass surface, and a 1 kbp DNA with an amine on one end and thiol on the other end is used to tether the amine bead to the sample. In Approach B, biotinylated BSA and streptavidin are used to functionalize the glass surface, and a 2 kbp DNA with a biotinon one end and thiol on the other end is used to tether the amine bead to the sample.

A critical consideration for the tethering process is ensuring the specific binding of each element. In our setup, it is important that the beads primarily bind one end of the DNA, while the other end primarily binds to the glass surface. To prevent non-specific binding of the beads to the glass surface, we chemically treated both the beads and the glass surface to minimize any undesired attachment of the beads to the glass substrate.

3.1. Bead treatment

The bead treatment protocol was the same for both approaches, based on previous work in our group, Kirkness et al.[126], and it is detailed in Appendix C.

I used superparamagnetic beads with amine groups on the surface (Dynabeads™ M-270; diameter 2.8 µm). These beads without any treatment have a non-specific interaction with the glass and bind to it. To minimize binding to the glass and functionalize them for further specific binding to the molecule of interest, we treat them with a two-step process using Succinic Anhydride (SA) (Sigma-Aldrich: 239690) and Succinimidyl 3-(2-PyridylDithio) Propionate (SPDP) (Thermo Fisher: 21857). SPDP has an NHS ester group at one end that reacts with the amine groups on the beads forming a covalent bond. At the other end, it has a pyridyl disulfide group that reacts with thiol at the 3' end of the DNA creating a covalent bond between them. Previous studies

in our research group[126] have determined that a single-step process using only SPDP will not properly block the non-specific binding of beads to the glass sample treated with F127-NHS, because some amine groups on the beads remain unreacted and available to react with surface-presented NHS groups. A two-step process of reacting the beads with SA after SPDP enhances the blocking of non-specific binding. SA has an NHS ester group on one end that covalently links to the free amine groups on the beads, and presents a carboxylic acid group at its other end. These two modifications to the surface of the beads should prevent their off-target binding to the surface.

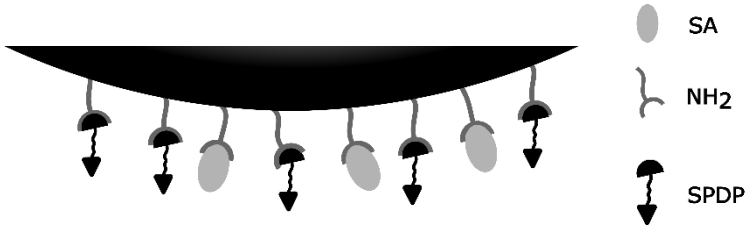

Figure 3-2 Two-step bead treatment using SA and SPDP.
The NH_2 groups on the beads are either reacted with SA to create blocking groups or linked to SPDP via pyridyl to create reactive groups.

It is important to note that the SA treatment might not be necessary for Approach B. However, I used the two-step process because previous results[126] indicate that when F127 without the NHS group is used on the glass surface, the two-step process involving both SA and SPDP is more effective at blocking non-specific binding compared to using just SPDP.

3.2. Glass surface treatment

Both tethering approaches that I used for my thesis, require a hydrophobic glass surface. The first step involves cleaning the glass surface using a protocol that includes a sequence of sonication steps: first in water, second in a mixture of hydrochloric acid (HCl) and ethanol (CH_3OH) in a 1:1 ratio, and third in sulfuric acid (H_2SO_4). The second step aims to create a hydrophobic surface using Sigmacote®. Detailed protocols for glass cleaning and hydrophobic surface treatment can be found in Appendix B and are adapted from Kirkness et al.[126]. The subsequent steps use different chemicals for the two tethering approaches and are detailed in Appendix C.

3.2.1. Approach A

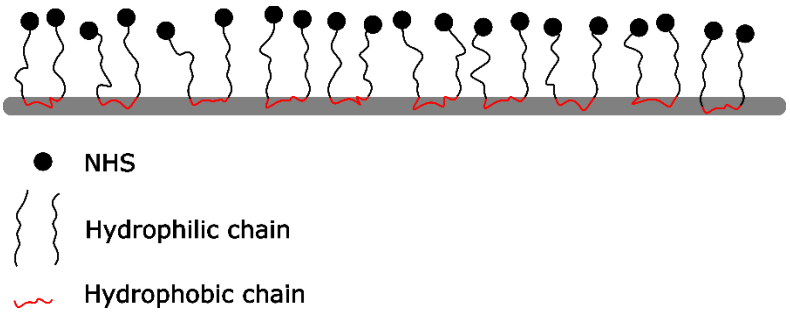

Figure 3-3 Glass functionalization approach A using F127-NHS.
Pluronic F127 is a non-ionic tri-block copolymer that contains two hydrophilic poly(ethylene glycol), PEG chains on the sides and a hydrophobic poly(propylene glycol), PPG chain in the middle [127]. Pluronic F127-NHS is end-functionalized with N-hydroxysuccinimide (NHS).

This tethering approach avoids the use of proteins, which is advantageous for studying the enzymatic cleavage of collagen, an area of interest in our lab. Using proteins to tether could complicate the analysis because enzymes might cleave these tethering proteins (e.g., streptavidin or BSA), making it difficult to determine whether collagen or proteins involved in the linkage are being cleaved. In the approach here, we use a polymer called F127-NHS (Polymer Source™: P40768-EOPOEO-2NHS), which has a hydrophobic central chain and two hydrophilic chains at the ends. Under the right temperature and pH conditions, F127-NHS forms a brush-like structure on a hydrophobic glass surface[126,128]. When this brush is formed, NHS ester groups are presented at the ends, illustrated as circles in Figure 3-3. The DNA, which has an amine group at one end, can then react with one of these NHS ester groups to form a covalent bond.

3.2.2. Approach B

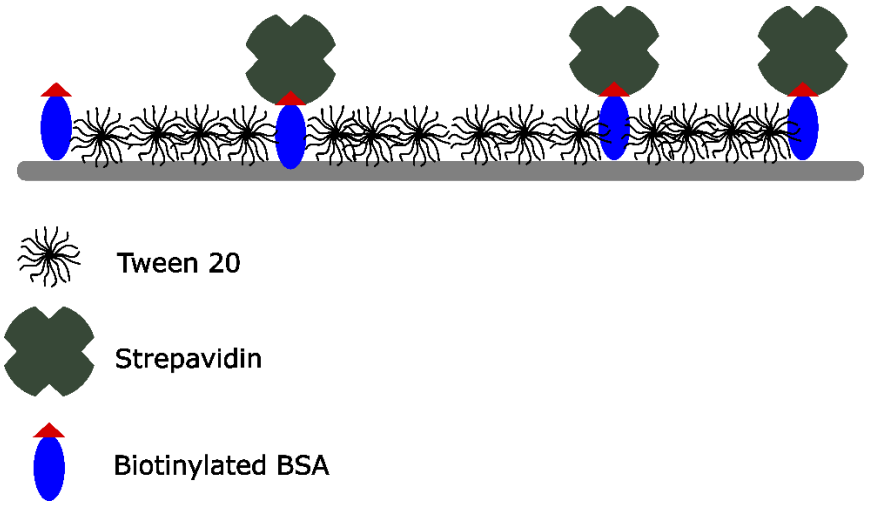

Figure 3-4 Glass functionalization approach B.
This figure shows the functionalization of the glass surface for Approach B which uses biotin-streptavidin linkages. Tween 20 blocks the non-specific binding in regions between biotinylated BSA proteins affixed nonspecifically to the hydrophobic surface.

In this approach, I implemented a procedure that involves a protein-based tether previously used in our laboratory[42]. To tether the biotinylated end of the DNA to the sample, biotinylated BSA (Sigma A8549) is first applied to the hydrophobic glass surface. The glass is then treated with Tween 20 (Sigma-Aldrich: P7949) (or Pluronic F-127, Sigma-Aldrich: P2443) to minimize the non-specific binding of beads to the hydrophobic surface[129,130]. Afterward, streptavidin is introduced, which can bind to the biotin on BSA. Once streptavidin is on the surface, the biotin on the end of the DNA can bind to it (each streptavidin protein has four biotin-binding sites). The final result is the DNA being attached to the glass surface via biotin-streptavidin interactions. The details of the procedure can be found in Appendix C.

3.3. MAGIC Assay

The microsphere adhesion by gravity, inversion, then counting (MAGIC) assay was previously developed to quantify the success of bead-tethering strategies[126]. This approach can be used to address the specific and non-specific binding of microspheres to the surface of a chamber independently of the bead concentration and size, which is a huge advantage in testing tethering assays. I have used it to test the non-specific

binding of the beads to a glass sample and assess the effectiveness of the DNA tethering procedures.

For this assay, treated microspheres are first flowed into the sample chamber and allowed to interact via gravity with the coverslip, which is initially the bottom surface (Figure 3-5). After 20 to 30 minutes, the sample is flipped, making the coverslip the top surface. Waiting for 5 to 10 minutes allows any unbound spheres to be pulled by gravity and settle onto the microscope slide, which is now the bottom surface. Images of 5 to 10 random locations on both the top and bottom surfaces of the sample are then captured using bright field imaging with an inverted microscope (Olympus IX83) with a 10X objective lens.

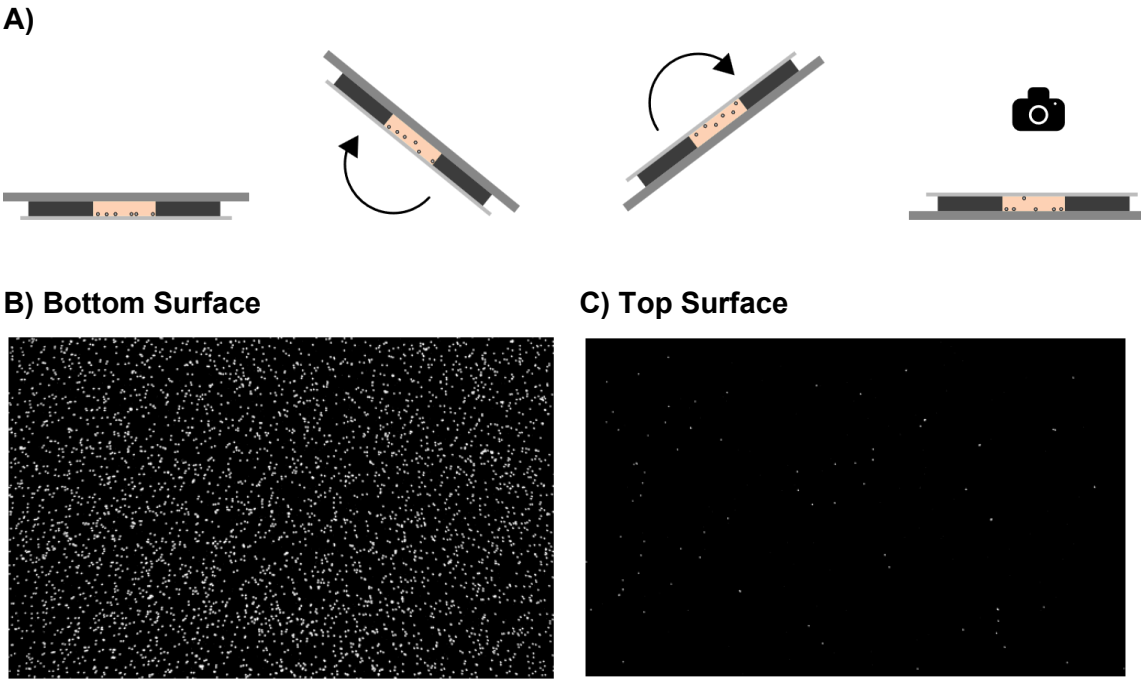

Figure 3-5 MAGIC assay steps.
A) The first step of the MAGIC assay is to let the beads settle on the coverslip and interact with the functionalized surface. The second step is to rotate the sample so that the coverslip, initially at the bottom, comes to the top. The next step is to capture images of both the top and bottom surfaces after flipping. The final step is to count the number of beads on the top and bottom surfaces and calculate the percentage of beads remaining on top to assess the effectiveness of specific binding or the blocking of non-specific binding. (B) and (C) show an example of the bottom and top surfaces respectively of carboxyl beads in an F127-NHS treated sample after the images are processed to be binary as described in Appendix D. The field of view is approximately 1.8 mm x 1.1 mm. In this example, the number of beads on the top surface is 53 and at the bottom is 1955. The percentage of beads remaining on the top surface is thus $(\frac{53}{1955+53}) * 100 = 2.63\%$.

After acquiring images of both surfaces, a Python script (described in Appendix D, Figure D-1) developed by group member Koushik Bar is used to count the number of beads on the top and bottom surfaces. The percentage of beads that remain on the top surface indicates the effectiveness of the specific binding or blocking of non-specific binding.

3.4. Tethering Results

Many experiments were conducted for each approach. Fifteen experiments were performed using Approach A, which involves F127-NHS to tether the beads using DNA. These experiments were conducted in collaboration with Koushik Bar, another graduate student in our research group. I am not presenting all the MAGIC assay data collected in this period, as early experiments may contain human errors resulting from the initial learning process.

We initially tried to test the whole construct, following the procedure described in Appendix C. It includes the treatment for the non-specific binding of the beads using SA and SPDP, the linkers between the bead and the DNA, and the linker between the glass sample and the DNA. We expected that the construct with all the components should have been tethered (high percentage at the top surface) and the one without the DNA should have been not bound to the coverslip (low percentage at the top surface); however, that is not what we found (Figure 3-6).

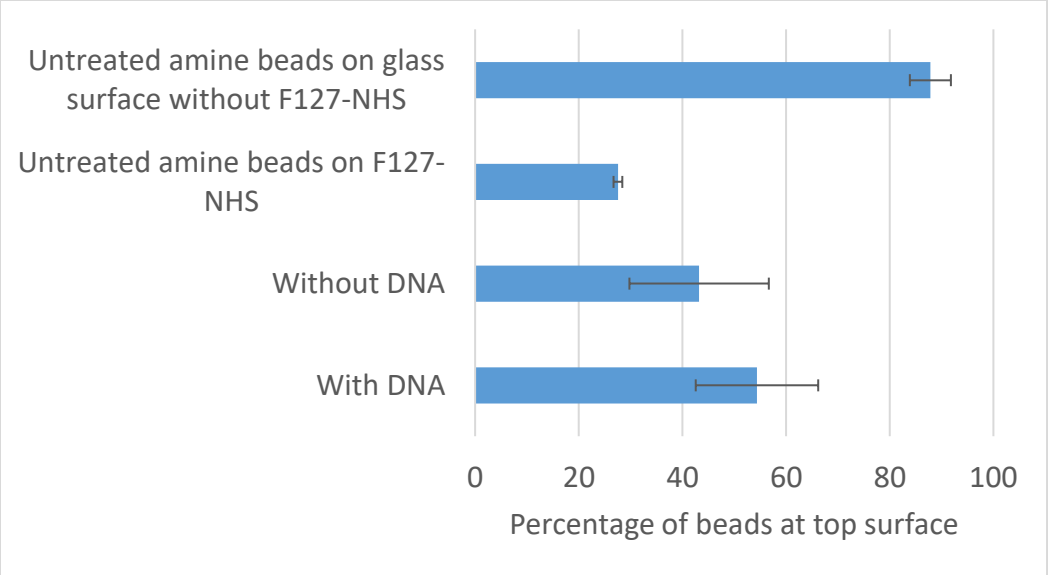

Figure 3-6 First set of results using approach A.
This figure shows the percentage of beads remaining on the top surface after flipping; the error bars are standard deviations. There are four kinds of samples: one has every part of the tethering construct (With DNA), and another one has the beads and the glass surface treated but it does not have DNA (Without DNA). The other two have amine beads that were not treated: one is with glass treated with F127-NHS and the other one has no subsequent treatment of the hydrophobic glass. Each bar represents one sample and three images of the top and bottom surfaces were taken.

We conducted several experiments to identify the cause of the inconsistencies observed. First, we created various control samples to evaluate the effectiveness of the SA treatment. Instead of using the standard SA+SPDP treatment, we applied two treatments of SA, which effectively converted our amine beads into carboxyl beads. In all these samples, non-specific binding was blocked (Figure D-2).

Next, we tested the functionality of our original batch of F127-NHS by comparing it to a newly acquired batch. There was no significant difference between them, as shown in Figure 3-7, indicating the F127-NHS was not the issue. (We expected to see a high percentage retained on the top surface for amine beads on F127-NHS and a low percentage for amine beads on F127.) Then we questioned the reliability of our amine beads. The original batch was from Thermofisher (Dynabeads® M-270). Therefore, we acquired new amine beads (ProMag® 3 Series · NH2) from a different provider (Bangs Laboratories Inc.), but the new beads also showed inconsistency, as shown in Figure 3-7. Similarly, we compared old and newly acquired batches of SPDP, but found no significant differences, indicating that SPDP was not the issue.

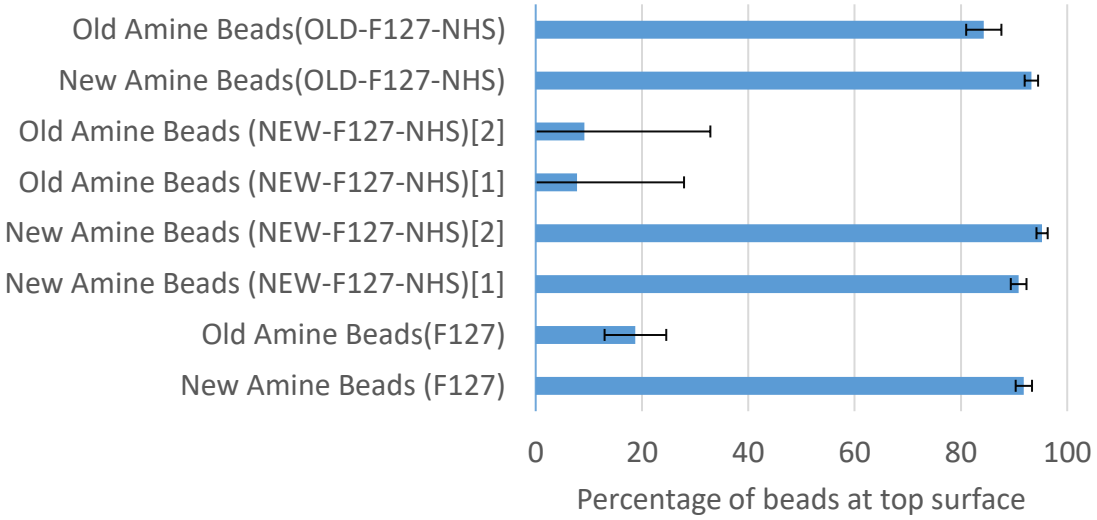

Figure 3-7 Testing different batches of F127-NHS and amine beads.
This figure shows the percentage of beads remaining on top after flipping, the error bars are standard deviations. Old Amine beads are Dynabeads® M-270, and New Amine beads are newly acquired ProMag® 3 Series · NH2. Also, newly acquired F127-NHS, the old batch of F127-NHS, and F127 without NHS are compared. Three images of the top and bottom surfaces were taken in each sample chamber (row of plot).

To rule out other potential chemical groups that might be interfering with the reactions involved in the tethering, we used NMR spectroscopy to analyze the F127-NHS and the SPDP performed by Eric Ye in the chemistry department. The results confirmed the absence of unexpected chemical groups that could interfere with the reactions.

Given that in Approach A the formation of a brush with F127-NHS is necessary and the formation of this structure is sensitive to variations in pH, temperature, handling procedures, and hydrophobicity of the surface[126,128]. I decided to test an alternative method that should be less sensitive and does not require the formation of a brush (Approach B) because it uses Tween 20 to passivate the glass surface[129,130].

MAGIC assays for Approach B, which uses biotin and streptavidin at the base of the tether (detailed in Appendix C), were conducted 11 times. For these experiments, I used DNA that is 2075 bp in length with biotin and thiol end-labels, provided by Derek Dee's lab at UBC. The sequence of the DNA can be found in Appendix E. I concentrated and purified the DNA by using a precipitation method following[131], and confirmed the purity using the DNA UV-vis absorbance spectra, as shown in Figure E-3. Also, I

calculated the concentration (1765 μg/ml) using this spectrum and the Beer-Lambert law ($A = \varepsilon lc$) where A is the absorbance, ε is the molar extinction coefficient (50 ml/μg*cm), l is the path length and, c is the concentration. To confirm that the DNA had the expected 2 kbp length, I performed agarose gel electrophoresis as shown in Figure E-4.

During this period, I ensured the technical aspects of the procedure were carefully executed, minimizing the likelihood of human error. I employed various controls to test different components of the tether to confirm their functionality. I tested for non-specific binding of the beads using different control samples to ensure the blocking was effective. Examples of these include testing that the treatment of the glass surface with Tween 20 and biotinylated BSA was blocking the non-specific binding of beads (Figure D-3) and testing that F127 as a different surface passivation with biotinylated BSA blocked the non-specific binding with both old and new beads (Figure D-4).

After confirming that some controls were functioning properly (surface passivation of Tween 20 + biotinylated BSA (Figure D-3)) and that streptavidin beads bind to the biotinylated BSA functionalized surface (Figure D-3 and Figure D-4)), I began using the DNA for tethering. Seven tethering experiments were performed that did not reveal a clear tethering behavior; I include as examples the first (Figure D-5) and the last of those trials (Figure D-6). The only significant modification to the protocol that I made involved activating the thiol groups in the DNA. Initially, I used TCEP gel, which offers the practical advantage of easily separating the reduced DNA. However, after consulting with group members who encountered issues with this approach, I decided to switch to soluble TCEP-HCl. A crucial consideration when using TCEP-HCl is that it must be diluted in a phosphate-free buffer.

However, when performing incubation steps with DNA-free samples, inconsistencies in non-specific binding recurred (Figure D-7). Despite thorough controls and careful execution, the non-specific binding issues persisted.

These experiments led us to conclude that we should not be using amine beads due to their inconsistent non-specific binding. Variability was observed across different days, samples, and procedures. In some experiments, carboxyl beads were used as controls, and these consistently exhibited good blocking of the non-specific binding as shown in Figure 3-8. Additionally, using a two-step SA coating process on the amine

beads, which is like converting the amine beads into carboxyl beads, also resulted in reliable blocking of the non-specific binding (Figure D-2).

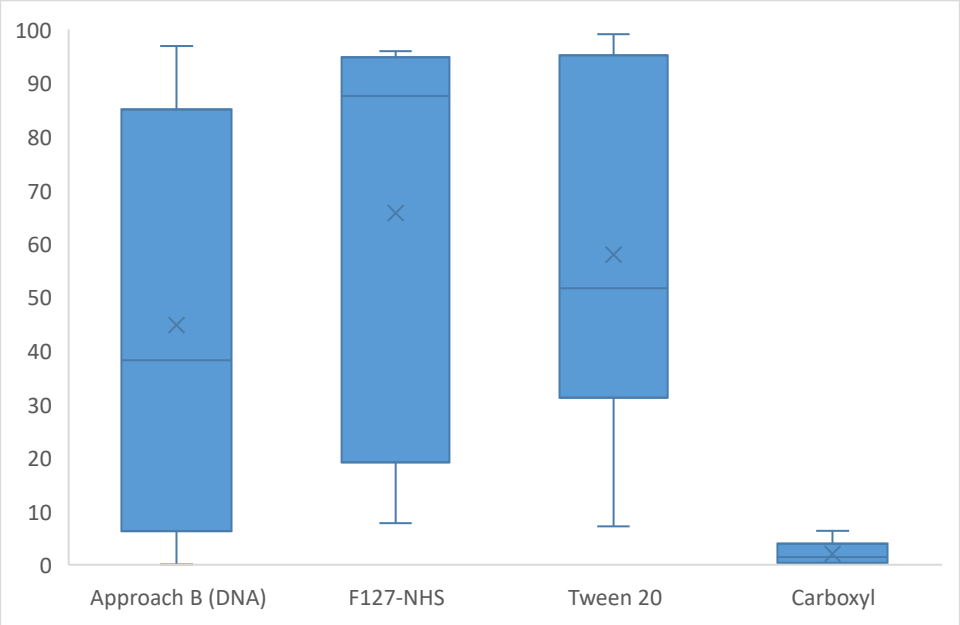

Figure 3-8 Tethering final results.
This figure shows the percentage of beads remaining on top after flipping. Four kinds of samples are shown: amine beads tethered with DNA using Approach B (n=28), amine beads without DNA over F127-NHS (n=8), amine beads without DNA over Tween 20 (n=11) compared with carboxyl beads (n=5). n is the number of replicate chambers per condition. The middle line of the box represents the median, and the x in the box represents the mean. The top line of the box represents the 3rd quartile (the median of the top half), and bottom line of the box represents the 1st quartile (median of the bottom half). The whiskers (vertical lines) extend from the ends of the box to the minimum value and maximum value.

Therefore, we decided to change our tethering procedure to use carboxyl beads instead of amine beads. This tethering study is being continued by others in our lab, who will explore similar approaches but with modified linkers to accommodate the use of carboxyl beads. Meanwhile, I proceeded with development of the MT instrumentation necessary to characterize successfully tethered DNA.

Chapter 4.

Force-extension measurements

Force-extension measurements using magnetic tweezers involve a bead that is being pulled up by a force proportional to the gradient of the product of the magnetic field and the magnetic moment of the beads (equation [7]), and is constrained by the tension of a tethered polymer. In a nonthermal equilibrium scenario, the force exerted by the magnetic field and the tension on the polymer balance out, making the bead stationary.

However, in reality the bead is affected by the thermal environment, which causes the bead's position to fluctuate due to Brownian motion. There is an effective restoring force that brings the bead back to its central position (Figure 4-1), which can be approximated as:

$$F_x = -k_x \delta x. \quad [12]$$

Using the equipartition theorem, the variance of the bead position ($\langle \delta x^2 \rangle$) and the restoring stiffness (k_x) can be related to the thermal energy ($k_B T$), where k_b is the Boltzmann constant and *T* is the temperature:

$$\frac{1}{2} k_x \langle \delta x^2 \rangle = \frac{1}{2} k_B T. \quad [13]$$

Assuming that the displacement angle θ is small for a bead tethered by a polymer, the magnitude of the restoring force can be approximated using the geometry in Figure 4-1 as

$$F_x = F_T \sin\theta \approx \frac{F_z}{z} \delta x. \quad [14]$$

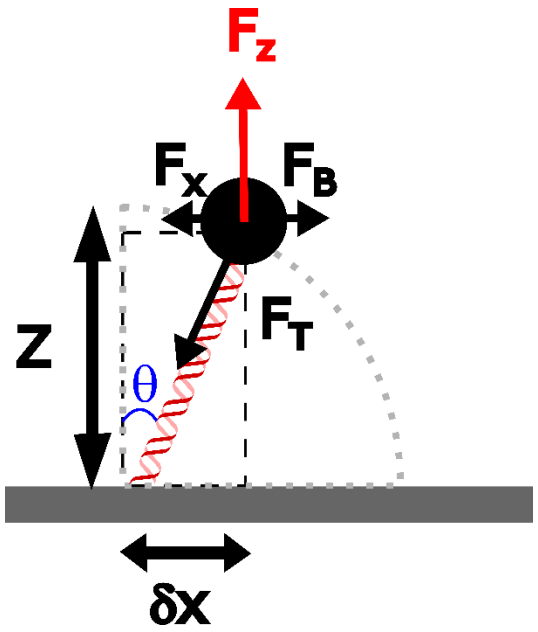

Figure 4-1 Magnetic tweezers force diagram.
Forces and geometry used to derive Equation [15] for a bead tethered via a polymer. The figure shows the force pulling up from the magnetic field (F_z), the tension generated by the polymer (F_T), the restoring force (F_x), the x-component of the force caused by the Brownian motion (F_B), the angular displacement (θ), the height of the bead that for a small angle is approximately extension of the polymer (z) and the displacement from equilibrium in the horizontal plane (δx). Schematic is not to scale.

Combining the previous equations, we can derive the standard equation used in magnetic tweezers experiments [99,1,112] that gives us the magnitude of the vertical force, using the measurable variables of temperature (T), lateral fluctuations of the bead $\langle \delta x^2 \rangle$, and bead height ($z$):

$$F_z = \frac{k_B T z}{\langle \delta x^2 \rangle}. \qquad [15]$$

Thus, to obtain a force-extension curve of a tethered polymer, one needs to know the temperature of the sample and measure the height and lateral fluctuations of the bead. In this chapter, I describe how each of these is determined and my work to improve the precision and accuracy of these measurements.

4.1. Lateral bead fluctuations

The lateral fluctuations of a bead in magnetic tweezers are an important parameter for accurately determining the forces acting on tethered polymers. To

measure these fluctuations, the lateral position (x, y) of the bead's center must be tracked at each time point. Particle tracking methods can be classified in different ways[132]; for example, into two groups[5]: direct image fitting techniques, such as Gaussian fitting[133,134], and reference image-based techniques, such as cross-correlation[135] or self-convolution[109]. In our experiments, the lateral position of the bead is determined by cross-correlation, using an approach implemented in LabVIEW by Michael Poirier's group at The Ohio State University[136,137]. This method correlates bead positions across sequential frames, allowing for sub-pixel resolution of the bead's lateral motion. In section 4.1.2, I will explain the method in more detail. However, several other tracking methods have been developed and used across the field, each with its own strengths and weaknesses, I will briefly discuss some of them here.

4.1.1. Particle-Tracking Methods

Numerous tracking algorithms have been developed over the past decades, with significant variations in precision, robustness, and computational complexity[138]. Although comparing these tracking algorithms can be challenging because they are often optimized for specific scenarios, Chenouard *et al.*[139] provided a comprehensive comparison through an open competition. In their study, 14 different tracking algorithms were evaluated for particle-tracking performance across standardized datasets, using synthetic data that mimicked real biological conditions. A key conclusion of their study was that no single method consistently performed best in all cases. I will highlight some key parts of the approaches that in my opinion are relevant for tracking particles like the magnetic beads used in our magnetic tweezers setup.

- Non-fitting methods: One of the simplest methods to track a particle is using a center of mass (COM) algorithm that calculates the average position of pixels weighted by their intensity to localize the particle[133,138,140]. While computationally efficient, this method is susceptible to errors in cases where the bead is dim or its intensity profile is asymmetric. In addition to COM, other non-fitting methods have been developed that perform well in specific scenarios[141,142]. For example, radial symmetry methods offer a computationally efficient alternative for localized tracking, particularly in high-contrast images. However, COM remains effective for isolated, high-contrast particles, although it struggles in dense or noisy

environments compared to more advanced fitting techniques like Gaussian fitting.

- Fitting methods: Fitting algorithms play a crucial role in particle localization by modeling the intensity profile of a particle's image and estimating its center with sub-pixel precision. The most commonly used model is the Gaussian fitting method, which assumes that the particle's point spread function (PSF) can be approximated by a Gaussian function[133,134]. This approach is particularly effective for well-focused particles in microscopy and remains a gold standard for achieving high localization accuracy[143], especially in single-molecule tracking experiments[143]. Optimization can be performed using the least-squares criterion[133], which minimizes the difference between observed data and the model, though it is sensitive to noise. Maximum-likelihood estimation (MLE) provides a more robust alternative, maximizing the likelihood that the observed data fits the model, offering better accuracy in noisy environments at the cost of increased computational effort[144].

- Reference-image-based techniques: These methods track particle motion by comparing an image of the particle to a reference image across successive frames, allowing for sub-pixel precision in localization. Cross-correlation is one of the most widely used techniques, comparing intensity patterns between frames to detect shifts in position[135,145]. While cross-correlation is computationally demanding, the use of Fourier transforms can significantly speed up the calculations, making it feasible for real-time tracking in our setup.

In addition to the commonly used COM, Gaussian fitting, and reference-image-based techniques, other advanced approaches have been developed to improve tracking accuracy under complex experimental conditions[132,133,138]. Some of these methods integrate both fitting and correlation approaches at different stages of the algorithm, while incorporating underlying system information such as prior knowledge of constant velocity or Brownian motion. For example, Kalman filtering and Multiple Hypothesis Tracking (MHT) offer dynamic models that incorporate particle motion, noise, and uncertainty into the tracking algorithm. More recent approaches have methods used machine learning and deep learning to reconstruct images and increase tracking capabilities, and have been incorporated into STORM[146]. These methods are

particularly useful in high-noise, crowded environments, low photon counts, and blinking fluorophores. For further insights into these complex methods, Shen et al.[138], Chenouard et al.[139], Manzo & Garcia-Parajo[132], and Antun et al.[147] offer good overviews.

In this thesis, cross-correlation was used for its balance of precision and real-time performance. I tested its performance and found it to be well-suited for our experimental setup. The use of Allan deviation or power spectral density (PSD) analysis could help in further evaluation and modification of the method when tethered molecules are tested.

4.1.2. Algorithm to detect the bead fluctuations

First, the beads are selected by a region of interest (ROI) as shown in Figure 4-2. Each bead's position is tracked by capturing a sequence of images of the bead's diffraction pattern within the ROI.

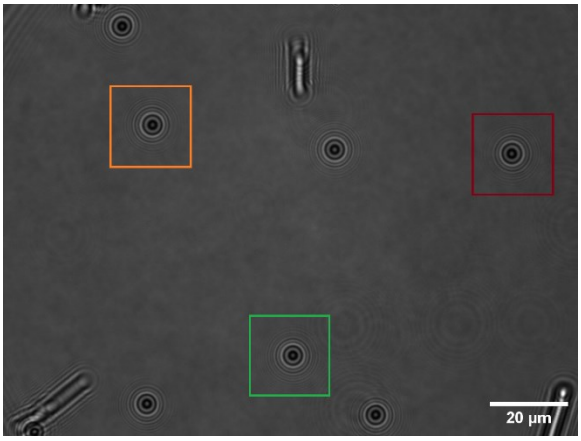

Figure 4-2 Representative image of beads in the field of view.
The full field of view is presented with three beads selected to be analyzed, enclosed by orange, green, and red regions of interest (ROI).

To determine a bead's relative position at each time point, we perform a cross-correlation between the image of the bead at a given time and another image taken at an initial time, Figure 4-3 (A). The cross-correlation technique involves one image shifted spatially (x,y) relative to another and calculating the correlation coefficient for each shift. For each shift, the cross-correlation describes how similar the values in the two images are. The point at which the correlation coefficient is maximized indicates the lateral displacement of the bead ($\delta x, \delta y$) (Figure 4-3 (A)).

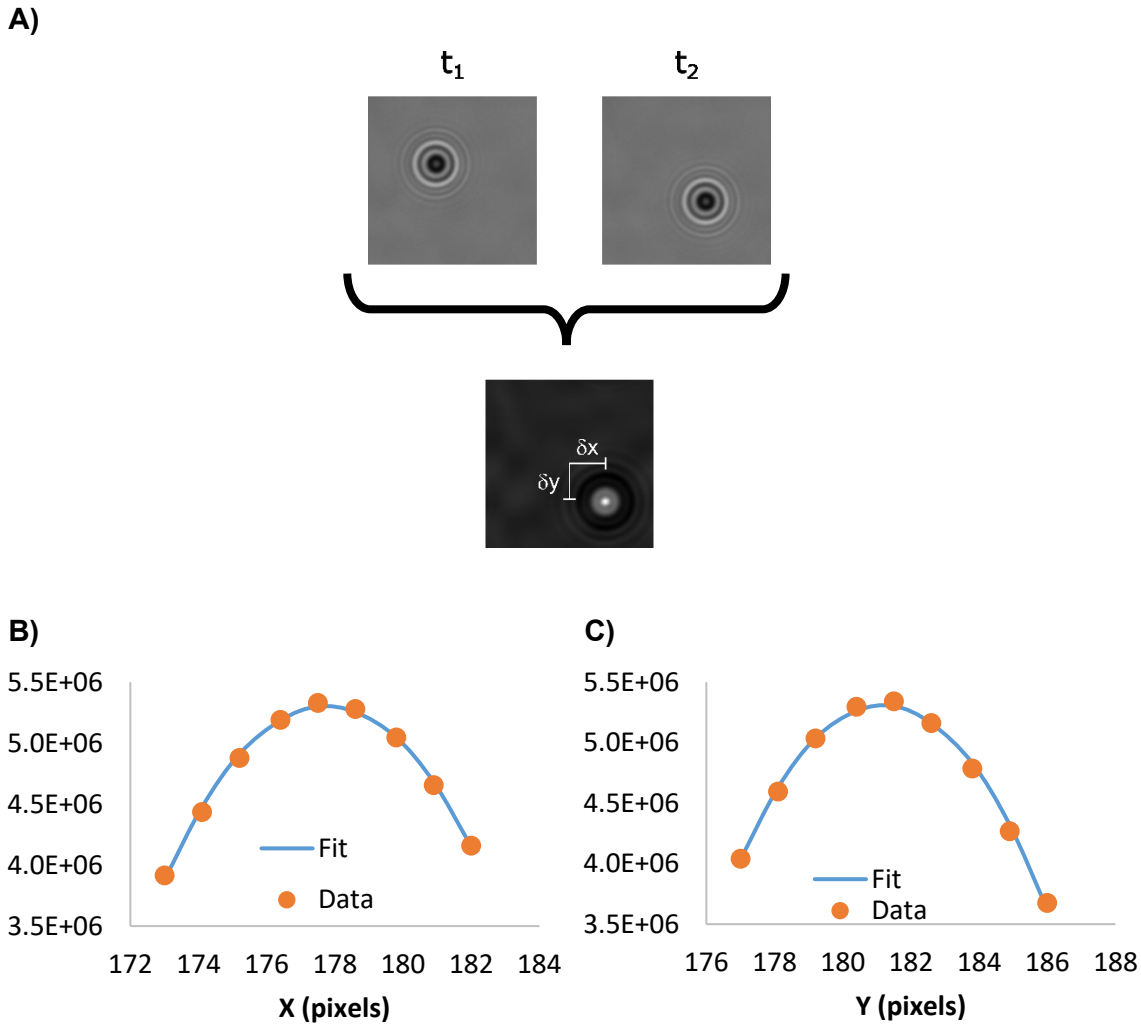

Figure 4-3 Cross-correlation of bead shifted spatially (x,y).
A) Two images of a displaced bead at different times (t_1 and t_2), along with the result of the cross-correlation between them, indicating the displacement ($\delta x, \delta y$). (B) and (C) display the cross-correlation coefficient and the second-degree polynomial fit for 9 points near the maximum cross-correlation, for offsets along the x and y axis, respectively.

The cross-correlation is calculated in reciprocal space using a Fast Fourier Transform (FFT) as:

$$(f * g) = \mathcal{F}^{-1}\left[\overline{F(\omega)}G(\omega)\right], \qquad [16]$$

where $(f * g)$ is the cross-correlation, $\mathcal{F}^{-1}$ is the inverse Fourier transform, $G(\omega)$ is the Fourier transform of g and $\overline{F(\omega)}$ is the complex conjugate of the Fourier transform of f.

The LabVIEW code and a more detailed explanation of the cross-correlation are in Appendix F (Figure F-1).

In the algorithm developed in Poirier's lab, to reduce the noise and find the center after the cross-correlation, three rows near the center are averaged to find the x-position and three columns near the center are averaged to find the y-position. Nine points around the maximum of these averaged profiles are fitted to a 2nd-degree polynomial function to find the center (Figure 4-3 (B) and (C)). The center of the cross-correlation is taken as the maximum point in the 2nd-degree polynomial fit. This marks the relative lateral position of the bead at that timepoint, which is saved with its respective time stamp in a vector as (t_i, x_i, y_i) for later analysis.

When the lateral position (x_i,y_i) of the bead is determined for each time point, the next step is to calculate the lateral fluctuations. The lateral fluctuations are quantified by the variance in the bead's position, denoted as $\langle \delta x^2 \rangle$ for the *x*-direction and $\langle \delta y^2 \rangle$ for the *y*-direction. This variance represents the extent of the bead's movement due to Brownian motion and is calculated to quantify the spread of the distribution of *n* number of (*x,y*) positions over time as:

$$\langle \delta x^2 \rangle = \frac{\sum (x_i - \bar{x})^2}{n-1}. \qquad [17]$$

The variance is inversely proportional to the force exerted by the magnetic field on the bead, as in Equation [15]. Identification and characterization of the lateral fluctuations is necessary to ensure that only thermally induced fluctuations are used to determine the force. Thus, it is important to correct for sample drift and other systematic factors that might influence the measured fluctuations.

In the next section I present some results of the lateral fluctuations of fixed beads, their respective variance and its characterization.

4.1.3. Analysis of lateral bead fluctuations

To characterize detected fluctuations and identify potential nonthermal noise and drift in our system, I used fiduciary beads (stuck to the sample surface). The beads were immobilized by allowing them to settle on a chamber placed over permanent magnets,

resulting in the beads nonspecifically binding to the glass surface. Figure 4-4 shows examples of beads whose position was tracked. In these experiments, neither the piezo stage nor the magnets was moved; however, some movement of the beads is noticeable over large periods of time (several minutes), presumably due to drift of the sample chamber relative to the imaging optics.

I used the standard deviation of the bead's position to quantify the precision of the bead tracking. It is calculated as the square root of the variance. I measured the standard deviation for 54 different beads taken on six different days at the same magnet height (approximately 4 mm from the sample). The mean standard deviation was 43 nm, with individual values ranging from 7 nm to 106 nm. This wide range of standard deviation is expected because the exact nature of the bead's attachment to the sample (nonspecific binding) is unknown, resulting in different trapping stiffness.

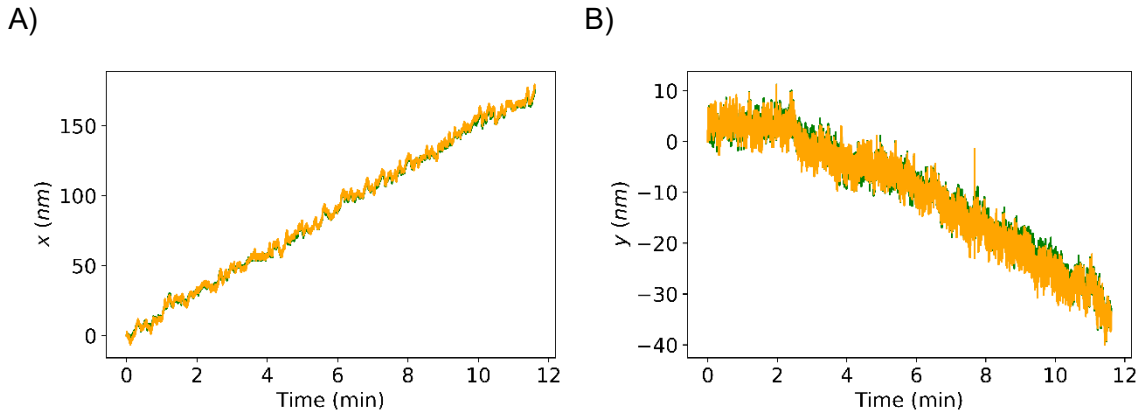

Figure 4-4 X and Y positions of fiduciary beads.
The x-x_0 (A) and y-y_0 (B) positions within the ROI (size of approximately 22 µm) are shown for two different beads (labelled as “green” and “orange”) that appear superimposed in the graphs. In each plot, the positions of two beads were tracked, with an average frame rate of 46.2 frames per second.

There are different ways to correct for sample drift. The most straightforward method is to use a fiduciary bead during a measurement to correct for sample drift that also affects the measured positions of the beads under study[109,148] (e.g. those that are used to exert force on a tethered polymer). Figure 4-5 shows an example of a correction done by subtracting one bead position from the other, mimicking the use of a fiducial bead in a measurement of tethered particle motion. The result is a relative displacement fluctuating around zero, implying that stage drift has been well corrected. The mean

standard deviation over 27 measurements, where the position of one bead was subtracted from another, is 11 nm, with individual values ranging from 3 nm to 20 nm. As expected, this value is lower than the standard deviation without subtraction, indicating that large-scale fluctuations (presumably due to drift) were effectively eliminated.

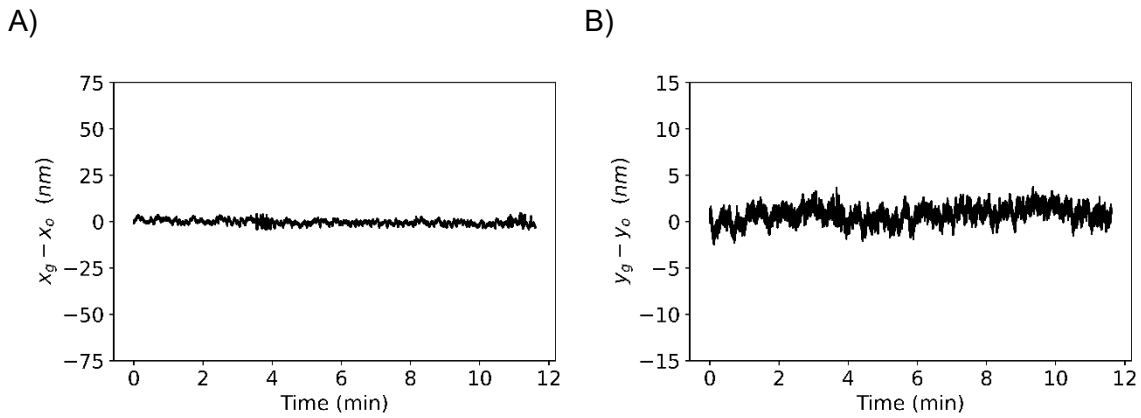

Figure 4-5 Relative displacements of a stuck particle.
Using the same measurements as in Figure 4-4, here, the position of the orange bead was subtracted from the green at each timepoint in *x* (A) and *y* (B). The ranges of the vertical axes are the same as in Figure 4-4.

For the calculation of the variance (plotted as the standard deviation in Figure 4-6) I used an overlapping method: the data is divided into segments of equal duration (τ) that incremented $\tau = 0.005\ s, 0.010\ s, 0.015\ s$ ... ; the variance for each value of τ was calculated as

$$\sigma^2{}_\tau = \frac{\sum_{j=0}^{N-1} \sigma^2(j\tau,(j+1)\tau)}{N}, \qquad [18]$$

where $\sigma^2(t_1, t_2)$ is the variance calculated from t_1 to t_2, and *N* is the number of $\sigma^2(t_1, t_2)$ calculated per τ. Then the standard deviation σ (the square root of the variance) was plotted as a function of those time intervals τ. From Figure 4-6, we see that the effects of drift (long-time noise) are diminished when the position of one bead is subtracted from another, as seen by comparing the black to the orange line. These coincide at short times, indicating uncorrelated bead motion.

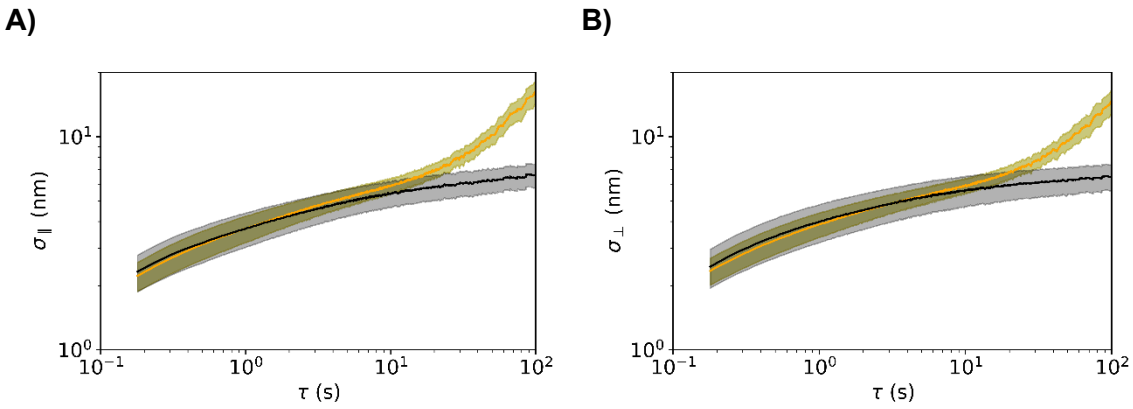

Figure 4-6 Standard deviation of stuck bead positions for different τ.
Standard deviation parallel ($\sigma_\parallel$) (A) and perpendicular ($\sigma_\perp$) (B) to the field calculated for the same sample chamber, with 10 different measurements, and two beads tracked per measurement. The magnets were positioned 4 mm away from the sample and rotated to alter the direction of the magnetic field relative to the sample. The green and orange lines (which are superimposed) represent the standard deviation of the positions based on raw data, while the black line represents the subtraction of the lateral positions of the two beads. The shaded regions indicate the standard error of the mean standard deviation across the 10 different measurements.

A useful method for characterizing drift over time is the Allan variance[99,148–150], which analyzes the stability of a signal. Unlike normal variance, which increases with time as noise accumulates, even at shorter time scales as seen in Figure 4-6, Allan variance often flattens or decreases at specific time intervals. This behavior reveals distinct noise characteristics that are otherwise hidden in traditional variance analysis, making it especially useful for identifying optimal time scales for precise measurements. This allows for the identification of noise sources and system stability that would otherwise be obscured in standard variance analysis, as Allan variance can flatten or even decrease at specific intervals, revealing optimal time scales for precise measurements[151–153].

The Allan variance is a time-domain measure that represents half of the ensemble-averaged variance of the differences between successive position measurements. Each measurement is itself a local average of the probe's position. The timescale τ refers to the duration over which each measurement is averaged. For non-overlapping data it is calculated as:

$$\sigma^2(\tau) = \frac{1}{2N}\sum_{j=0}^{N-1}\{\bar{x}[2j\tau,(2j+1)\tau] - \bar{x}[(2j+1)\tau,(2j+2)\tau]\}^2. \quad [19]$$

$\bar{x}[t_1, t_2]$ is the average position from t_1 to t_2, $N = \frac{t_f}{2\tau}$, t_f is the total experiment time, $\tau = \tau_s, 2\tau_s, 3\tau_s, \ldots, \frac{t_f}{10}$, and τ_s is generally the sampling time, *i.e.*, the smallest time increment of position measurements. The largest τ has to be a fraction of the total time because as τ increases, fewer data points contribute to the calculation, making the statistical confidence lower for larger values. In this "non-overlapping" method, each position measurement contributes only once to each value of $\sigma^2(\tau)$, which limits statistical accuracy especially for large times τ. This approach has few values contributing for large τ, meaning the statistics are poor. A more refined method involves using overlapping data, where all possible bins for a given τ are used. In this case, the Allan variance is calculated as:

$$\sigma^2(\tau) = \frac{1}{2N}\sum_{j=0}^{N-1}\{\bar{x}[j\tau_s, j\tau_s + \tau] - \bar{x}[j\tau_s + \tau, j\tau_s + 2\tau]\}^2, \quad [20]$$

where $N = \frac{t_f - 2\tau}{\tau_s}$. The use of overlapping Allan variance has been validated by Lansdorp and others[149,154].

In the context of bead position tracking, Allan deviation quantifies how position measurements vary over different time scales, enabling the identification of noise[152] and systematic errors such as long-term drift. It also allows for determining the optimal time frame to calculate the variance accurately for thermally induced bead fluctuations[151,153].

The expected shape of the Allan deviation curve for a tether bead should be similar to what was reported by Czerwinski et al.[151] for optically trapped beads, and is similar at low time scales to Lansdorp *et al.*[148] (MT) and Andersson *et al.*[153] (OT). The behavior of the plot can be divided into distinct regions:

- Initial rise (positive slope): This phase typically occurs at times shorter than the correlation time (τ_c) in the measurements. This can be interpreted as a diffusive

motion of the probe at short times[149,154]; if so, then Lansdorp and Saleh[149] show that at short τ the Allan variance $\sigma^2(\tau) \propto \tau$.

- First maximum: This occurs around a timescale at which the measurements start to be uncorrelated. It is usually quantified by the correlation time (τ_c).

- Decrease (negative slope): This indicates noise reduction with increasing measurement time, consistent with averaging out high-frequency noise such as rapid fluctuations from electronic sources or thermal motion[151,153]. During this phase, the system moves towards optimal measurement accuracy, as it approaches the minimum in the Allan plot. Lansdorp and Saleh[149] show that in this range, the Allan variance $\sigma^2(\tau) \propto \tau^{-1}$.

- Minimum in Allan deviation: At this point, there is a balance between a time long enough to allow parameters to be accurately determined, and a time short enough that drift does not play a significant role. Drift of the sample stage or gradual thermal changes can increase the Allan deviation beyond this minimum[148,151]. This region often corresponds to the optimal measurement time for the experiment where noise is least affected by drift or external factors[151,153].

- Final rise at longer timescales (positive slope): At longer timescales, the plot shows an upward trend, suggesting that low-frequency noise starts to dominate. Factors such as stage drift, thermal fluctuations of other parts of the system, and other environmental effects contribute to the noise, causing the Allan deviation to increase again. This behavior is consistent with the findings of Lesage and Audoin[152] and Andersson et al.[153] where slow changes in the system or setup (such as stage drift or piezo stage instability) led to increased noise.

Allan deviation plots could be useful for evaluating the fluctuations of tethered beads and whether the fluctuation behavior aligns with the expected patterns, helping to identify potential anomalies or inconsistencies in the data. Figure 4-7 (A and B) presents the Allan deviation plot for beads fixed to a sample chamber in experiments lasting 10 minutes. Figure 4-7 (A) resembles the shape previously described, although the experiments here were not performed with tethered particles. Not all stuck beads exhibit this trend, with some displaying different behaviors, which could indicate that different mechanisms are part of the attachment for individual beads. Because these different

attachment mechanisms that are not accounted in this analysis, it might not resemble the shape previously discussed and therefore it might not be the right way to analyze stuck beads.

Averaging of the deviation of multiple stuck (potentially fiduciary) beads in the same sample smooths out statistical noise and reveals important trends, as seen in Figure 4-7 (B). For instance, sample drift starts to influence the measurements after the minimum of the Allan plot (~3 seconds). As explained previously, that would be the higher limit of the ideal timeframe to measure the fluctuation of the beads, before long-time fluctuations become relevant.

It is worth noting that I did not observe any significant difference in the Allan deviation or in the standard deviation when looking at motion aligned with versus perpendicular to the magnetic field. I tested this by rotating the magnets 90° before each series of bead position measurements was recorded, as shown in Figure 4-6.

Another approach commonly used to analyze fluctuations of a system is the power spectral density (PSD). The PSD contains the same information as the Allan variance but present it in a different format, focusing on how the variations are distributed across various frequencies. I used the Welch method[155], a common technique for estimating the PSD. It works by dividing the signal into overlapping segments, applying a window function to each segment, computing the periodogram for each windowed segment, and then averaging the periodograms to produce a smooth PSD estimate.

For my analysis, I used the SciPy Python library and treated the position data as if they were uniformly spaced in time, with the time interval taken as the average of the recorded time differences. I divided the positions into segments such that each segment contained a fifth of the total data points, used 50% overlap between segments, and applied a Hann window function before averaging the periodograms to obtain the final PSD. The result shown in Figure 4-7 (C and D) indicates an increase in the PSD at low frequencies, which is related to long-time fluctuations such as drift. This alternative representation offers a distinct way of understanding the system's behavior, revealing features such as the dominant fluctuation frequencies and the system's bandwidth[156,157]. The different perspective provided by the PSD complements the time-domain insights

from the Allan variance, allowing for a more comprehensive analysis of the fluctuations[148,151]. By using both approaches, one can gain a deeper understanding of the sources of variability and the system's response characteristics across different timescales and frequency ranges.

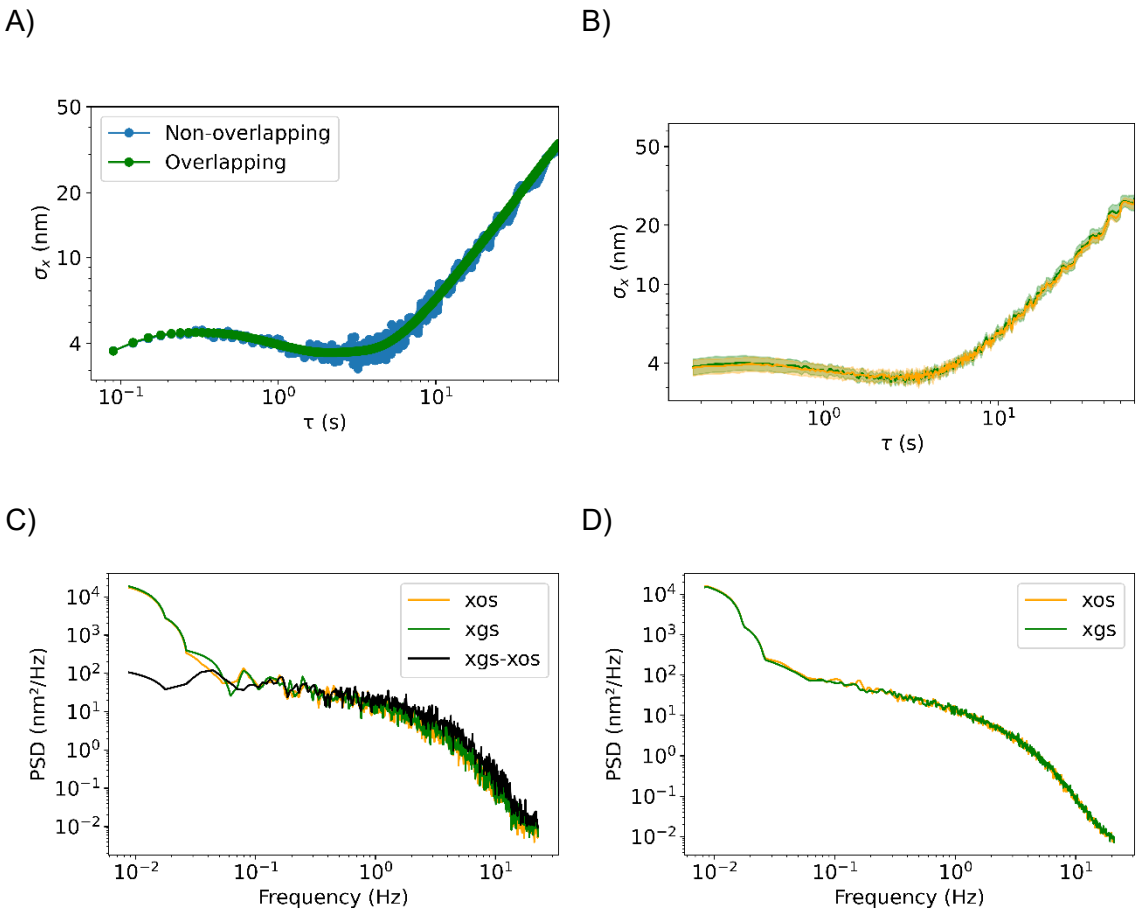

Figure 4-7 Allan deviation and PSD plot.
A) Allan deviation of a single stuck bead shows a similar shape as expected for a tethered bead calculated with the overlapping and non-overlapping method described in the main text. B) shows the average over 10 experiments conducted within the same sample chamber, with two beads tracked per measurement (green and orange, which are superimposed). The shaded regions indicate the standard deviation of the mean. The average sampling rate per measurement ranges from 41.0 to 48.4 Hz. (C and D) show PSD plots calculated using the Welch method. C) PSD for a single measurement showing two different beads (xos and xgs) and the difference between them (xos-xgs). D) Average PSD over 10 experiments conducted within the same sample chamber, with two beads tracked per measurement (green and orange, which are superimposed).

It is possible to calculate the shortest τ required to accurately measure thermally induced fluctuations using the correlation time τ_c. The simplest expression for τ_c comes

from an overdamped harmonic oscillator, which provides a reasonable approximation for the behavior of a tethered bead. The correlation time is defined as

$$\tau_c = \frac{\gamma}{\kappa}, \quad [21]$$

where γ is the viscous damping coefficient and κ is the restoring stiffness which in this case arises from the nonspecific adhesion of the beads to the glass. The stiffness could be calculated using the equipartition theorem (Equation [13]) and the measured variance. The viscous damping coefficient could be determined assuming Stokes' law for a bead with a diameter of 2.8 μm. Something to be mindful of when calculating the damping coefficient is that the tethered bead is close to the glass sample and is thus influenced by boundary conditions that increase γ well beyond Stokes' law[158,159]. Alternatively, the fitting method described in Lansdorp and Saleh[149] could be used to find the viscous damping coefficient and the restoring stiffness by using the first region of the Allan plot, which can be used to calculate the correlation time.

This analysis lays the foundation for future students to understand and characterize the fluctuations of fiduciary beads and of beads tethered to a surface via a polymer. In the latter cases, the behavior is expected to be similar but differing in terms of the timescales and fluctuation amplitudes, as the restoring stiffness of a tethered bead should be much lower than that of a bead stuck to the surface.

4.2. Bead height

In single-molecule force experiments on polymers using magnetic tweezers, it is necessary to precisely determine the extension of the polymer. This is achieved by measuring the height of a bead tethered by the polymer. The height is inferred from the out-of-focus diffraction pattern of the bead, which changes at different heights.

Various methods have been developed to accurately determine the bead's height based on its diffraction pattern. In the following section, I will describe some of these methods and the algorithms used in our instrument, along with the modifications I made to enhance their accuracy.

From a theoretical perspective, holographic imaging combined with fitting images to Lorenz-Mie scattering theory (LMST) has been employed to track colloidal spheres in three dimensions[160]. This approach also allows for the extraction of physical characteristics that define the hologram, such as the bead's radius and refractive index. However, in single-molecule biophysics, bead-tracking applications often use simpler, empirical methods to improve processing speed.

A commonly used and efficient method for bead tracking involves three distinct stages:

1. Find the center of the bead
2. Extract the radial profile
3. Compare the radial profile with a look-up-table (LUT)

The center of the bead is located by calculating either the center of mass or performing a one-dimensional (1D) or two-dimensional (2D) auto-correlation. Once the center has been identified, the radial intensity profile is typically generated by averaging different radial profiles of the same bead, which can sometimes be enhanced using computer-generated images[161]. To compare the image of the bead at unknown height with a pre-calibrated look-up table (LUT) of radial profiles, various methods can be used, such as using the squared difference[162,163] or cross-correlation[164]. The bead's height is then extracted by fitting the resulting curve, which relates the LUT profiles to the bead at an unknown height, and interpolating. This method has a balance between accuracy — achieving a resolution of up to 1 nm when optimized[162] — and speed, making it popular in applications where quick processing is needed.

Other methods have been used effectively, such as those described in Brouwer et al[161] and [163]. In these approaches, translations in the z direction are captured into a single parameter, the phase, which is shown to be proportional to the height. Using this method, an accuracy of 2.4 nm can be achieved at 30 Hz imaging or 1 nm at 5 Hz[161].

Improvements in tracking the height of beads can be made in several ways. A typical improvement involves optimizing the processing pipeline to increase the frequency at which bead images can be processed[150,162]. Modifications to the radial profile, such as re-scaling and truncating it, can also enhance accuracy[165]. Additionally, reducing the bias induced by pixelation can be achieved by interpolating the image on a

circular grid[164], achieving a resolution up to 0.2 nm. Enhancing the illumination of the sample is another effective approach, for example, by using a superluminescent diode [148] or a laser instead of a regular LED[166]. (It is important to note that using a laser introduces the issue of coherence, leading to variations in illumination at different distances due to interference from stray optical paths.) Using these methods, a resolution in the z-position of 0.014 nm can be achieved for an integration time of 4 seconds for a surface-attached bead and 0.17 nm for an integration time of 1 second for a tethered dsDNA [166]. Using a high-magnification objective lens can further increase resolution, achieving relative position changes of fixed beads with a precision of 1 Å at kHz rates and down to 0.1 Å at 10 Hz rates [150]. However, this approach has the drawback of reduced multiplexing capabilities. We would like to be able to capture and localize multiple beads simultaneously in our field of view and thus are working with images that strike a compromise between resolution and statistical power.

Figure 4-8 shows how the diffraction pattern of a bead changes with its distance from the objective lens, typically used for determining bead height in MT experiments. To visually represent how the bead pattern changes at different distances from the objective lens, Figure F-2 shows the radial profile of a bead at various heights after the processing in reciprocal space. My goal is to achieve nanometer-level precision in measuring the height, allowing me to detect changes in polymer extension within this range.

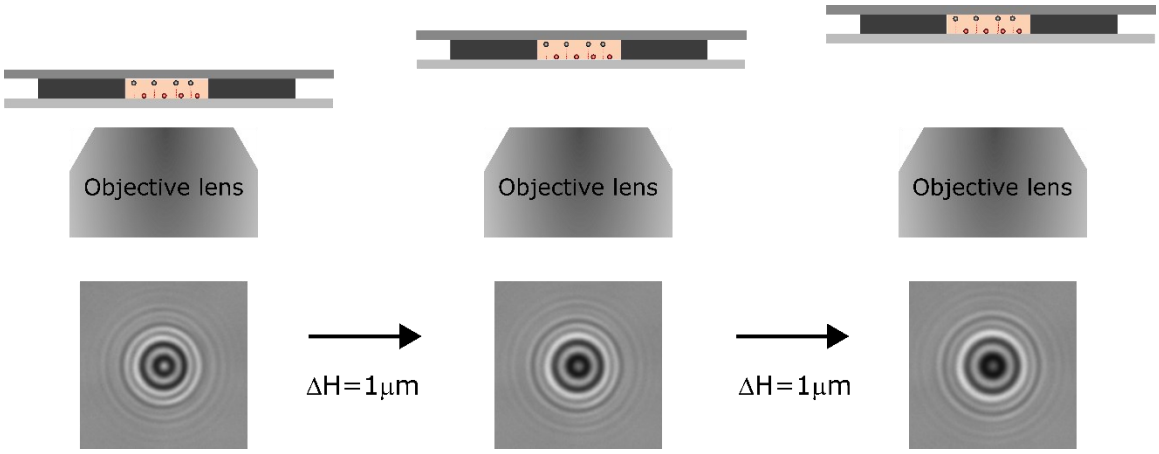

Figure 4-8 Bead diffraction at different heights.
This image shows how a bead's diffraction pattern changes when the piezo stage is raised in steps of Δ*H*=1 μm.

4.2.1. RMS algorithm

The algorithm I initially used to measure the height of the beads is an adaptation from one developed by Michael Poirier's group at The Ohio State University[136,137] (`Magnetic Tweezers for Instrument final RMS and record.vi`, Figure G-1). To use this algorithm, a calibration curve must be created. First, the region of interest (ROI) containing the bead to be analyzed must be selected, as shown in Figure 4-2. Two parameters are required to establish the calibration: the height of a high-precision piezo stage (*H*) and the intensity of each pixel in each ROI.

The piezo stage holding the sample chamber is moved in known steps away from the objective lens. At each piezo step height (H), bead images are captured (in my set-up, 25 images at each height, recorded at approximately 220 frames per second (fps)) and are processed to extract a characteristic reference value (here, the root mean square (RMS)) for calibration purposes. In the Poirier lab's implementation of image processing, the diffraction pattern of each bead is initially transformed into reciprocal space using a Fast Fourier Transform (FFT). The process in the reciprocal space includes a low and high bandpass filter, which eliminates the unwanted high and low frequencies, and an attenuation that adjusts the intensity of the bead image in reciprocal space. The images are subsequently transformed back using an inverse Fast Fourier Transform (FFT^{-1}), and the format of the image is adjusted to use the real part of that image for the next steps. The detailed process is outlined in Figure F-3.

From each of the 25 transformed images recorded at each piezo height *H*, the root mean square $RMS_H = \sqrt{\sum_{i,j}\left(I_{ij}^{H}\right)^2}$ of the pixel intensities in the ROI is determined. The average of these 25 values is used as the reference value for that piezo height. This series of RMS_H values then form the calibration curve for determining height of an unknown bead (Figure 4-9).

In practice, the starting point of the calibration curve should be decided by the region where the relationship between piezo height and RMS is monotonic, as indicated in the shaded region of Figure 4-9 (A). This can be identified through an initial calibration curve with a wide piezo stage height range, typically between 20 μm and 30 μm, starting at the focal plane of the beads. The size of the steps could be as large as 1 μm because

the goal is merely to identify the monotonic region of the curve. After the monotonic region is identified, in this case (Figure 4-9 (A)) approximately 9 µm above the focal plane and spanning about 10 µm, a final calibration in that region has to be performed by choosing a range suited for the specific experiments that will be conducted.

For my experiments, involving DNA of either ~340 nm or ~680 nm in length, a final calibration over a 1 µm range with 200 nm steps should be sufficient to detect changes in polymer extension. However, I prefer to perform the calibration over a larger region (e.g., 3 µm) and with shorter steps (e.g., 100 nm) since it does not require much additional time or computational resources (Figure 4-9 (B)). If a longer polymer is used, a final calibration curve with a wider piezo height range should be created.

The final calibration curve on the monotonic relation region is then fit by a polynomial function, which enables the determination of the bead's height by reading the RMS values (Figure 4-9 (B)). The order of the polynomial fit could be changed to adjust better to different calibration curves.

Before starting each experiment, it is essential to create a calibration curve for each bead that will be tracked. This calibration process must be repeated whenever a new set of beads is used or if the microscope has drifted out of the previously established calibration range.

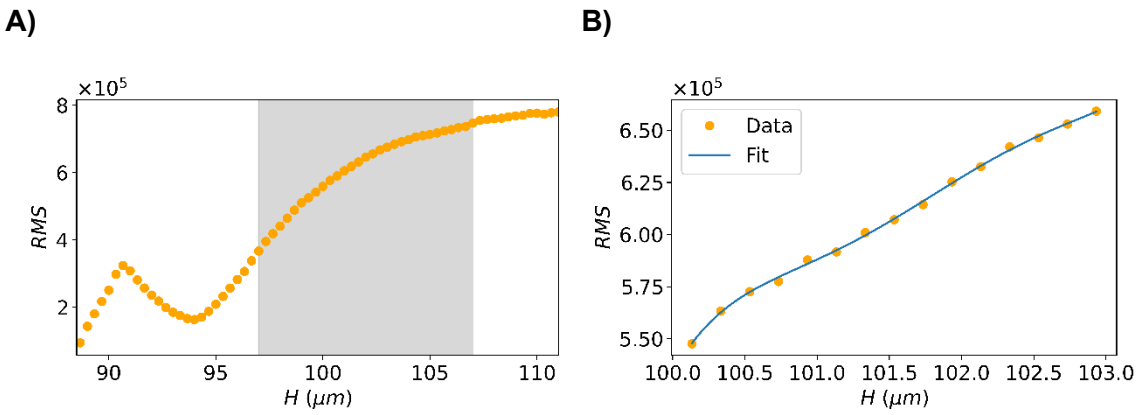

Figure 4-9 RMS algorithm bead height calibration.
A) RMS preliminary calibration curve showing the relationship between the height of the piezo stage *H* and the RMS for a bead. The shaded area represents a range where the relation is monotonic and the RMS algorithm can be used. The first point in the x-axis corresponds to the focal plane of the beads (~ 88.3 µm) and the stage was moved 3 steps per micron. B) RMS final calibration curve showing data and a 5th-degree polynomial fit. Here, the stage was moved in 200

nm steps. The piezo stage of our piezo stage has a range of movement of 200 μm and a minimum step size of 2 nm.

I discovered a problem with using this algorithm in our system: the change in illumination intensity with magnet height (*z* in Chapter 2) that results from our use of transillumination with light from an LED passing through a narrow aperture between the magnets (Figure 2-3). This contrasts with the epi-illumination used by the Poirier group, in which illumination light is provided through the objective lens and thus its intensity does not change with magnet height. I found that in our set-up, the intensity of the illumination decreases as the magnets are moved away from the sample chamber (Figure 4-10, Figure 4-11 (A)), which leads to a change in the RMS of the bead (Figure 4-11 (B)). The consequence is that any movement of the magnets could cause an inferred change in the bead's detected height, even for a stuck reference 'fiducial' particle.

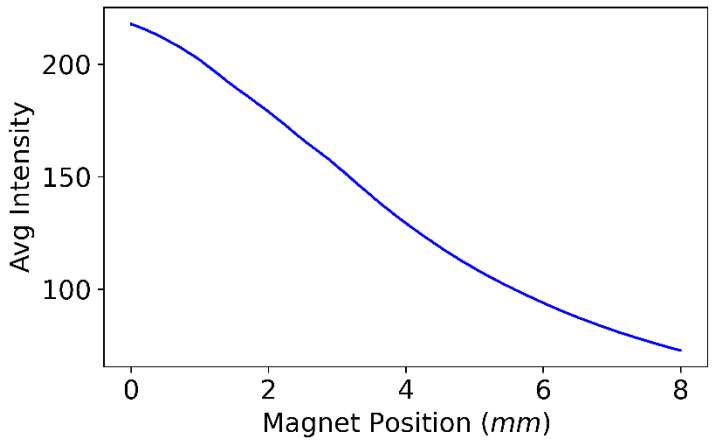

Figure 4-10 Intensity of the full field of view at different magnet heights.
The Intensity was averaged over the field of view for each image as the magnets were withdrawn over an 8 mm distance. The zero magnet position is the closest distance between the magnet and the sample that the system currently allows.

This issue becomes evident when applying a calibration curve to interpret changes in RMS as changes in bead height. After altering the magnet height by just a few millimeters, the calibration curve's range is exceeded. Specifically, with a calibration curve that covers a large range (e.g., 10 μm as shown within the shaded regions of Figure 4-9 and Figure 4-11), the RMS values fall out of this range after adjusting the magnet height by less than 4 mm. Consequently, this leads to inferred bead heights that

differ by more than 10 µm at different magnet heights, even though the bead is at the same location with respect to the objective lens throughout.

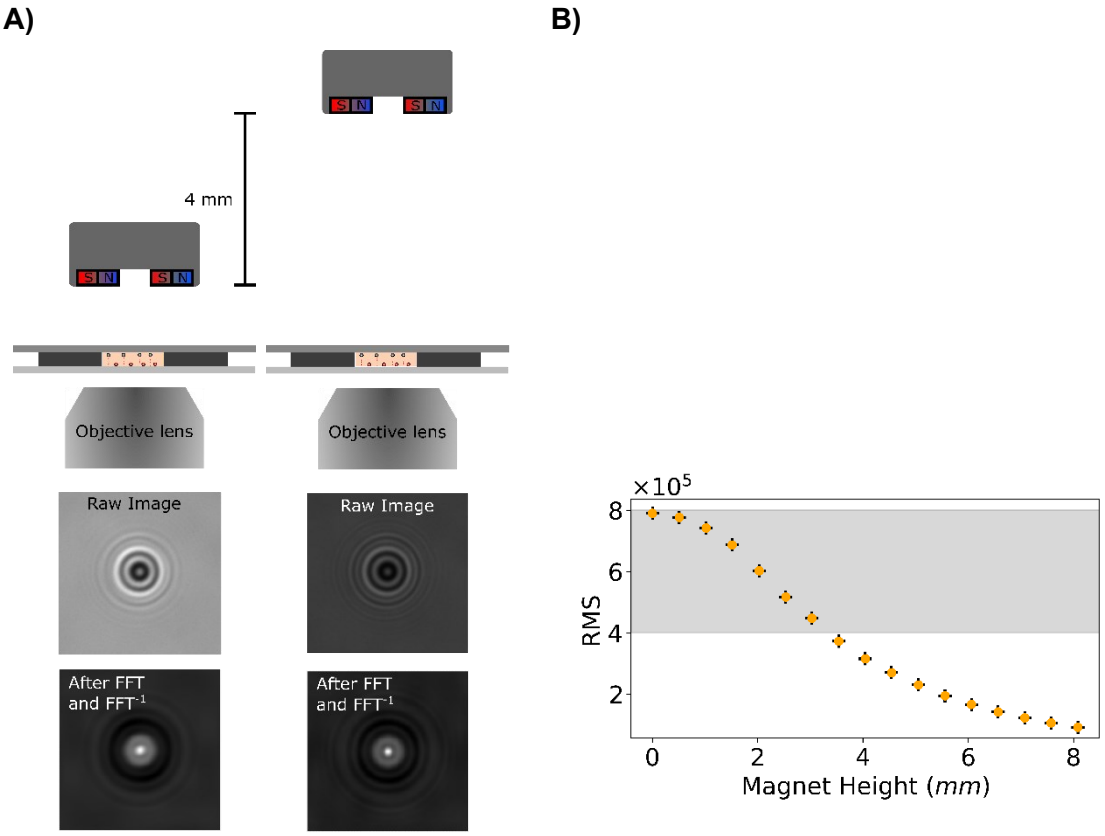

Figure 4-11 Bead images and RMS at different magnet heights.
A) The raw image and the image after processing in reciprocal space are shown for one bead at 0 and 4 mm magnet heights respectively. The schematic is not to scale. B) shows how the RMS changes for a fixed bead when the magnets are withdrawn from the sample. The range where the magnets are moved (8 mm) is guided by the range where the magnetic field does not change direction, as discussed in Chapter 2. The magnet height was changed in discrete steps of 1 mm, zero is the closest distance currently achievable between the magnets and the sample, and the error bars indicate the standard deviation for both the RMS and the magnet height.

During experiments, this is a problem because adjusting the magnet height to change the force exerted on a bead should not influence the measured height of fiduciary beads stuck to the sample. Additionally, for tethered beads, the height should vary only due to the extension of the polymer, not because of changes in illumination. Ideally, the change in measured bead height at different magnet heights should be on the order of nanometers or less.

I tried different approaches to correct this problem. First, I checked if the RMS of the background also changed with magnet height; Figure 4-12 shows that it does. So, the Fourier transform does not correct for changes in the background.

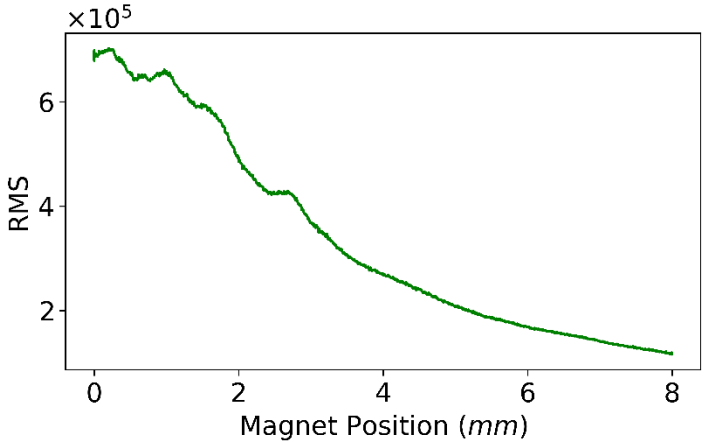

Figure 4-12 RMS of background.
RMS of the background in a square ROI of 250 pixels (~ 27.3 μm) in length, for magnet position changed continuously in an 8 mm range from the closest distance to the sample (where magnet position = 0).

The diffraction profile of stuck beads should not depend on the magnet height, and also experimentally did not appear to change much when the magnet's height was changed (Figure 4-13). Only the intensity decreased as the magnets were pulled away, as shown in Figure 4-13 (A and B). However, the profile after processing the image in reciprocal space did seem to change significantly as shown in Figure 4-13 (C).

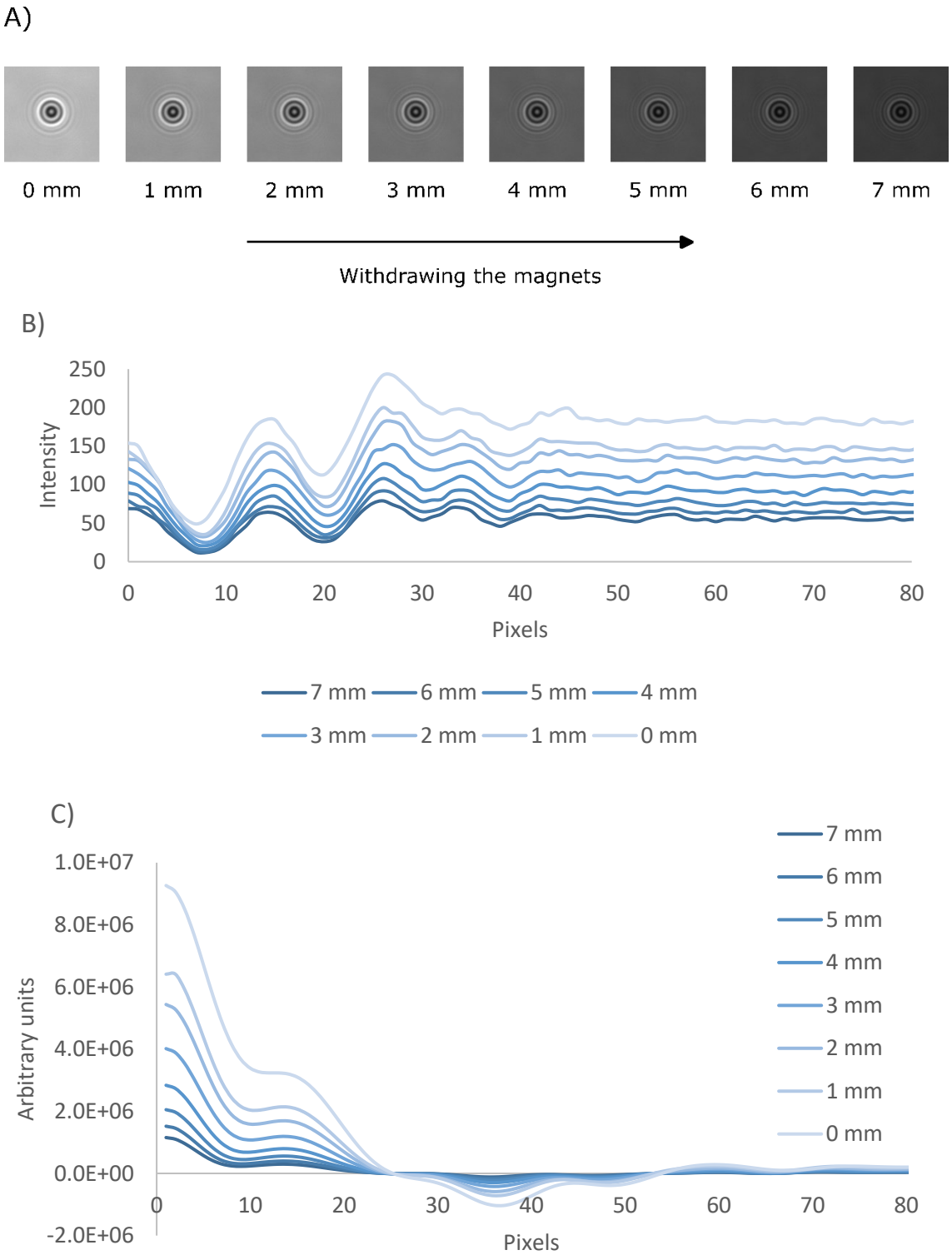

Figure 4-13 Bead images and profiles at different magnet heights.
A) Images of the full ROI as the magnets are withdrawn. B) Radial profile of the diffraction pattern of the beads at different magnet heights. The radial profile was extracted by manually selecting the bead's center and plotting the line of pixels to the right of that center from the raw images. The x-axis represents pixel distance, and the y-axis represents pixel intensity along this coordinate. C) Radial profile of the bead diffraction pattern after processing in reciprocal space.

The bead's center was determined using the algorithm described in Section 4.1.1. The x-axis represents distance in pixels, and the y-axis represents the intensity along this coordinate, taken from the real part of the image after transforming back to real space using the inverse Fourier transform.

Because of the small changes in the diffraction pattern features, mainly changes in the intensity but not much in the shape, I tried rescaling the intensity of the raw image in the ROI from 0 to 100, using:

$$\mathrm{I_{scaled}} = \frac{\mathrm{I} - \mathrm{I_{min}}}{\mathrm{I_{max}} - \mathrm{I_{min}}} \cdot 100, \qquad [22]$$

with 100 being the highest intensity and 0 being the lowest, shown in Figure F-4.

This approach also did not work: the RMS still changed with the magnet height as shown in Figure 4-14 (A). Changing the magnet height by 8 mm resulted in a measured height difference (after applying the calibration curve) of approximately 1.5 µm *(*Figure 4-14 (B)). This is more than three times the length of the longest DNA I was planning to use (2 *kb*,~ 680 nm), indicating that the height precision is insufficient for the experiments planned with this instrument.

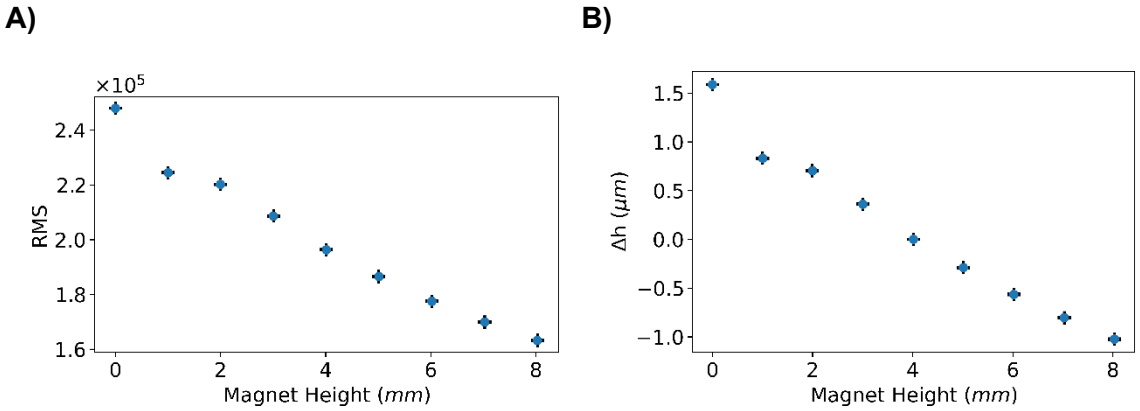

Figure 4-14 RMS and bead height for re-scaled bead diffraction pattern.
For this experiment, the magnet height was changed in discrete steps of 1 mm, and ROI intensity was rescaled from 0 to 100. The error bars indicate the standard deviation in both plots. A) shows the RMS for a bead at different magnet heights. B) shows the inferred bead height (*Δh*) at different magnet heights. *h*=0 is chosen as the height measured from the piezo stage at 4 mm magnet height, where the calibration curve was performed.

4.2.2. Illumination light path modifications

The RMS change at different magnet heights is partially caused by uncollimated illumination light. The original optical path designed by MadCity Labs (Figure 2-3) consists of one converging lens (f = 75 mm) positioned approximately 40 mm from the LED; the light is then reflected by a 45° mirror and finally passes through another converging lens (f = 150 mm) 155 mm away from the second lens. This configuration does not result in collimated light illuminating the sample.

One way to fix this problem is to collimate the illumination light. However, collimating the light from an LED is challenging because the light distribution is not homogeneous, and it is neither parallel nor a perfect point source. However, to improve the collimation, I start by considering the light from the LED as a point source.

If a calculation is done with the original optical path using the thin lens equation,

$$\frac{1}{f} = \frac{1}{d_o} + \frac{1}{d_i}, \qquad [23]$$

the excitation light will converge to a point at approximately 260 mm from the second lens. This distance is beyond the magnet holder, the sample, and the focal point of the objective lens. Such a configuration will create a decrease in the illumination intensity as the magnets are withdrawn from the sample. Figure 4-15 shows a simplified ray diagram of the original configuration.

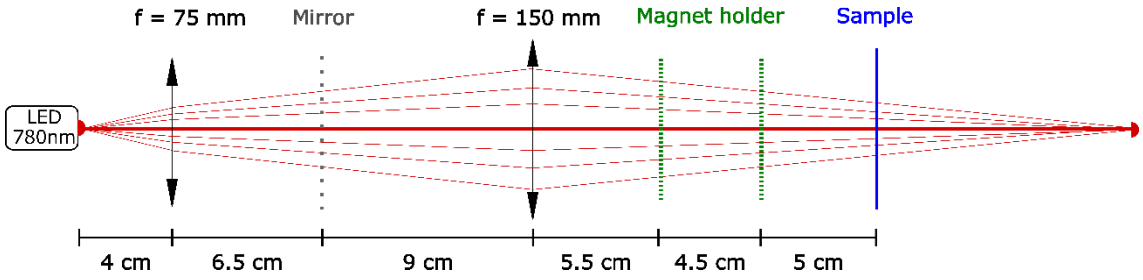

Figure 4-15 Original lightpath.
Simplified version of the original illumination path. Parts from left to right are: LED, convex lens (f = 75 mm), mirror (not acting as a mirror in this illustration), convex lens (f = 150 mm), the furthest and closest positions of the aperture in the magnet holder, and the sample.

A way to correct this problem is to have a different light path that provides more collimated excitation light. I used the lenses available in our laboratory to test this

correction. In the first and second attempts, I used the lenses from the original optical path, but one at a time, positioning each lens at a distance from the LED equal to its focal length. This setup would create perfectly collimated light for an ideal point light source and an ideal lens, as shown in Figure 4-16.

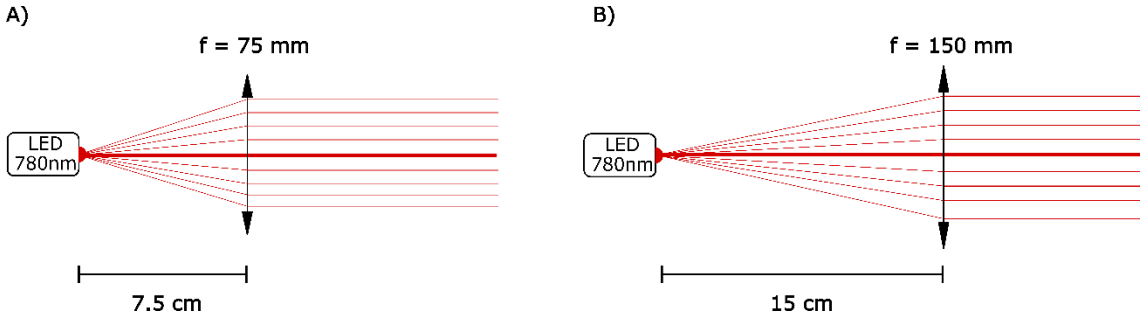

Figure 4-16 Illumination using one lens.
Modifications to the illumination by using one convex lens positioned at a distance from the LED equal to its focal length: A) 7.5 cm and B) 15 cm.

To study the effect of these different lens arrangements, I changed the magnets' height while tracking average intensities and RMS, and extracted bead height from the recorded images. The range over which I moved the magnets was guided by the relevant region of force at different magnet heights determined in Chapter 2, from the point of closest approach to where the magnet-exerted force goes to zero (at 7.1 mm).

Figure 4-17 shows a comparison of the average background intensity across the entire field of view, between the original arrangement and the one-lens configurations. The intensity difference at different magnet heights is significantly improved for the configurations where only one lens is used.

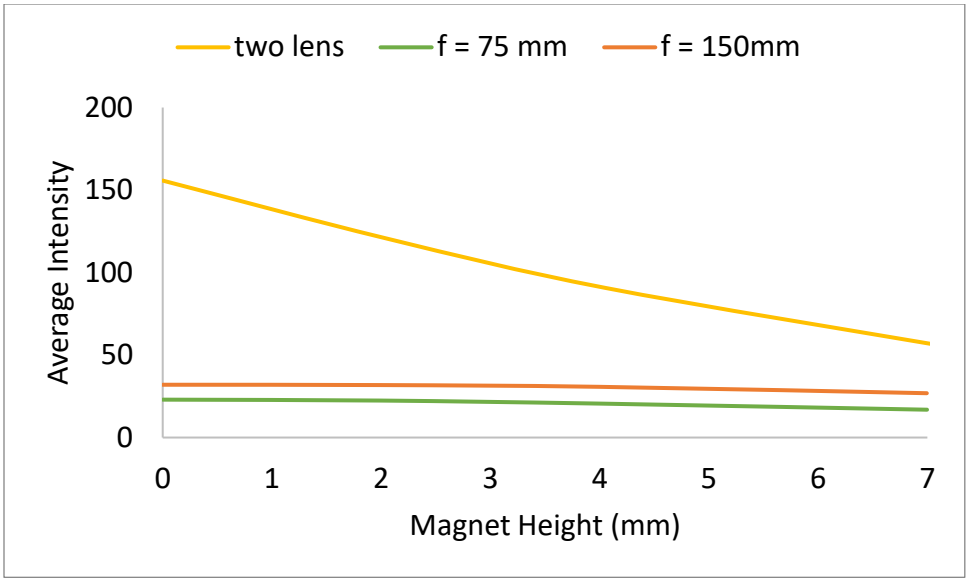

Figure 4-17 Average intensity for different illumination path configurations.
The average intensity of the whole field of view at different magnet heights for the original two-lens configuration compared to the partially collimated configurations using one lens (*f* = 75 mm or *f* = 150 mm).

However, while there are significant improvements over the original two-lens design, the RMS and the measured bead height still changes with magnet height when just one lens is used (Figure F-5).

Inspired by the partial success of this approach, I aimed to further improve the collimation using two converging lenses and an iris. Here, the aperture of the iris can be used to eliminate some of the extra modes in the light profile, thereby creating a better point source of light. For this configuration, I used a *f* = 25 mm converging lens, a *f* = 75 mm converging lens, and an iris diaphragm. The first lens (*f* = 25 mm) was positioned at a distance equal to twice its focal length from the LED, creating a focal point of light just before the mirror where I placed the iris diaphragm. The second lens was positioned at a distance equal to its focal length from the iris to complete the collimation arrangement. This setup is shown in Figure 4-18, ignoring the mirror.

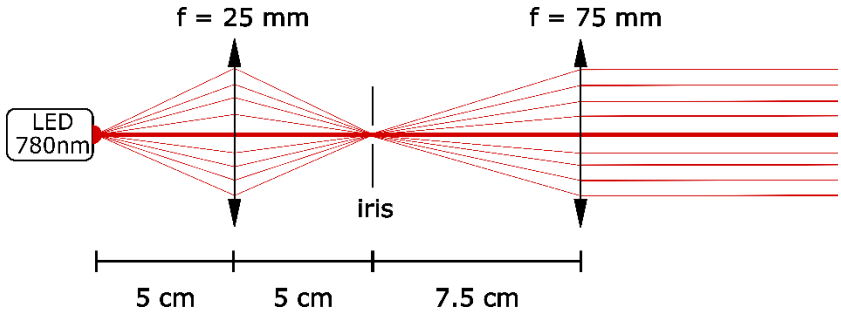

Figure 4-18 Revised two-lens plus iris illumination path.
Illumination path using two convex lenses (*f* = 25 mm and *f* = 75 mm) and an iris diaphragm to better collimate the illumination light.

To assess the improvement resulting from this light path, I compared the original configuration to the new configuration when the iris is completely open and when the iris is open to only 2 mm. The collimation should be better when the iris is closed, however, this could also cause insufficient illumination to track the beads. I found the background intensity to vary far less as magnet height changes for the new configuration (Figure 4-19). The percentage of variation in the average intensity for the full magnetic height range is 68.6% for the original configuration, 30.0% for the new configuration with the iris open, and 2.96% for the new configuration with the iris at 2 mm wide.

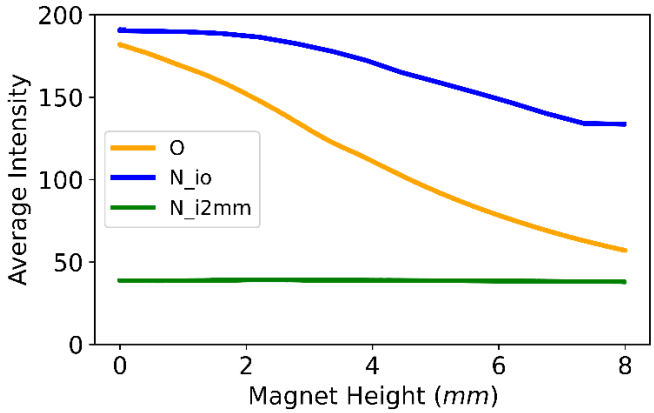

Figure 4-19 Average Intensity of original and final illumination path configurations.
Average intensity in the whole field of view for the original illumination (O) and the new two-lens configuration with the iris completely open (N_io) and the iris closed to a 2 mm aperture (N_i2mm). The magnets were continuously moved at 0.5 *μm/s.*

I also compared bead images at different magnet heights for the original light path and for the new light path when the iris is completely open and when the iris is 2 mm wide. For both iris settings, the change in RMS is significantly less than with the

original configuration, as shown in Figure 4-20, and the illumination is sufficient to track the beads.

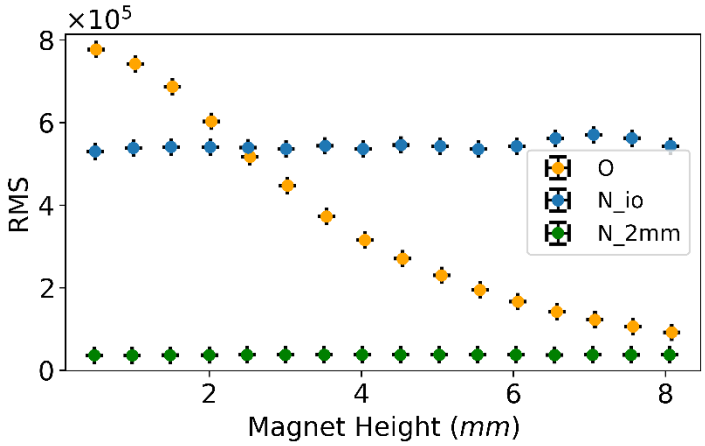

Figure 4-20 RMS of original and revised two-lens light paths.
For this experiment, the magnet height was changed in steps of 1 mm while tracking the RMS. These measurements were made for the original configuration (O) and the new configuration with the iris open (N_io) and the iris at 2 mm (N_2mm).

The new illumination arrangement also caused the radial profile at different magnet heights to become essentially invariant with magnet height, both for the raw images and for the images after the Fourier processing (Figure 4-21). This is an enormous improvement from the original illumination design (Figure 4-13).

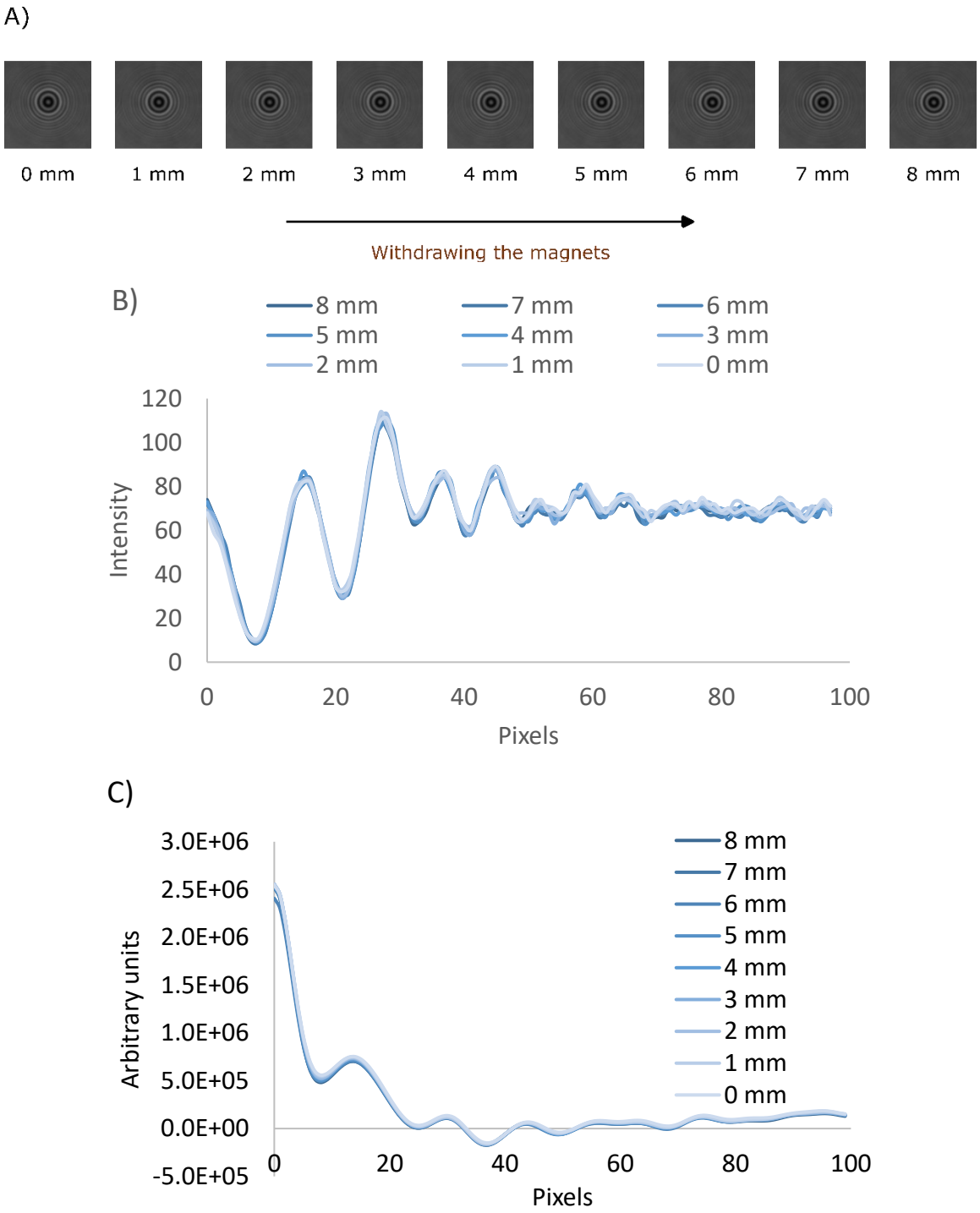

Figure 4-21 Bead diffraction pattern using the final two-lens illumination path. A) Images of the full ROI as the magnets are withdrawn. B) Radial profile of the diffraction pattern of the beads at different magnet heights. The radial profile was extracted by manually selecting the bead's center and plotting the line of pixels to the right of that center from the raw images. The x-axis represents pixel distance, and the y-axis represents pixel intensity along this coordinate. C) Radial profile of the bead diffraction pattern after processing in reciprocal space. The bead's center was determined using the algorithm described in Section 4.1.1. The x-axis represents the distance in pixels, and the y-axis represents the intensity along this coordinate,

taken from the real part of the image after transforming back to real space using the inverse Fourier transform.

However, when using the RMS algorithm to determine the height of beads, I found that the extracted bead height still changed for this new light path. With the iris open, the measured height change over the full range of magnet motion is 290 nm; with the iris 2 mm wide, the inferred height change is 190 nm (Figure 4-22). Previously, the change in the measured height using the original illumination was greater than the range of the calibration curve, *i.e.* > 10 μm. Even though there was an improvement of more than 2 orders of magnitude, the inferred bead height change is still too great for our target of nanometer-scale resolution. I also tried re-scaling the raw images as in the previous section, however, the results were quite similar, and the largest change in the measure bead height for the 8 mm magnet height range was 216 nm as shown in Figure F-6. This suggests that rescaling of the raw images does not improve the precision of the measurement.

Simply changing the excitation light path is not enough to obtain accurate measurements when changing the magnet height. As a result, I explored using a different algorithm that could decrease the variation in extracted bead height at different magnet heights.

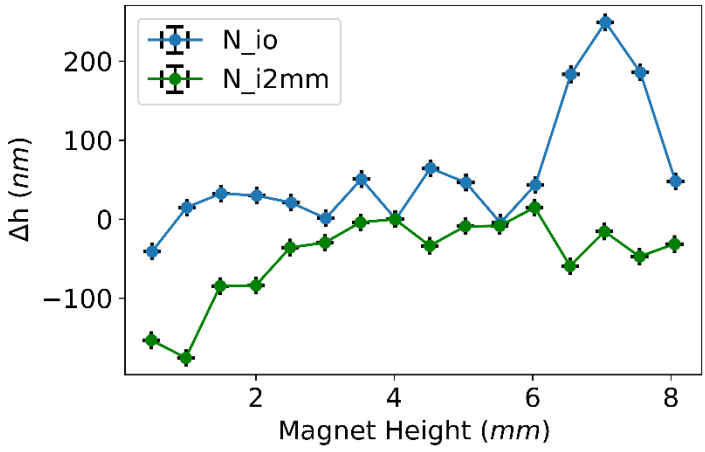

Figure 4-22 Measured changes in bead height with the final illumination setup.
Measured change in bead height (Δh) at different magnet heights with the new light configuration and using the RMS algorithm. The two curves belong to the same bead using the iris completely open (N_io) and the iris 2mm wide (N_i2mm). The magnet height was changed in steps of 1 mm.

4.2.3. Implementation of a new correlation-based algorithm

The algorithm that I developed (Figure 4-23) to determine bead height uses the radial profiles of the beads and correlates the intensity profile of a measured diffraction pattern of a bead at an "unknown" height with a calibration set measured for the same bead at known heights. I decided to use this approach because the features in the radial intensity profile of a bead at different magnet heights look very similar (Figure 4-13 (B) and Figure 4-21).

First, for every bead image, I used the same image processing in reciprocal space as described in Section 4.2.1; the details of this can be found in Appendix F (Figure F-3). Next, the algorithm locates the center of the bead's diffraction pattern using the same approach described in Section 4.1.1, but instead of performing a cross-correlation with temporally shifted images, an autocorrelation is applied. Then, a radial profile of each bead is extracted by taking the intensity along a line of pixels to the right of the center in the ROI (Figure 4-24 (A)). This radial profile can then be used either to create an entry in a calibration standard, with known bead heights read from the piezo stage, or to determine the height of a bead by correlating it with the previously calibrated set of images.

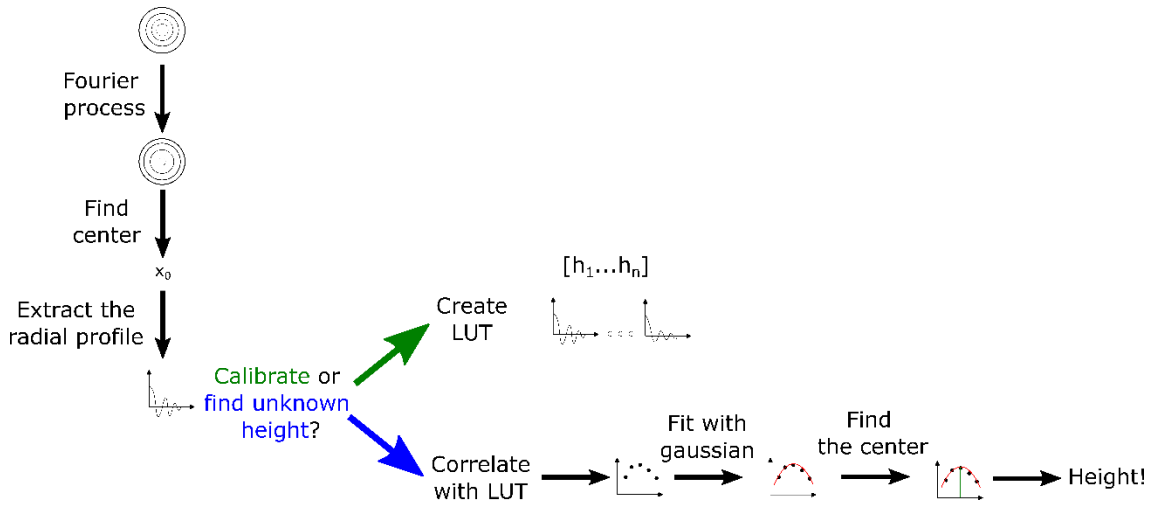

Figure 4-23 Correlation algorithm to measure bead height.
Pipeline from the raw image of the diffraction pattern in the ROI to the measure of the height. The first part of this algorithm (i.e. the process in the reciprocal space and finding the center of the bead) was adapted from LabVIEW code developed in Michael Poirier's laboratory[136,137]. The rest of it was developed by me and implemented in LabVIEW.

For calibration, a look-up table (LUT) is created by moving the height of the sample chamber via a piezo stage, in 100 nm increments. After waiting 10 ms at each step to ensure that the piezo stage equilibrates at the desired height, an image of the bead is recorded along with the corresponding piezo stage height. The radial profile of that image is extracted by finding the center using the approach described in the previous paragraph, and taking the intensities to the right of that center.

The height of a bead is measured by correlating its radial profile (Figure 4-24 (A)) with those in the previously created LUT (Figure 4-24 (B)). A few points around the maximum correlation index are then fitted to a Gaussian (Figure 4-24 (C)), and the center of this Gaussian provides the bead's height. I found that using fewer than 5 points or more than 11 points for the Gaussian fit can sometimes result in incorrect heights, so I recommend using a number of points within that range.

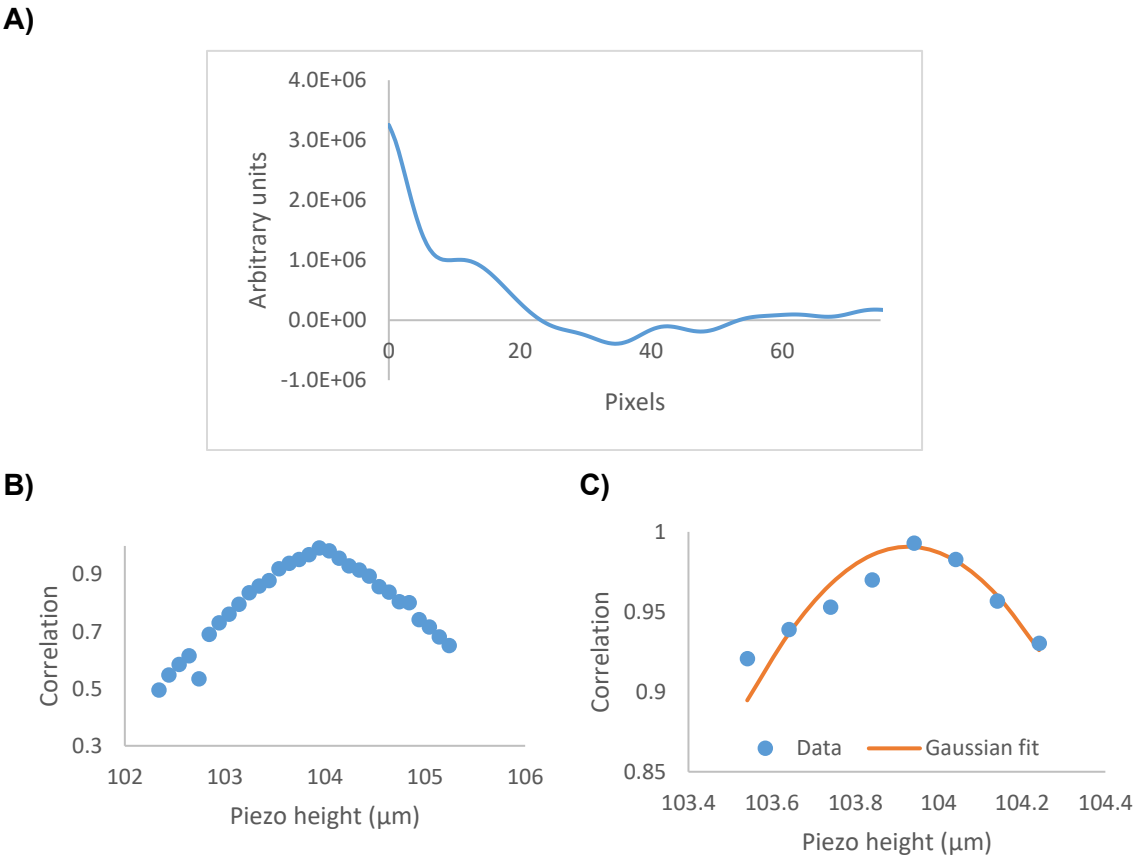

Figure 4-24 Bead height analyzed with the new correlation algorithm.
This experiment is done with the original illumination set up. A) Radial profile of a bead with an unknown height after processing in Fourier space. The x-axis is the pixel distance and the y-axis is the intensity (from the real part of the image after being transformed back to real space by using the inverse Fourier transform). B) Correlation between the radial profile of the bead with

unknown height and the LUT radial profiles recorded at different piezo stage heights. C) Eight points around the maximum correlation index in (B) fitted with a Gaussian.

The results in Figure 4-25 shows that using the *original* illumination and a fiduciary stuck bead, the correlation index varies significantly less (the maximum variation is 7.6%) at different magnet heights in comparison with the RMS value that varies by two orders of magnitude. This suggests that it would be more effective to use a correlation-based algorithm rather than an RMS-based algorithm to read the bead heights in our experimental setup.

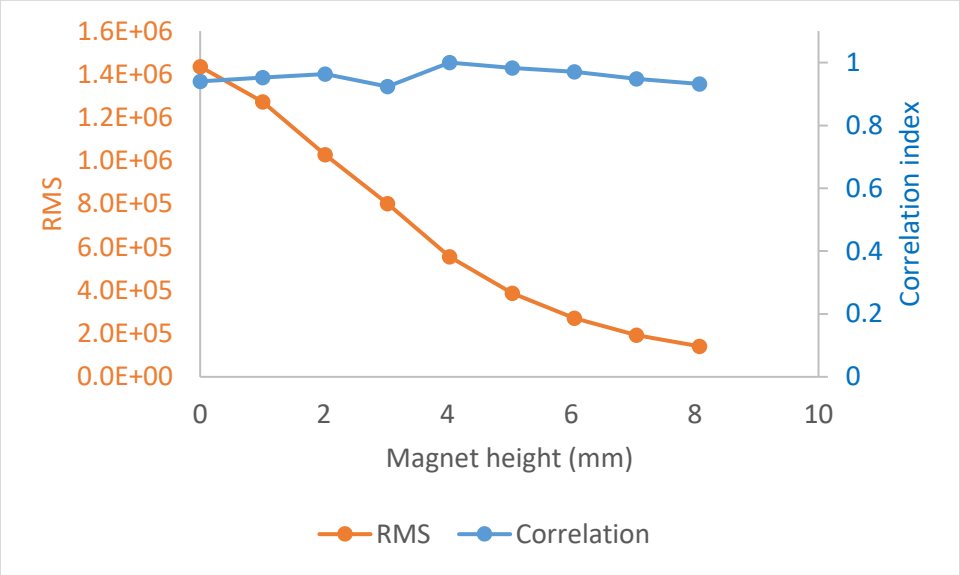

Figure 4-25 RMS and correlation index at different magnet heights.
Images of a bead at different magnet heights of 1 mm step were analyzed. The orange curve shows the change in the RMS value for those sets of images, while the blue curve shows the change in the correlation index with a reference bead LUT at magnet height = 4 mm. For all the analysis the images were processed in the reciprocal space as previously described.

The next step is to evaluate how much the measured bead height changes with magnet height using the correlation algorithm, still with the original illumination scheme. I discovered that there is still a significant variation in the measured height. Figure 4-26 shows six examples from different samples where the apparent height of the bead changes with the magnet position, with ranges between 19 nm and 261 nm. Although this is a substantial improvement compared to the RMS algorithm, where the variation in measured height exceeded the calibration range (>10 μm), the range remains too large for the type of experiments we aim to conduct in the lab. The shorter DNA tether that I used is approximately 340 nm long and the variation caused by changing the magnet

height is on the same order of magnitude. Ideally, the measured height change should be less than a few nanometers for the relevant range of magnet heights.

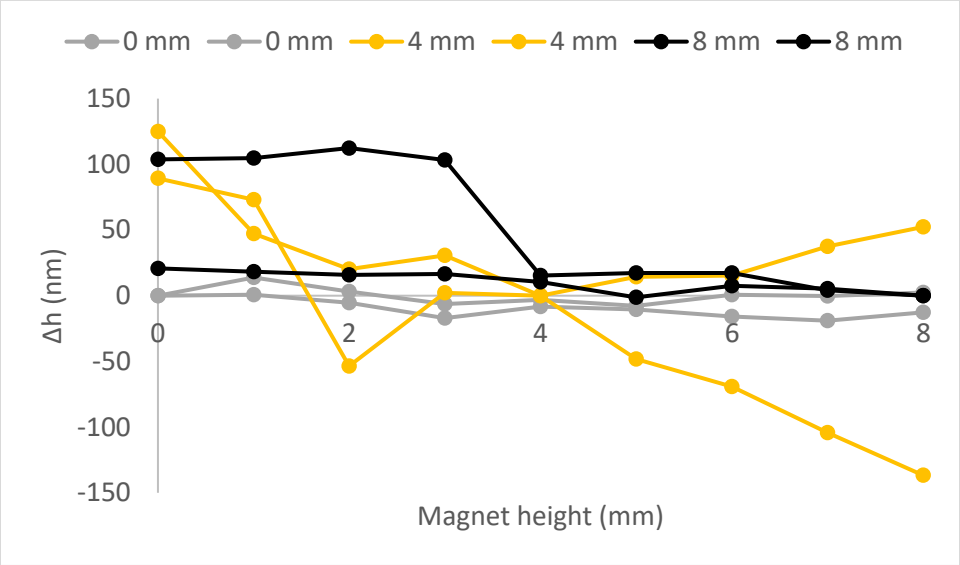

Figure 4-26 Bead heights at different magnet heights with correlation algorithm. Inferred change in bead height (Δh) at different magnet heights for six different fiduciary beads. Bead height changes are referenced with respect to the position at which the respective LUT was created (two with magnets as close as possible to the sample (gray), two at 4 mm away from the sample (yellow), and two at 8 mm away from the sample(black)). Lines are to guide the eye.

4.2.4. Modified illumination and correlation algorithm.

Because neither the modification to the illumination nor the correlation algorithm by themselves reached the desired precision, I combined and tested the performance of the new iris-based two-lens optical arrangement with the newly implemented correlation algorithm. The approach of combining the new algorithm with the modified illumination yields better results, as described in this section.

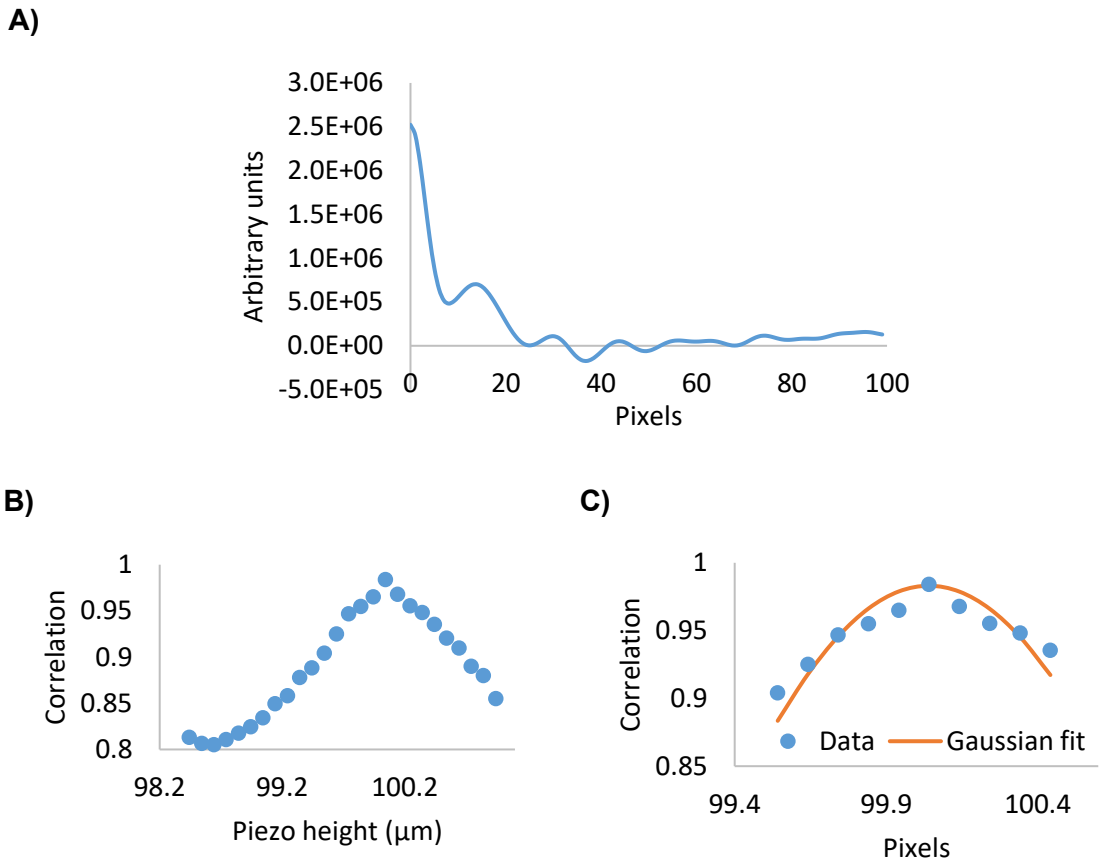

Figure 4-27 Bead height analyzed with the improved method.
This experiment was performed with the partially collimated illumination two-lens set-up with the iris 2 mm open and the correlation algorithm. A) Radial profile of a bead at an unknown height after processing in Fourier space. The y-axis is the signal in the real part of the image after being transformed back to real space with an inverse Fourier transform. B) Correlation between the radial profile of the bead at unknown height and the LUT radial profiles. C) Ten points around the maximum correlation index in (B) fitted with a Gaussian.

Figure 4-27 shows similar results – for the new illumination – as in Figure 4-24 in the original illumination. The radial profile shows clearer variations with the new illumination, which I expect to lead to a better precision when using the correlation algorithm to extract an unknown bead height. The variations in the measured height at different magnet heights are significantly smaller than with the original illumination or with the RMS algorithm. Variations in inferred height for stuck bead are less than 10 nm, when combining the new algorithm with the new optical alignment. Figure 4-28 shows examples of six different bead heights tracked, with the largest variation of 9.6 nm and the best precision being 0.0014 nm, below the resolution of the piezo stage (0.2 nm).

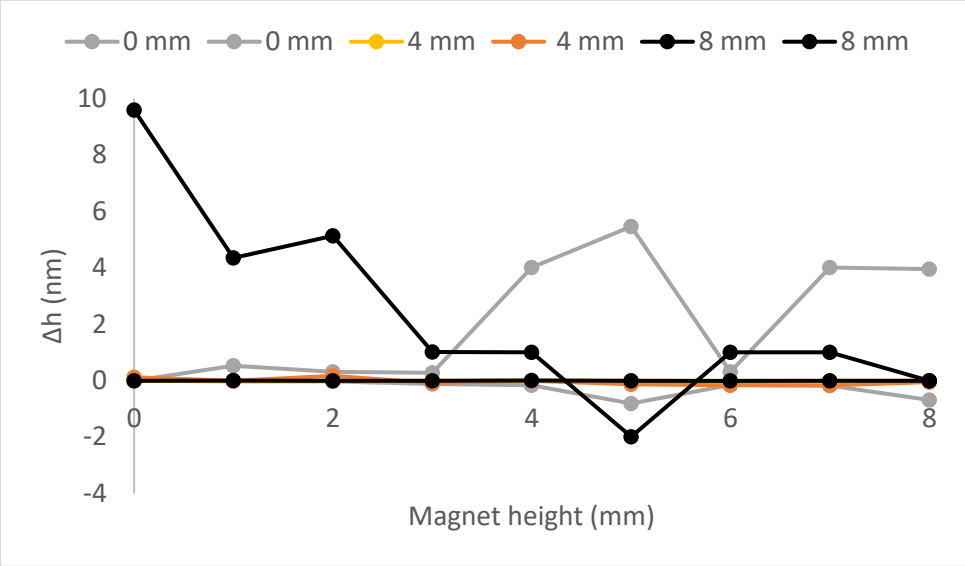

Figure 4-28 Improved performance of inferred bead height.
Inferred change in bead height (*Δh*) at different magnet heights for six different fiduciary beads using the new illumination and the new correlation algorithm. Bead height changes are referenced with respect to the position at which the respective LUT was created (two with magnets as close as possible to the sample (gray), two at 4 mm away from the sample (yellow and orange), and two at 8 mm away from the sample(black). Lines are to guide the eye. The standard deviation between all measurements is 1.8 nm.

Finally, I tested whether the Fourier processing was necessary, or if I could simply use the raw bead images. I found that the processing significantly improved the height resolution: for the raw images, the correlation algorithm gave variations in bead height on the order of ±40 nm (Figure 4-29), compared with the subnanometer change of the same bead using the filtered images (Figure 4-28 orange line).

The best approach to measuring the bead height and avoiding the changes produced by the height of the magnets is to use the partially collimated two-lens and iris illumination in combination with the correlation algorithm described in the precious section.

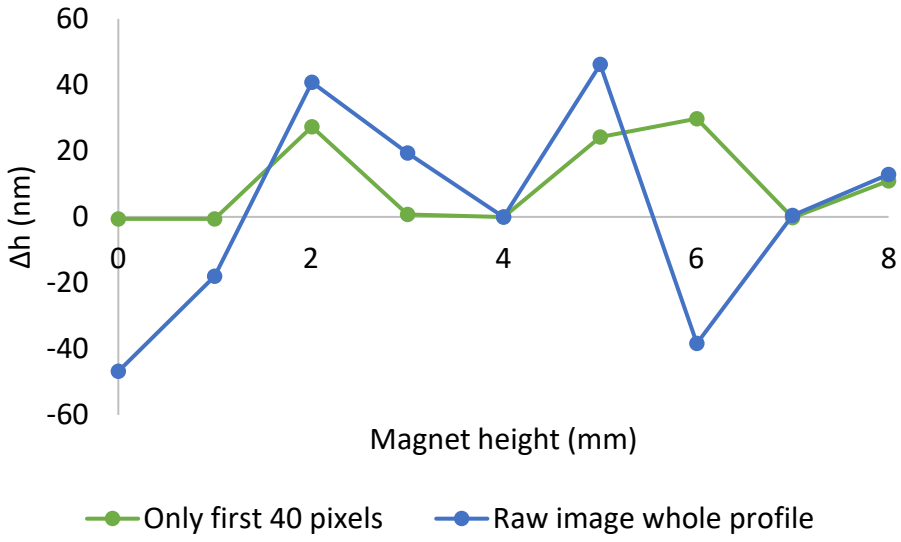

Figure 4-29 Change in bead height inferred from raw images.
For this experiment, I used the raw images (not processed in Fourier space) in the correlation algorithm, with data recorded using the new partially collimated illumination with the iris open 2 mm. The magnet was moved in 1 mm steps and one image per magnet height was collected (same bead images used in Figure 4-28). h = 0 mm is where the calibration images were taken, in this case, 4 mm away from the closest distance that the magnets could be from the sample. For the orange curve, the whole profile was used (100 pixels), and for the blue only the first 40 pixels in the radial profile of the bead. Although most of the information is contained in the first 40 pixels of the radial profile (e.g. Figure 4-27A), there is still significant variation in inferred bead height when using this information in the correlation.

4.2.5. Index of refraction correction

Different systematic errors can affect height measurements in MT setups; a typical one is caused by refractive index mismatches. In our instrument, we use an oil-immersion objective lens, which introduces image distortion because the refractive index of the immersion oil (n_o = 1.515) is different from that of the water or buffer in the sample chamber ($n_W \approx$ 1.333).

During calibration and for fiduciary beads, the objective lens is moved by known distances in the oil while the bead remains stationary, and therefore any height change occurs in the oil. However, during the measurement of a polymer-tethered bead, its height changes in water while the piezo stage remains fixed, resulting in a mismatch between the real height and the apparent height in the image. This requires correction factor (α) based on the refractive indices $h = \alpha h'$, where h' is the apparent height and h is the real height (Figure 4-30).

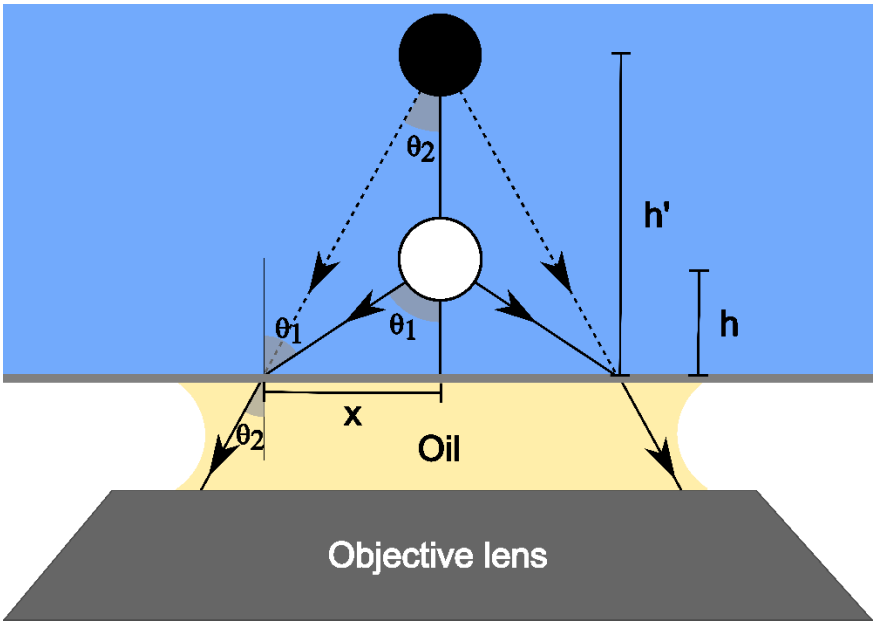

Figure 4-30 Index of refraction mismatch.
The black bead represents the apparent height of the bead and the white bead represents the true height of the bead.

This correction factor *α*, can be derived using the geometry in Figure 4-30:

$$x = h \tan \theta_1 = h' \tan \theta_2. \quad [24]$$

For a small-angle approximation,

$$h \sin \theta_1 = h' \sin \theta_2. \quad [25]$$

This could be combined with Snell's law, to get [1,167]:

$$\alpha = \frac{h}{h'} \approx \frac{\sin \theta_2}{\sin \theta_1} = \frac{n_w}{n_o}, \quad [26]$$

From this, we find that α = 0.88 is the correction that we should use for our height measurements if using a low numerical aperture objective lens. However, because our instrument has an objective that has an NA of 1.5 (necessary for TIRF illumination), this approximation might not hold and could be improved with a different approximation[168]. So, the validity of Equation [26] should be addressed in future experiments.

4.3. Temperature control

Temperature is a critical factor in biological systems, as even slight changes can significantly alter the behavior of some biomolecules. Implementing a temperature control system is experimentally valuable for exploring how temperature influences various behaviors. For example, one of the most intriguing aspects about collagen behavior is that even though it does many functions inside our bodies, it is unstable at body temperature[28]. This observation suggests that single-molecule force experiments with collagen at different temperatures are worth exploring.

Our instrument has a temperature-control chamber (UNO T-H-CO2™ from Okolab). Initially, the plan was to perform magnetic tweezers experiments while simultaneously controlling the temperature. However, this is not feasible with the current setup. As discussed in Chapter 2, exerting biologically relevant forces on a magnetic bead requires the magnets to be very close to the sample. With the temperature-control chamber in place (24.1 mm in height) the magnets cannot physically approach the sample, as illustrated in Figure 4-31 (A).

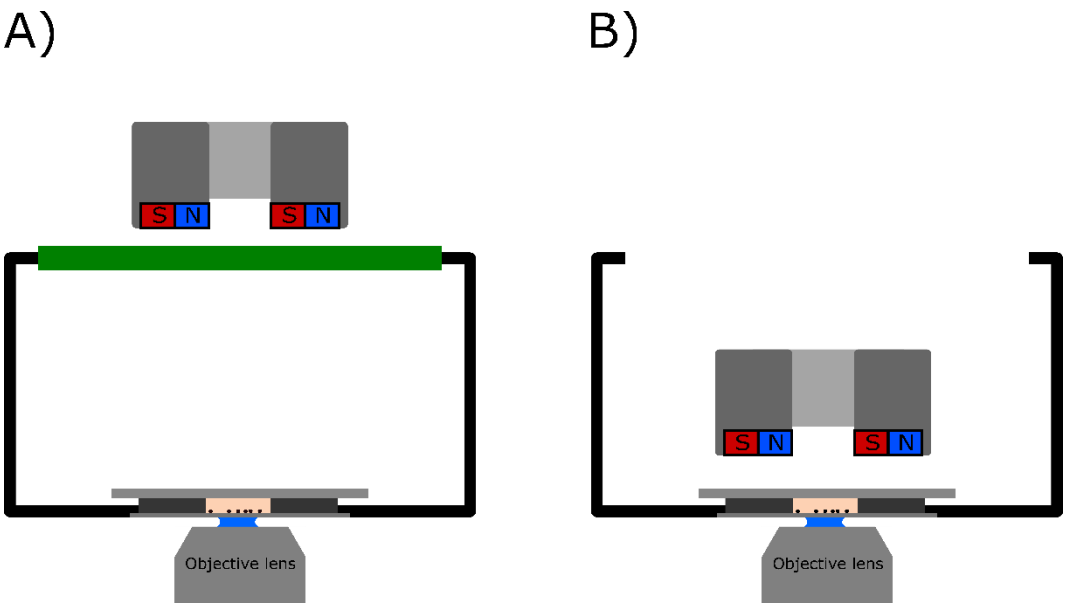

Figure 4-31 Temperature chamber with magnet holder.
A) The black box represents the temperature chamber, which includes heating elements on the sides, the lid (green), and an objective lens heater. B) The chamber without the lid, allowing the magnets to be positioned closer to the sample. This schematic is not to scale.

One potential way to use the temperature-control chamber is to remove the chamber's lid, allowing the magnets to be placed inside the chamber. I tested whether the chamber could reach body temperature (37°C) under these conditions, with the magnet holder inside. After calibration, the chamber reached this temperature in approximately two hours (Figure 4-32). However, further tests are necessary, including stability assessments, varying heating rates, and examining how the distance from the magnets impacts temperature control. It's important to note that demagnetization of the magnets is not a concern, as 37°C is well below the 85°C working temperature of N52 magnets [169], where they start to lose magnetization.

I have integrated control of the temperature-control chamber into a LabVIEW program that controls the instrument (`Magnetic Tweezers instrument with temperature control.vi`, Figure G-2), allowing users to set and monitor the temperature, which can then be used to calculate the force using Equation [15].

A)

B)

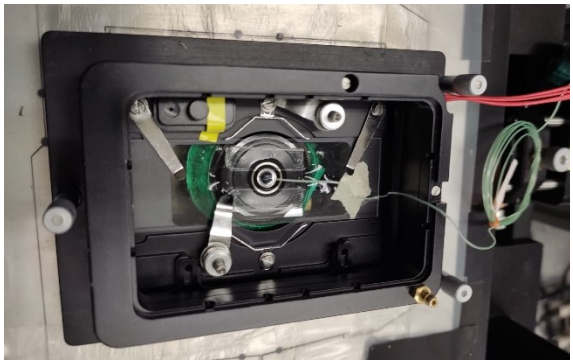

C)

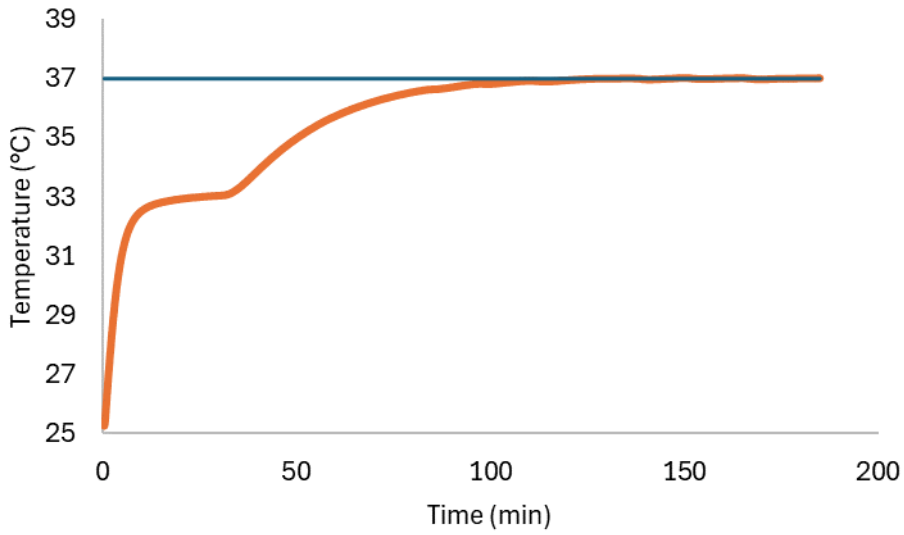

Figure 4-32 Temperature-control chamber.
This experiment was performed by using the temperature-control chamber without the lid, *i.e.*, only using the sides of the chamber and the objective lens heater. A) shows the magnet holder lowered within the temperature-control chamber during the experiment. B) shows the inside part of the temperature-control chamber where the thermocouple was placed, inside a sample chamber similar to the ones used for the bead experiments. C) show the temperature evolution in time of the chamber measured from the thermocouple (orange) and the set temperature (blue).

Chapter 5. Summary and future directions

In this thesis, I have established the foundational methods and characterizations necessary for conducting single-molecule force experiments on biopolymers using Magnetic Tweezers (MT), specifically with the instrument available in the Forde lab. A significant achievement of this work is the enhanced precision in analyzing the bead's height, made possible by modifying sample illumination and analysis algorithms. These improvements are crucial for accurately tracking the mechanical response of biopolymers like DNA and collagen under tension, via their force-extension curves. By refining these analytical techniques, I have opened new opportunities for exploring the impact of molecular interactions and environmental factors at the single-molecule level. Integrating this work with further developments in Total Internal Reflection Fluorescence (TIRF) microscopy, precise temperature control, and optimized tethering protocols will enable the Forde lab to study the complex interplay between mechanical forces, temperature variations, and molecular processes with unprecedented precision.

In terms of the instrument, the magnetic field measurements and analysis conducted in Chapter 2 demonstrate that it is possible to achieve biologically relevant forces (tens of pN), within the range typically attained by other Magnetic Tweezers instruments. It is recommended to construct sample chambers using two coverslips instead of a combination of a microscope slide and a cover slip to achieve forces as high as 42.6 pN. If even greater forces are required, modifications to the instrument setup will be necessary. One approach to increase the force is to adjust the arrangement of the magnets. For instance, reducing the gap between the magnets from 1 mm to 0.5 mm would more than double the force exerted on beads located at the edge of the magnets (Figure 5-1).

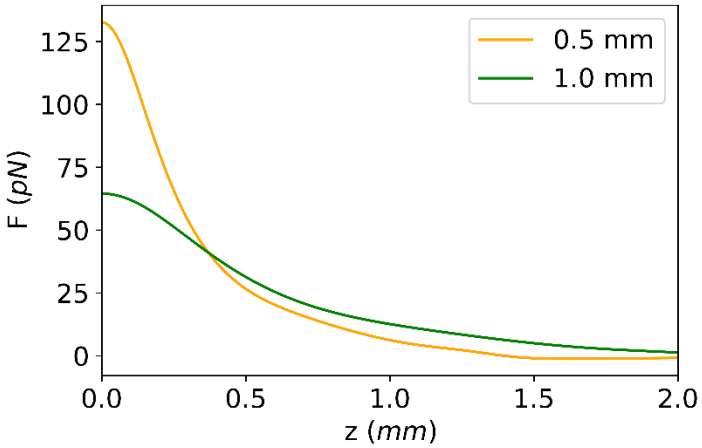

Figure 5-1 Expected force for two different magnet separations.
Simulation to calculate the expected forces exerted on amine Dynabeads at different magnet heights. The orange line represents a magnet separation of 0.5 mm and the green line represents a separation of 1 mm (used currently).

An alternative orientation of the magnets is shown in Figure 5-2 (A). This configuration avoids the issue of a change in the sign of the magnetic field and force, as discussed in Chapter 2 and illustrated in Figure 5-2 (B). Specifically, this orientation can generate a maximum force of 32.1 pN when the magnets are separated by 1 mm and up to 65.7 pN when the separation is reduced to 0.5 mm (Figure 5-2 (C)). These reasons make this orientation worth exploring in the future. Another straightforward way to increase the force involves using larger permanent magnets and larger magnetic beads, as their increased magnetization would result in greater tension applied to the tethered polymers.

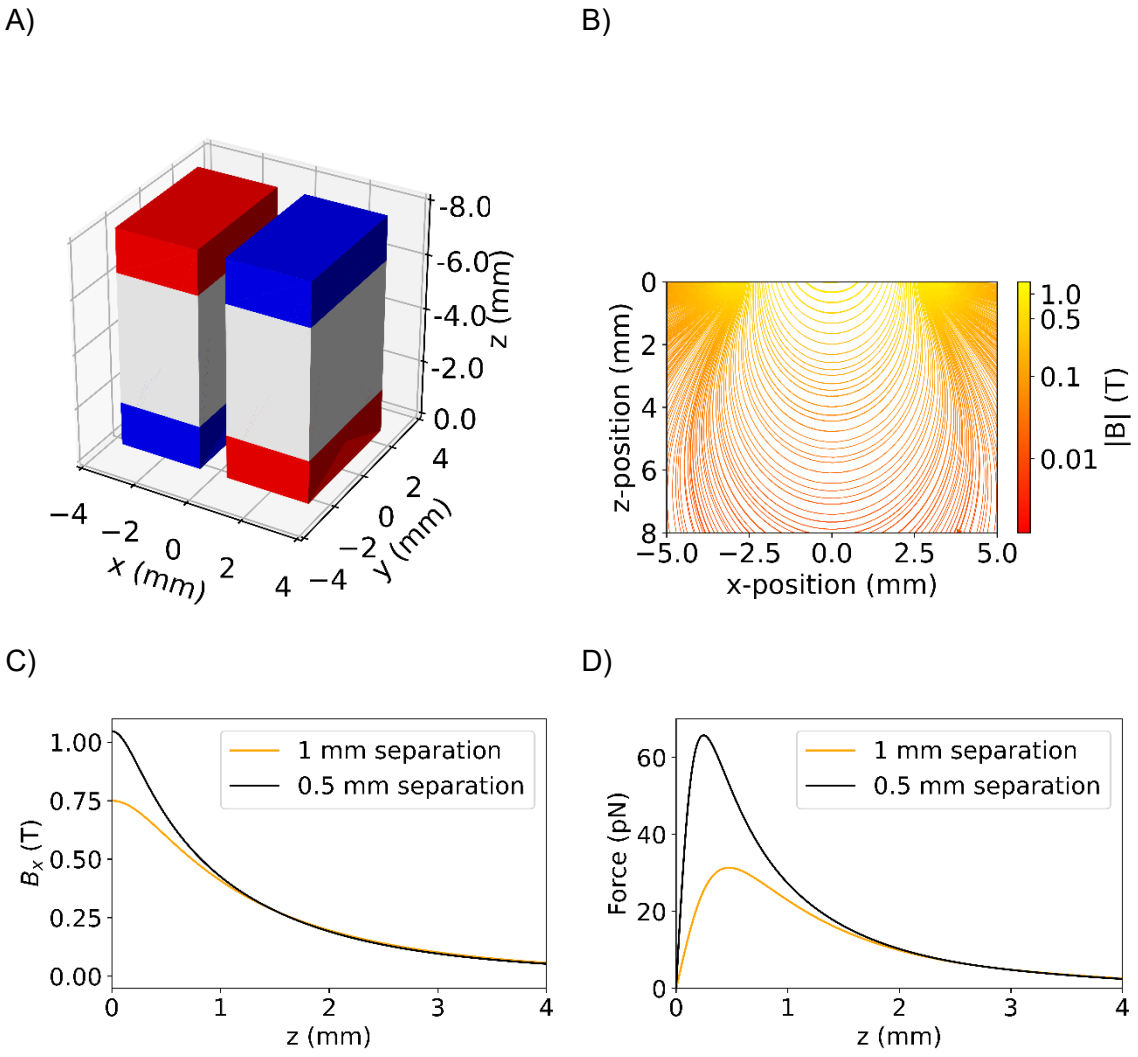

Figure 5-2 Magnets oriented perpendicular to the sample.
A) shows an alternative orientation of the magnets with the long axis perpendicular to the sample. B) presents the magnetic field simulated below the magnets. C) and D) present the magnetic field and force at different distances below the magnets, for 1 mm and 0.5 mm separation.

The objective of Chapter 3, to establish a standardized protocol for tethering DNA, was unfortunately not fully achieved. However, after numerous MAGIC assays, it became clear that the use of amine beads should be abandoned, which was a valuable insight. The tethering protocol is still under development, but the issue of non-specific binding has been resolved with the use of carboxyl beads. It is important to note that while avoiding non-specific binding is generally beneficial, having some beads that bind this way can be useful as fiduciary markers in the sample.

In Chapter 4, I detailed the methods for measuring forces and precisely determining bead positions to obtain accurate force and polymer extension data during experiments. However, there is room for improvement, both in the algorithm and the illumination setup. On the instrumental side, enhancing bead tracking could be achieved by changing the excitation light. This could be achieved using a superluminescent diode coupled with a collimating lens to produce better-collimated light. Additionally, the diode could be combined with a single-mode fiber to guide the light through the magnet holder hole. Alternatively, EPI illumination could be employed to bypass the issue of the magnet position interfering with the light path, as implemented in the Poirier lab[136]. On the algorithm side, an improvement would be to average multiple images of the region of interest (ROI) where the bead is located, both for creating the LUT and for analyzing the bead whose height has to be determined, rather than relying on a single image as was done in this thesis. Also, taking radial profiles at multiple angles for each bead could further enhance resolution.

Additionally, in Chapter 4, I characterized bead fluctuations using Allan variance to distinguish fluctuation behaviors across various time scales. By examining fiduciary beads, I demonstrated how the optimal time to measure the bead fluctuations can be identified through Allan deviation plots. The analysis indicated that the optimal time window for measuring thermally induced bead fluctuations for that specific sample was around 3 seconds, guided by the minimum of the Allan plot. This methodology provides a solid foundation for future studies on tethered beads, where similar fluctuation behavior is expected, though with different timescales due to the lower restoring stiffness of tethered beads

In experiments in which the data should be analyzed simultaneously as the experiment is being conducted, I suggest using the LabVIEW program `Magnetic Tweezers for Instrument final RMS and record.vi`(Figure G-1) with the RMS algorithm. Although this method is less precise when the magnet height is changed, it executes quickly and can be useful during real-time measurements to monitor the progress of the experiment. Simultaneously, the images can be saved for later analysis with the correlation algorithm program (`Correlation algorithm final.vi`, Figure G-3), which provides greater precision (standard deviation = 1.8 nm) in determining bead height when the magnet height is changed. If a high frame rate is required for a specific experiment, I suggest using a simple program that focuses only on

saving the images, without processing them simultaneously (`Saving images.vi`, Figure G-4).

Two main adjustments should be made when using MT (Magnetic Tweezers) along with TIRF (Total Internal Reflection Fluorescence) microscopy:

1) If the dichroic-based TIRF illumination is used (Figure 2-12 (A)), the current setup includes a quad-band optical element (Chroma, ZT 405/488/561/640 rpcv2-uf2). This optic reflects light in the narrow band gaps of the four laser lines, directing them to one side of the objective lens to produce TIR illumination while transmitting outside these narrow band gaps to allow light to reach the cameras. However, the transmission of this quad-band set in the spectral part used for MT detection (*i.e.*, > 775 nm) is low and furthermore results in an intensity gradient in the MT camera's field of view. This issue can be easily resolved by acquiring a similar optic that also transmits effectively in this part of the spectrum. It's important to note that when using micromirror-based TIRF (Figure 2-12 (B)), this issue does not arise because the quad-band element is not required.

2) The MT and TIRF detection systems are aligned so that their focal planes coincide within the sample. However, for MT detection, the beads need to be out of focus to produce a diffraction pattern that can be used to calculate their height. To use MT and TIRF together, the TIRF system should be focused on the bottom surface of the sample, while the MT system should be out of focus above the bottom surface to use fiduciary beads for drift correction. One way to achieve this is by modifying the optical arrangement after the light coming from the sample is separated (as shown in the red component in Figure 2-1) and before it reaches the MT camera, ensuring that the beads are out of focus.

This thesis focused on the development, optimization, and characterization of a magnetic tweezers instrument for single-molecule force experiments, with the future aim of studying collagen's mechanical properties. The improved instrument now enables precise force-extension measurements, providing valuable insights into the behavior of various polymers under mechanical stress. Advanced algorithms were implemented to precisely analyze bead fluctuations and height positions, with significant improvements in the accuracy of height detection achieved through modifications in the algorithms and

experimental set-up. Additionally, certain limitations of the system were characterized, offering a more comprehensive understanding of its performance. These refinements enhance the technical capabilities of our single-molecule manipulation systems, establishing a robust platform for future investigations into protein mechanics and their biological significance.

References

(1) Sarkar, R.; Rybenkov, V. V. A Guide to Magnetic Tweezers and Their Applications. *Front. Phys.* **2016**, *4*.

(2) Seol, Y.; Neuman, K. C. Magnetic Tweezers for Single-Molecule Manipulation. *Methods Mol. Biol. Clifton NJ* **2011**, *783*, 265–293. https://doi.org/10.1007/978-1-61779-282-3_15.

(3) Neuman, K. C.; Nagy, A. Single-Molecule Force Spectroscopy: Optical Tweezers, Magnetic Tweezers and Atomic Force Microscopy. *Nat. Methods* **2008**, *5* (6), 491–505. https://doi.org/10.1038/nmeth.1218.

(4) Tanase, M.; Biais, N.; Sheetz, M. Magnetic Tweezers in Cell Biology. In *Methods in Cell Biology*; Cell Mechanics; Academic Press, 2007; Vol. 83, pp 473–493. https://doi.org/10.1016/S0091-679X(07)83020-2.

(5) De Vlaminck, I.; Dekker, C. Recent Advances in Magnetic Tweezers. *Annu. Rev. Biophys.* **2012**, *41* (1), 453–472. https://doi.org/10.1146/annurev-biophys-122311-100544.

(6) Madariaga-Marcos, J.; Hormeño, S.; Pastrana, C. L.; Fisher, G. L. M.; Dillingham, M. S.; Moreno-Herrero, F. Force Determination in Lateral Magnetic Tweezers Combined with TIRF Microscopy. *Nanoscale* **2018**, *10* (9), 4579–4590. https://doi.org/10.1039/C7NR07344E.

(7) Franklin, R. E.; Gosling, R. G. Molecular Configuration in Sodium Thymonucleate. *Nature* **1953**, *171* (4356), 740–741. https://doi.org/10.1038/171740a0.

(8) Watson, J. D.; Crick, F. H. C. Molecular Structure of Nucleic Acids: A Structure for Deoxyribose Nucleic Acid. *Nature* **1953**, *171* (4356), 737–738. https://doi.org/10.1038/171737a0.

(9) Engel, G. S.; Calhoun, T. R.; Read, E. L.; Ahn, T.-K.; Mančal, T.; Cheng, Y.-C.; Blankenship, R. E.; Fleming, G. R. Evidence for Wavelike Energy Transfer through Quantum Coherence in Photosynthetic Systems. *Nature* **2007**, *446* (7137), 782–786. https://doi.org/10.1038/nature05678.

(10) Scholes, G. D.; Fleming, G. R.; Olaya-Castro, A.; van Grondelle, R. Lessons from Nature about Solar Light Harvesting. *Nat. Chem.* **2011**, *3* (10), 763–774. https://doi.org/10.1038/nchem.1145.

(11) Lehmann, K.; Shayegan, M.; Blab, G. A.; Forde, N. R. Optical Tweezers Approaches for Probing Multiscale Protein Mechanics and Assembly. *Front. Mol. Biosci.* **2020**, *7*.

(12) Kirkness, M. W.; Lehmann, K.; Forde, N. R. Mechanics and Structural Stability of the Collagen Triple Helix. *Curr. Opin. Chem. Biol.* **2019**, *53*, 98–105. https://doi.org/10.1016/j.cbpa.2019.08.001.

(13) Bustamante, C. J.; Chemla, Y. R.; Liu, S.; Wang, M. D. Optical Tweezers in Single-Molecule Biophysics. *Nat. Rev. Methods Primer* **2021**, *1* (1), 1–29. https://doi.org/10.1038/s43586-021-00021-6.

(14) Ritzefeld, M.; Walhorn, V.; Anselmetti, D.; Sewald, N. Analysis of DNA Interactions Using Single-Molecule Force Spectroscopy. *Amino Acids* **2013**, *44* (6), 1457–1475. https://doi.org/10.1007/s00726-013-1474-4.

(15) Eckel, R.; Ros, R.; Ros, A.; Wilking, S. D.; Sewald, N.; Anselmetti, D. Identification of Binding Mechanisms in Single Molecule–DNA Complexes. *Biophys. J.* **2003**, *85* (3), 1968–1973.

(16) Camp, R. J.; Liles, M.; Beale, J.; Saeidi, N.; Flynn, B. P.; Moore, E.; Murthy, S. K.; Ruberti, J. W. Molecular Mechanochemistry: Low Force Switch Slows Enzymatic Cleavage of Human Type I Collagen Monomer. *J. Am. Chem. Soc.* **2011**, *133* (11), 4073–4078. https://doi.org/10.1021/ja110098b.

(17) Löf, A.; Walker, P. U.; Sedlak, S. M.; Gruber, S.; Obser, T.; Brehm, M. A.; Benoit, M.; Lipfert, J. Multiplexed Protein Force Spectroscopy Reveals Equilibrium Protein Folding Dynamics and the Low-Force Response of von Willebrand Factor. *Proc. Natl. Acad. Sci.* **2019**, *116* (38), 18798–18807. https://doi.org/10.1073/pnas.1901794116.

(18) Miller, H.; Zhou, Z.; Shepherd, J.; Wollman, A. J. M.; Leake, M. C. Single-Molecule Techniques in Biophysics: A Review of the Progress in Methods and Applications. *Rep. Prog. Phys.* **2017**, *81* (2), 024601. https://doi.org/10.1088/1361-6633/aa8a02.

(19) Tarnutzer, K.; Siva Sankar, D.; Dengjel, J.; Ewald, C. Y. Collagen Constitutes about 12% in Females and 17% in Males of the Total Protein in Mice. *Sci. Rep.* **2023**, *13* (1), 4490. https://doi.org/10.1038/s41598-023-31566-z.

(20) Al-Shaer, A.; Lyons, A.; Forde, N. R. Characterizing the Flexibility of the Body's Building Block: Collagen. 4.

(21) Shoulders, M. D.; Raines, R. T. Collagen Structure and Stability. *Annu. Rev. Biochem.* **2009**, *78* (1), 929–958. https://doi.org/10.1146/annurev.biochem.77.032207.120833.

(22) Mathew-Steiner, S. S.; Roy, S.; Sen, C. K. Collagen in Wound Healing. *Bioengineering* **2021**, *8* (5), 63. https://doi.org/10.3390/bioengineering8050063.

(23) Monteiro, G. A.; Fernandes, A. V.; Sundararaghavan, H. G.; Shreiber, D. I. Positively and Negatively Modulating Cell Adhesion to Type I Collagen Via Peptide Grafting. *Tissue Eng. Part A* **2011**, *17* (13–14), 1663–1673. https://doi.org/10.1089/ten.tea.2008.0346.

(24) Holmes, D. F.; Lu, Y.; Starborg, T.; Kadler, K. E. Chapter Three - Collagen Fibril Assembly and Function. In *Current Topics in Developmental Biology*; Litscher, E. S., Wassarman, P. M., Eds.; Extracellular Matrix and Egg Coats; Academic Press, 2018; Vol. 130, pp 107–142. https://doi.org/10.1016/bs.ctdb.2018.02.004.

(25) Wang, H. A Review of the Effects of Collagen Treatment in Clinical Studies. *Polymers* **2021**, *13* (22), 3868. https://doi.org/10.3390/polym13223868.

(26) Sorushanova, A.; Delgado, L. M.; Wu, Z.; Shologu, N.; Kshirsagar, A.; Raghunath, R.; Mullen, A. M.; Bayon, Y.; Pandit, A.; Raghunath, M.; Zeugolis, D. I. The Collagen Suprafamily: From Biosynthesis to Advanced Biomaterial Development. *Adv. Mater.* **2019**, *31* (1), 1801651. https://doi.org/10.1002/adma.201801651.

(27) Bailey, A. J.; Paul, R. G.; Knott, L. Mechanisms of Maturation and Ageing of Collagen. *Mech. Ageing Dev.* **1998**, *106* (1), 1–56. https://doi.org/10.1016/S0047-6374(98)00119-5.

(28) Leikina, E.; Mertts, M. V.; Kuznetsova, N.; Leikin, S. Type I Collagen Is Thermally Unstable at Body Temperature. *Proc. Natl. Acad. Sci.* **2002**, *99* (3), 1314–1318. https://doi.org/10.1073/pnas.032307099.

(29) Orgel, J. P. R. O.; San Antonio, J. D.; Antipova, O. Molecular and Structural Mapping of Collagen Fibril Interactions. *Connect. Tissue Res.* **2011**, *52* (1), 2–17. https://doi.org/10.3109/03008207.2010.511353.

(30) Bella, J.; Eaton, M.; Brodsky, B.; Berman, H. M. Crystal and Molecular Structure of a Collagen-Like Peptide at 1.9 Å Resolution. *Science* **1994**. https://doi.org/10.1126/science.7695699.

(31) Okuyama, K.; Okuyama, K.; Arnott, S.; Takayanagi, M.; Kakudo, M. Crystal and Molecular Structure of a Collagen-like Polypeptide (Pro-Pro-Gly)10. *J. Mol. Biol.* **1981**, *152* (2), 427–443. https://doi.org/10.1016/0022-2836(81)90252-7.

(32) Buehler, M. J. Nature Designs Tough Collagen: Explaining the Nanostructure of Collagen Fibrils. *Proc. Natl. Acad. Sci.* **2006**, *103* (33), 12285–12290. https://doi.org/10.1073/pnas.0603216103.

(33) Wenger, M. P. E.; Bozec, L.; Horton, M. A.; Mesquida, P. Mechanical Properties of Collagen Fibrils. *Biophys. J.* **2007**, *93* (4), 1255–1263. https://doi.org/10.1529/biophysj.106.103192.

(34) van der Rijt, J. A. J.; van der Werf, K. O.; Bennink, M. L.; Dijkstra, P. J.; Feijen, J. Micromechanical Testing of Individual Collagen Fibrils. *Macromol. Biosci.* **2006**, *6* (9), 697–702. https://doi.org/10.1002/mabi.200600063.

(35) Veld, P. J. in't; Stevens, M. J. Simulation of the Mechanical Strength of a Single Collagen Molecule. *Biophys. J.* **2008**, *95* (1), 33–39. https://doi.org/10.1529/biophysj.107.120659.

(36) Rezaei, N.; Lyons, A.; Forde, N. R. Environmentally Controlled Curvature of Single Collagen Proteins. *Biophys. J.* **2018**, *115* (8), 1457–1469. https://doi.org/10.1016/j.bpj.2018.09.003.

(37) Sun, Y.-L.; Luo, Z.-P.; Fertala, A.; An, K.-N. Direct Quantification of the Flexibility of Type I Collagen Monomer. *Biochem. Biophys. Res. Commun.* **2002**, *295* (2), 382–386. https://doi.org/10.1016/S0006-291X(02)00685-X.

(38) Sun, Y.-L.; Luo, Z.-P.; Fertala, A.; An, K.-N. Stretching Type II Collagen with Optical Tweezers. *J. Biomech.* **2004**, *37* (11), 1665–1669. https://doi.org/10.1016/j.jbiomech.2004.02.028.

(39) Rezaei, N.; Downing, B. P. B.; Wieczorek, A.; Chan, C. K. Y.; Welch, R. L.; Forde, N. R. Using Optical Tweezers to Study Mechanical Properties of Collagen. In *Photonics North 2011*; SPIE, 2011; Vol. 8007, pp 146–155. https://doi.org/10.1117/12.905714.

(40) Shayegan, M.; Rezaei, N.; Lam, N. H.; Altindal, T.; Wieczorek, A.; Forde, N. R. Probing Multiscale Mechanics of Collagen with Optical Tweezers. In *Optical Trapping and Optical Micromanipulation X*; SPIE, 2013; Vol. 8810, pp 200–209. https://doi.org/10.1117/12.2027258.

(41) Wieczorek, A.; Rezaei, N.; Chan, C. K.; Xu, C.; Panwar, P.; Brömme, D.; Merschrod S., E. F.; Forde, N. R. Development and Characterization of a Eukaryotic Expression System for Human Type II Procollagen. *BMC Biotechnol.* **2015**, *15* (1), 112. https://doi.org/10.1186/s12896-015-0228-7.

(42) Kirkness, M. W. H.; Forde, N. R. Single-Molecule Assay for Proteolytic Susceptibility: Force-Induced Collagen Destabilization. *Biophys. J.* **2018**, *114* (3), 570–576. https://doi.org/10.1016/j.bpj.2017.12.006.

(43) Adhikari, A. S.; Chai, J.; Dunn, A. R. Mechanical Load Induces a 100-Fold Increase in the Rate of Collagen Proteolysis by MMP-1. *J. Am. Chem. Soc.* **2011**, *133* (6), 1686–1689. https://doi.org/10.1021/ja109972p.

(44) Adhikari, A. S.; Glassey, E.; Dunn, A. R. Conformational Dynamics Accompanying the Proteolytic Degradation of Trimeric Collagen I by Collagenases. *J. Am. Chem. Soc.* **2012**, *134* (32), 13259–13265. https://doi.org/10.1021/ja212170b.

(45) Tang, M.; Li, T.; Pickering, E.; Gandhi, N. S.; Burrage, K.; Gu, Y. Steered Molecular Dynamics Characterization of the Elastic Modulus and Deformation Mechanisms of Single Natural Tropocollagen Molecules. *J. Mech. Behav. Biomed. Mater.* **2018**, *86*, 359–367. https://doi.org/10.1016/j.jmbbm.2018.07.009.

(46) Buehler, M. J.; Wong, S. Y. Entropic Elasticity Controls Nanomechanics of Single Tropocollagen Molecules. *Biophys. J.* **2007**, *93* (1), 37–43. https://doi.org/10.1529/biophysj.106.102616.

(47) Al-Shaer, A.; Lyons, A.; Ishikawa, Y.; Hudson, B. G.; Boudko, S. P.; Forde, N. R. Sequence-Dependent Mechanics of Collagen Reflect Its Structural and Functional Organization. *Biophys. J.* **2021**, *120* (18), 4013–4028. https://doi.org/10.1016/j.bpj.2021.08.013.

(48) Sorushanova, A.; Delgado, L. M.; Wu, Z.; Shologu, N.; Kshirsagar, A.; Raghunath, R.; Mullen, A. M.; Bayon, Y.; Pandit, A.; Raghunath, M.; Zeugolis, D. I. The Collagen Suprafamily: From Biosynthesis to Advanced Biomaterial Development. *Adv. Mater.* **2019**, *31* (1), 1801651. https://doi.org/10.1002/adma.201801651.

(49) Lovelady, H. H.; Shashidhara, S.; Matthews, W. G. Solvent Specific Persistence Length of Molecular Type I Collagen. *Biopolymers* **2014**, *101* (4), 329–335. https://doi.org/10.1002/bip.22365.

(50) Sarkar, S. K.; Marmer, B.; Goldberg, G.; Neuman, K. C. Single-Molecule Tracking of Collagenase on Native Type I Collagen Fibrils Reveals Degradation Mechanism. *Curr. Biol.* **2012**, *22* (12), 1047–1056. https://doi.org/10.1016/j.cub.2012.04.012.

(51) Shayegan, M.; Altindal, T.; Kiefl, E.; Forde, N. R. Intact Telopeptides Enhance Interactions between Collagens. *Biophys. J.* **2016**, *111* (11), 2404–2416. https://doi.org/10.1016/j.bpj.2016.10.039.

(52) Altindal, T.; Shayegan, M.; Kiefl, E.; Forde, N. R. Probing Telopeptide-Induced Collagen-Collagen Interactions Using Optical-Tweezers-Based Microrheology. In *Optics in the Life Sciences (2015), paper OtM3E.3*; Optica Publishing Group, 2015; p OtM3E.3. https://doi.org/10.1364/OTA.2015.OtM3E.3.

(53) Shayegan, M.; Forde, N. R. Probing the Viscoelasticity of Collagen Solutions via Optical-Tweezers-Based Microrheology. *MRS Online Proc. Libr. OPL* **2012**, *1465*, mrss12. https://doi.org/10.1557/opl.2012.964.

(54) Shayegan, M.; Forde, N. R. Microrheological Characterization of Collagen Systems: From Molecular Solutions to Fibrillar Gels. *PLOS ONE* **2013**, *8* (8), e70590. https://doi.org/10.1371/journal.pone.0070590.

(55) Lee, C. H.; Singla, A.; Lee, Y. Biomedical Applications of Collagen. *Int. J. Pharm.* **2001**, *221* (1), 1–22. https://doi.org/10.1016/S0378-5173(01)00691-3.

(56) Li, Z.; Du, T.; Ruan, C.; Niu, X. Bioinspired Mineralized Collagen Scaffolds for Bone Tissue Engineering. *Bioact. Mater.* **2021**, *6* (5), 1491–1511. https://doi.org/10.1016/j.bioactmat.2020.11.004.

(57) Haider, A.; Haider, S.; Rao Kummara, M.; Kamal, T.; Alghyamah, A.-A. A.; Jan Iftikhar, F.; Bano, B.; Khan, N.; Amjid Afridi, M.; Soo Han, S.; Alrahlah, A.; Khan, R. Advances in the Scaffolds Fabrication Techniques Using Biocompatible Polymers and Their Biomedical Application: A Technical and Statistical Review. *J. Saudi Chem. Soc.* **2020**, *24* (2), 186–215. https://doi.org/10.1016/j.jscs.2020.01.002.

(58) Yannas, I. V. Tissue Regeneration by Use of Collagen-Glycosaminoglycan Copolymers. *Clin. Mater.* **1992**, *9* (3), 179–187. https://doi.org/10.1016/0267-6605(92)90098-E.

(59) López-Otín, C.; Blasco, M. A.; Partridge, L.; Serrano, M.; Kroemer, G. The Hallmarks of Aging. *Cell* **2013**, *153* (6), 1194–1217. https://doi.org/10.1016/j.cell.2013.05.039.

(60) Chen, Y.; Liang, C.-P.; Liu, Y.; Fischer, A. H.; Parwani, A. V.; Pantanowitz, L. Review of Advanced Imaging Techniques. *J. Pathol. Inform.* **2012**, *3* (1), 22. https://doi.org/10.4103/2153-3539.96751.

(61) Koenderink, A. F.; Tsukanov, R.; Enderlein, J.; Izeddin, I.; Krachmalnicoff, V. Super-Resolution Imaging: When Biophysics Meets Nanophotonics. *Nanophotonics* **2022**, *11* (2), 169–202. https://doi.org/10.1515/nanoph-2021-0551.

(62) Kherlopian, A. R.; Song, T.; Duan, Q.; Neimark, M. A.; Po, M. J.; Gohagan, J. K.; Laine, A. F. A Review of Imaging Techniques for Systems Biology. *BMC Syst. Biol.* **2008**, *2* (1), 74. https://doi.org/10.1186/1752-0509-2-74.

(63) Clausen-Schaumann, H.; Seitz, M.; Krautbauer, R.; Gaub, H. E. Force Spectroscopy with Single Bio-Molecules. *Curr. Opin. Chem. Biol.* **2000**, *4* (5), 524–530. https://doi.org/10.1016/S1367-5931(00)00126-5.

(64) Yang, B.; Liu, Z.; Liu, H.; Nash, M. A. Next Generation Methods for Single-Molecule Force Spectroscopy on Polyproteins and Receptor-Ligand Complexes. *Front. Mol. Biosci.* **2020**, *7*. https://doi.org/10.3389/fmolb.2020.00085.

(65) Mandal, S. S. Force Spectroscopy on Single Molecules of Life. *ACS Omega* **2020**, *5* (20), 11271–11278. https://doi.org/10.1021/acsomega.0c00814.

(66) Baselt, D. R.; Revel, J. P.; Baldeschwieler, J. D. Subfibrillar Structure of Type I Collagen Observed by Atomic Force Microscopy. *Biophys. J.* **1993**, *65* (6), 2644–2655. https://doi.org/10.1016/S0006-3495(93)81329-8.

(67) Bozec, L.; Odlyha, M. Thermal Denaturation Studies of Collagen by Microthermal Analysis and Atomic Force Microscopy. *Biophys. J.* **2011**, *101* (1), 228–236. https://doi.org/10.1016/j.bpj.2011.04.033.

(68) Unksov, I. N.; Korosec, C. S.; Surendiran, P.; Verardo, D.; Lyttleton, R.; Forde, N. R.; Linke, H. Through the Eyes of Creators: Observing Artificial Molecular Motors. *ACS Nanosci. Au* **2022**, *2* (3), 140–159. https://doi.org/10.1021/acsnanoscienceau.1c00041.

(69) Vicidomini, G.; Bianchini, P.; Diaspro, A. STED Super-Resolved Microscopy. *Nat. Methods* **2018**, *15* (3), 173–182. https://doi.org/10.1038/nmeth.4593.

(70) Betzig, E.; Patterson, G. H.; Sougrat, R.; Lindwasser, O. W.; Olenych, S.; Bonifacino, J. S.; Davidson, M. W.; Lippincott-Schwartz, J.; Hess, H. F. Imaging Intracellular Fluorescent Proteins at Nanometer Resolution. *Science* **2006**, *313* (5793), 1642–1645. https://doi.org/10.1126/science.1127344.

(71) Rust, M. J.; Bates, M.; Zhuang, X. Sub-Diffraction-Limit Imaging by Stochastic Optical Reconstruction Microscopy (STORM). *Nat. Methods* **2006**, *3* (10), 793–796. https://doi.org/10.1038/nmeth929.

(72) Balzarotti, F.; Eilers, Y.; Gwosch, K. C.; Gynnå, A. H.; Westphal, V.; Stefani, F. D.; Elf, J.; Hell, S. W. Nanometer Resolution Imaging and Tracking of Fluorescent Molecules with Minimal Photon Fluxes. *Science* **2017**, *355* (6325), 606–612. https://doi.org/10.1126/science.aak9913.

(73) Göttfert, F.; Wurm, C. A.; Mueller, V.; Berning, S.; Cordes, V. C.; Honigmann, A.; Hell, S. W. Coaligned Dual-Channel STED Nanoscopy and Molecular Diffusion Analysis at 20 Nm Resolution. *Biophys. J.* **2013**, *105* (1), L01–L03. https://doi.org/10.1016/j.bpj.2013.05.029.

(74) Fish, K. N. Total Internal Reflection Fluorescence (TIRF) Microscopy. *Curr. Protoc. Cytom.* **2009**, *50* (1), 12.18.1-12.18.13. https://doi.org/10.1002/0471142956.cy1218s50.

(75) Axelrod, D. Total Internal Reflection Fluorescence Microscopy in Cell Biology. *Traffic* **2001**, *2* (11), 764–774. https://doi.org/10.1034/j.1600-0854.2001.21104.x.

(76) Gell, C.; Berndt, M.; Enderlein, J.; Diez, S. TIRF Microscopy Evanescent Field Calibration Using Tilted Fluorescent Microtubules. *J. Microsc.* **2009**, *234* (1), 38–46. https://doi.org/10.1111/j.1365-2818.2009.03147.x.

(77) Unno, N.; Maeda, A.; Satake, S.; Tsuji, T.; Taniguchi, J. Fabrication of Nanostep for Total Internal Reflection Fluorescence Microscopy to Calibrate in Water. *Microelectron. Eng.* **2015**, *133*, 98–103. https://doi.org/10.1016/j.mee.2014.12.002.

(78) Saxton, M. J. Lateral Diffusion in an Archipelago. Single-Particle Diffusion. *Biophys. J.* **1993**, *64* (6), 1766–1780.

(79) Eggeling, C.; Ringemann, C.; Medda, R.; Schwarzmann, G.; Sandhoff, K.; Polyakova, S.; Belov, V. N.; Hein, B.; von Middendorff, C.; Schönle, A.; Hell, S. W. Direct Observation of the Nanoscale Dynamics of Membrane Lipids in a Living Cell. *Nature* **2009**, *457* (7233), 1159–1162. https://doi.org/10.1038/nature07596.

(80) Herbst, K. J.; Ni, Q.; Zhang, J. Dynamic Visualization of Signal Transduction in Living Cells: From Second Messengers to Kinases. *IUBMB Life* **2009**, *61* (9), 902–908. https://doi.org/10.1002/iub.232.

(81) Axelrod, D.; Koppel, D. E.; Schlessinger, J.; Elson, E.; Webb, W. W. Mobility Measurement by Analysis of Fluorescence Photobleaching Recovery Kinetics. *Biophys. J.* **1976**, *16* (9), 1055–1069. https://doi.org/10.1016/S0006-3495(76)85755-4.

(82) Holden, S. J.; Uphoff, S.; Hohlbein, J.; Yadin, D.; Le Reste, L.; Britton, O. J.; Kapanidis, A. N. Defining the Limits of Single-Molecule FRET Resolution in TIRF Microscopy. *Biophys. J.* **2010**, *99* (9), 3102–3111. https://doi.org/10.1016/j.bpj.2010.09.005.

(83) Maki, K.; Han, S.-W.; Hirano, Y.; Yonemura, S.; Hakoshima, T.; Adachi, T. Real-Time TIRF Observation of Vinculin Recruitment to Stretched α-Catenin by AFM. *Sci. Rep.* **2018**, *8* (1), 1575. https://doi.org/10.1038/s41598-018-20115-8.

(84) Seol, Y.; Neuman, K. C. Combined Magnetic Tweezers and Micro-Mirror Total Internal Reflection Fluorescence Microscope for Single-Molecule Manipulation and Visualization. In *Single Molecule Analysis: Methods and Protocols*; Peterman, E. J. G., Ed.; Methods in Molecular Biology; Springer: New York, NY, 2018; pp 297–316. https://doi.org/10.1007/978-1-4939-7271-5_16.

(85) Cordova, J. C.; Das, D. K.; Manning, H. W.; Lang, M. J. Combining Single-Molecule Manipulation and Single-Molecule Detection. *Curr. Opin. Struct. Biol.* **2014**, *28*, 142–148. https://doi.org/10.1016/j.sbi.2014.08.010.

(86) Chen, H.; Chandrasekar, S.; Sheetz, M. P.; Stossel, T. P.; Nakamura, F.; Yan, J. Mechanical Perturbation of Filamin A Immunoglobulin Repeats 20-21 Reveals Potential Non-Equilibrium Mechanochemical Partner Binding Function. *Sci. Rep.* **2013**, *3* (1), 1642. https://doi.org/10.1038/srep01642.

(87) King, G. A.; Gross, P.; Bockelmann, U.; Modesti, M.; Wuite, G. J. L.; Peterman, E. J. G. Revealing the Competition between Peeled ssDNA, Melting Bubbles, and S-DNA during DNA Overstretching Using Fluorescence Microscopy. *Proc. Natl. Acad. Sci.* **2013**, *110* (10), 3859–3864. https://doi.org/10.1073/pnas.1213676110.

(88) Zhang, X.; Chen, H.; Le, S.; Rouzina, I.; Doyle, P. S.; Yan, J. Revealing the Competition between Peeled ssDNA, Melting Bubbles, and S-DNA during DNA Overstretching by Single-Molecule Calorimetry. *Proc. Natl. Acad. Sci.* **2013**, *110* (10), 3865–3870. https://doi.org/10.1073/pnas.1213740110.

(89) Almaqwashi, A. A.; Paramanathan, T.; Rouzina, I.; Williams, M. C. Mechanisms of Small Molecule–DNA Interactions Probed by Single-Molecule Force Spectroscopy. *Nucleic Acids Res.* **2016**, *44* (9), 3971–3988. https://doi.org/10.1093/nar/gkw237.

(90) Bustamante, C.; Macosko, J. C.; Wuite, G. J. L. Grabbing the Cat by the Tail: Manipulating Molecules One by One. *Nat. Rev. Mol. Cell Biol.* **2000**, *1* (2), 130–136. https://doi.org/10.1038/35040072.

(91) Dudko, O. K.; Hummer, G.; Szabo, A. Intrinsic Rates and Activation Free Energies from Single-Molecule Pulling Experiments. *Phys. Rev. Lett.* **2006**, *96* (10), 108101. https://doi.org/10.1103/PhysRevLett.96.108101.

(92) Brutzer, H.; Luzzietti, N.; Klaue, D.; Seidel, R. Energetics at the DNA Supercoiling Transition. *Biophys. J.* **2010**, *98* (7), 1267–1276. https://doi.org/10.1016/j.bpj.2009.12.4292.

(93) Halvorsen, K.; Wong, W. P. Massively Parallel Single-Molecule Manipulation Using Centrifugal Force. *Biophys. J.* **2010**, *98* (11), L53–L55. https://doi.org/10.1016/j.bpj.2010.03.012.

(94) Sitters, G.; Kamsma, D.; Thalhammer, G.; Ritsch-Marte, M.; Peterman, E. J. G.; Wuite, G. J. L. Acoustic Force Spectroscopy. *Nat. Methods* **2015**, *12* (1), 47–50. https://doi.org/10.1038/nmeth.3183.

(95) Gross, P.; Laurens, N.; Oddershede, L. B.; Bockelmann, U.; Peterman, E. J. G.; Wuite, G. J. L. Quantifying How DNA Stretches, Melts and Changes Twist under Tension. *Nat. Phys.* **2011**, *7* (9), 731–736. https://doi.org/10.1038/nphys2002.

(96) Chiou, C.-H.; Huang, Y.-Y.; Chiang, M.-H.; Lee, H.-H.; Lee, G.-B. New Magnetic Tweezers for Investigation of the Mechanical Properties of Single DNA Molecules. *Nanotechnology* **2006**, *17* (5), 1217. https://doi.org/10.1088/0957-4484/17/5/009.

(97) van Loenhout, M. T. J.; de Grunt, M. V.; Dekker, C. Dynamics of DNA Supercoils. *Science* **2012**, *338* (6103), 94–97. https://doi.org/10.1126/science.1225810.

(98) Bibeau, J. P.; Pandit, N. G.; Gray, S.; Shatery Nejad, N.; Sindelar, C. V.; Cao, W.; De La Cruz, E. M. Twist Response of Actin Filaments. *Proc. Natl. Acad. Sci.* **2023**, *120* (4), e2208536120. https://doi.org/10.1073/pnas.2208536120.

(99) Dulin, D. An Introduction to Magnetic Tweezers. In *Single Molecule Analysis : Methods and Protocols*; Heller, I., Dulin, D., Peterman, E. J. G., Eds.; Springer US: New York, NY, 2024; pp 375–401. https://doi.org/10.1007/978-1-0716-3377-9_18.

(100) Hugel, T.; Michaelis, J.; Hetherington, C. L.; Jardine, P. J.; Grimes, S.; Walter, J. M.; Falk, W.; Anderson, D. L.; Bustamante, C. Experimental Test of Connector Rotation during DNA Packaging into Bacteriophage Φ29 Capsids. *PLOS Biol.* **2007**, *5* (3), e59. https://doi.org/10.1371/journal.pbio.0050059.

(101) Ashkin, A.; Dziedzic, J. M.; Yamane, T. Optical Trapping and Manipulation of Single Cells Using Infrared Laser Beams. *Nature* **1987**, *330* (6150), 769–771. https://doi.org/10.1038/330769a0.

(102) Yang, D.; Ward, A.; Halvorsen, K.; Wong, W. P. Multiplexed Single-Molecule Force Spectroscopy Using a Centrifuge. *Nat. Commun.* **2016**, *7* (1), 11026. https://doi.org/10.1038/ncomms11026.

(103) Marko, J. F.; Siggia, E. D. Stretching DNA. *Macromolecules* **1995**, *28* (26), 8759–8770. https://doi.org/10.1021/ma00130a008.

(104) Wess, T. J. Collagen Fibril Form and Function. In *Advances in Protein Chemistry*; Fibrous Proteins: Coiled-Coils, Collagen and Elastomers; Academic Press, 2005; Vol. 70, pp 341–374. https://doi.org/10.1016/S0065-3233(05)70010-3.

(105) Storm, C.; Nelson, P. C. Theory of High-Force DNA Stretching and Overstretching. *Phys. Rev. E* **2003**, *67* (5), 051906. https://doi.org/10.1103/PhysRevE.67.051906.

(106) Bustamante, C.; Smith, S. B.; Liphardt, J.; Smith, D. Single-Molecule Studies of DNA Mechanics. *Curr. Opin. Struct. Biol.* **2000**, *10* (3), 279–285. https://doi.org/10.1016/S0959-440X(00)00085-3.

(107) Bustamante, C.; Marko, J. F.; Siggia, E. D.; Smith, S. Entropic Elasticity of λ-Phage DNA. *Science* **1994**, *265* (5178), 1599–1600. https://doi.org/10.1126/science.8079175.

(108) Wang, M. D.; Yin, H.; Landick, R.; Gelles, J.; Block, S. M. Stretching DNA with Optical Tweezers. *Biophys. J.* **1997**, *72* (3), 1335–1346. https://doi.org/10.1016/S0006-3495(97)78780-0.

(109) Ribeck, N.; Saleh, O. A. Multiplexed Single-Molecule Measurements with Magnetic Tweezers. *Rev. Sci. Instrum.* **2008**, *79* (9), 094301. https://doi.org/10.1063/1.2981687.

(110) Odijk, T. Stiff Chains and Filaments under Tension. *Macromolecules* **1995**, *28* (20), 7016–7018. https://doi.org/10.1021/ma00124a044.

(111) Krautbauer, R.; Pope, L. H.; Schrader, T. E.; Allen, S.; Gaub, H. E. Discriminating Small Molecule DNA Binding Modes by Single Molecule Force Spectroscopy. *FEBS Lett.* **2002**, *510* (3), 154–158. https://doi.org/10.1016/S0014-5793(01)03257-4.

(112) Strick, T. R.; Allemand, J.-F.; Bensimon, D.; Bensimon, A.; Croquette, V. The Elasticity of a Single Supercoiled DNA Molecule. *Science* **1996**, *271* (5257), 1835–1837. https://doi.org/10.1126/science.271.5257.1835.

(113) Eckel, R.; Wilking, S. D.; Becker, A.; Sewald, N.; Ros, R.; Anselmetti, D. Single-Molecule Experiments in Synthetic Biology: An Approach to the Affinity Ranking of DNA-Binding Peptides. *Angew. Chem. Int. Ed.* **2005**, *44* (25), 3921–3924. https://doi.org/10.1002/anie.200500152.

(114) Paramanathan, T.; Vladescu, I.; McCauley, M. J.; Rouzina, I.; Williams, M. C. Force Spectroscopy Reveals the DNA Structural Dynamics That Govern the Slow Binding of Actinomycin D. *Nucleic Acids Res.* **2012**, *40* (11), 4925–4932. https://doi.org/10.1093/nar/gks069.

(115) Collins, C.; Guilluy, C.; Welch, C.; O'Brien, E. T.; Hahn, K.; Superfine, R.; Burridge, K.; Tzima, E. Localized Tensional Forces on PECAM-1 Elicit a Global Mechanotransduction Response via the Integrin-RhoA Pathway. *Curr. Biol. CB* **2012**, *22* (22), 2087–2094. https://doi.org/10.1016/j.cub.2012.08.051.

(116) Mahowald, J.; Arcizet, D.; Heinrich, D. Impact of External Stimuli and Cell Micro-Architecture on Intracellular Transport States. *ChemPhysChem* **2009**, *10* (9–10), 1559–1566. https://doi.org/10.1002/cphc.200900226.

(117) John David Jackson. *Classical Electrodynamics, 2nd Edition*; 1975.

(118) Ortner, M.; Coliado Bandeira, L. G. Magpylib: A Free Python Package for Magnetic Field Computation. *SoftwareX* **2020**, *11*, 100466. https://doi.org/10.1016/j.softx.2020.100466.

(119) Yang, Z. J.; Johansen, T. H.; Bratsberg, H.; Helgesen, G.; Skjeltorp, A. T. Potential and Force between a Magnet and a Bulk Y1Ba2Cu3O7-δ Superconductor Studied by a Mechanical Pendulum. *Supercond. Sci. Technol.* **1990**, *3* (12), 591. https://doi.org/10.1088/0953-2048/3/12/004.

(120) Xiao-fan, G.; Yong, Y.; Xiao-jing, Z. Analytic Expression of Magnetic Field Distribution of Rectangular Permanent Magnets. *Appl. Math. Mech.* **2004**, *25* (3), 297–306. https://doi.org/10.1007/BF02437333.

(121) Engel-Herbert, R.; Hesjedal, T. Calculation of the Magnetic Stray Field of a Uniaxial Magnetic Domain. *J. Appl. Phys.* **2005**, *97* (7), 074504. https://doi.org/10.1063/1.1883308.

(122) Grob, D. T.; Wise, N.; Oduwole, O.; Sheard, S. Magnetic Susceptibility Characterisation of Superparamagnetic Microspheres. *J. Magn. Magn. Mater.* **2018**, *452*, 134–140. https://doi.org/10.1016/j.jmmm.2017.12.007.

(123) Krishnan, K. M. Fine Particles and Nanostructured Materials. In *Fundamentals and Applications of Magnetic Materials*; Krishnan, K. M., Ed.; Oxford University Press, 2016; p 0. https://doi.org/10.1093/acprof:oso/9780199570447.003.0009.

(124) Thormählen, I.; Straub, J.; Grigull, U. Refractive Index of Water and Its Dependence on Wavelength, Temperature, and Density. *J. Phys. Chem. Ref. Data* **1985**, *14* (4), 933–945. https://doi.org/10.1063/1.555743.

(125) Englert, M.; Hartmann, P.; Reichel, S. Optical Glass: Refractive Index Change with Wavelength and Temperature. In *Optical Modelling and Design III*; SPIE, 2014; Vol. 9131, pp 125–138. https://doi.org/10.1117/12.2052706.

(126) Kirkness, M. W. H.; Korosec, C. S.; Forde, N. R. Modified Pluronic F127 Surface for Bioconjugation and Blocking Nonspecific Adsorption of Microspheres and Biomacromolecules. *Langmuir* **2018**, *34* (45), 13550–13557. https://doi.org/10.1021/acs.langmuir.8b02877.

(127) Li, M.; Jiang, W.; Chen, Z.; Suryaprakash, S.; Lv, S.; Tang, Z.; Chen, X.; Leong, K. W. A Versatile Platform for Surface Modification of Microfluidic Droplets. *Lab. Chip* **2017**, *17* (4), 635–639. https://doi.org/10.1039/c7lc00079k.

(128) Nejadnik, M. R.; Olsson, A. L. J.; Sharma, P. K.; van der Mei, H. C.; Norde, W.; Busscher, H. J. Adsorption of Pluronic F-127 on Surfaces with Different Hydrophobicities Probed by Quartz Crystal Microbalance with Dissipation. *Langmuir* **2009**, *25* (11), 6245–6249. https://doi.org/10.1021/la9001169.

(129) Pan, H.; Xia, Y.; Qin, M.; Cao, Y.; Wang, W. A Simple Procedure to Improve the Surface Passivation for Single Molecule Fluorescence Studies. *Phys. Biol.* **2015**, *12* (4), 045006. https://doi.org/10.1088/1478-3975/12/4/045006.

(130) Hua, B.; Han, K. Y.; Zhou, R.; Kim, H.; Shi, X.; Abeysirigunawardena, S. C.; Jain, A.; Singh, D.; Aggarwal, V.; Woodson, S. A.; Ha, T. An Improved Surface Passivation Method for Single-Molecule Studies. *Nat. Methods* **2014**, *11* (12), 1233–1236. https://doi.org/10.1038/nmeth.3143.

(131) Green, M. R.; Sambrook, J. Precipitation of DNA with Ethanol. *Cold Spring Harb. Protoc.* **2016**, *2016* (12), pdb.prot093377. https://doi.org/10.1101/pdb.prot093377.

(132) Manzo, C.; Garcia-Parajo, M. F. A Review of Progress in Single Particle Tracking: From Methods to Biophysical Insights. *Rep. Prog. Phys.* **2015**, *78* (12), 124601. https://doi.org/10.1088/0034-4885/78/12/124601.

(133) Cheezum, M. K.; Walker, W. F.; Guilford, W. H. Quantitative Comparison of Algorithms for Tracking Single Fluorescent Particles. *Biophys. J.* **2001**, *81* (4), 2378–2388. https://doi.org/10.1016/S0006-3495(01)75884-5.

(134) Zhang, B.; Zerubia, J.; Olivo-Marin, J.-C. Gaussian Approximations of Fluorescence Microscope Point-Spread Function Models. *Appl. Opt.* **2007**, *46* (10), 1819–1829. https://doi.org/10.1364/AO.46.001819.

(135) Nakhmani, A.; Tannenbaum, A. Particle Filtering Using Multiple Cross-Correlations for Tracking Occluded Objects in Cluttered Scenes. In *2008 47th IEEE Conference on Decision and Control*; 2008; pp 652–657. https://doi.org/10.1109/CDC.2008.4738656.

(136) Robbins, A.; Hildebolt, H.; Neuhoff, M.; Beshay, P.; Winter, J. O.; Castro, C. E.; Bundschuh, R.; Poirier, M. G. Cooperative Control of a DNA Origami Force Sensor. *Sci. Rep.* **2024**, *14* (1), 4132. https://doi.org/10.1038/s41598-024-53841-3.

(137) Robbins, A. Cooperative Control of a DNA Origami Force Sensor. Doctoral dissertation, The Ohio State University, 2023.

(138) Shen, H.; Tauzin, L. J.; Baiyasi, R.; Wang, W.; Moringo, N.; Shuang, B.; Landes, C. F. Single Particle Tracking: From Theory to Biophysical Applications. *Chem. Rev.* **2017**, *117* (11), 7331–7376. https://doi.org/10.1021/acs.chemrev.6b00815.

(139) Chenouard, N.; Smal, I.; de Chaumont, F.; Maška, M.; Sbalzarini, I. F.; Gong, Y.; Cardinale, J.; Carthel, C.; Coraluppi, S.; Winter, M.; Cohen, A. R.; Godinez, W. J.; Rohr, K.; Kalaidzidis, Y.; Liang, L.; Duncan, J.; Shen, H.; Xu, Y.; Magnusson, K. E. G.; Jaldén, J.; Blau, H. M.; Paul-Gilloteaux, P.; Roudot, P.; Kervrann, C.; Waharte, F.; Tinevez, J.-Y.; Shorte, S. L.; Willemse, J.; Celler, K.; van Wezel, G. P.; Dan, H.-W.; Tsai, Y.-S.; de Solórzano, C. O.; Olivo-Marin, J.-C.; Meijering, E. Objective Comparison of Particle Tracking Methods. *Nat. Methods* **2014**, *11* (3), 281–289. https://doi.org/10.1038/nmeth.2808.

(140) Berglund, A. J.; McMahon, M. D.; McClelland, J. J.; Liddle, J. A. Fast, Bias-Free Algorithm for Tracking Single Particles with Variable Size and Shape. *Opt. Express* **2008**, *16* (18), 14064–14075. https://doi.org/10.1364/OE.16.014064.

(141) Andersson, S. B. Localization of a Fluorescent Source without Numerical Fitting. *Opt. Express* **2008**, *16* (23), 18714–18724. https://doi.org/10.1364/OE.16.018714.

(142) Hedde, P. N.; Fuchs, J.; Oswald, F.; Wiedenmann, J.; Nienhaus, G. U. Online Image Analysis Software for Photoactivation Localization Microscopy. *Nat. Methods* **2009**, *6* (10), 689–690. https://doi.org/10.1038/nmeth1009-689.

(143) Small, A.; Stahlheber, S. Fluorophore Localization Algorithms for Super-Resolution Microscopy. *Nat. Methods* **2014**, *11* (3), 267–279. https://doi.org/10.1038/nmeth.2844.

(144) Abraham, A. V.; Ram, S.; Chao, J.; Ward, E. S.; Ober, R. J. Quantitative Study of Single Molecule Location Estimation Techniques. *Opt. Express* **2009**, *17* (26), 23352–23373. https://doi.org/10.1364/OE.17.023352.

(145) Horst, A. van der; Forde, N. R. Calibration of Dynamic Holographic Optical Tweezers for Force Measurements on Biomaterials. *Opt. Express* **2008**, *16* (25), 20987–21003. https://doi.org/10.1364/OE.16.020987.

(146) Nehme, E.; Weiss, L. E.; Michaeli, T.; Shechtman, Y. Deep-STORM: Super-Resolution Single-Molecule Microscopy by Deep Learning. *Optica* **2018**, *5* (4), 458–464. https://doi.org/10.1364/OPTICA.5.000458.

(147) Antun, V.; Renna, F.; Poon, C.; Adcock, B.; Hansen, A. C. On Instabilities of Deep Learning in Image Reconstruction and the Potential Costs of AI. *Proc. Natl. Acad. Sci.* **2020**, *117* (48), 30088–30095. https://doi.org/10.1073/pnas.1907377117.

(148) Lansdorp, B. M.; Tabrizi, S. J.; Dittmore, A.; Saleh, O. A. A High-Speed Magnetic Tweezer beyond 10,000 Frames per Second. *Rev. Sci. Instrum.* **2013**, *84* (4), 044301. https://doi.org/10.1063/1.4802678.

(149) Lansdorp, B. M.; Saleh, O. A. Power Spectrum and Allan Variance Methods for Calibrating Single-Molecule Video-Tracking Instruments. *Rev. Sci. Instrum.* **2012**, *83* (2), 025115. https://doi.org/10.1063/1.3687431.

(150) Huhle, A.; Klaue, D.; Brutzer, H.; Daldrop, P.; Joo, S.; Otto, O.; Keyser, U. F.; Seidel, R. Camera-Based Three-Dimensional Real-Time Particle Tracking at kHz Rates and Ångström Accuracy. *Nat. Commun.* **2015**, *6* (1), 5885. https://doi.org/10.1038/ncomms6885.

(151) Czerwinski, F.; Richardson, A. C.; Oddershede, L. B. Quantifying Noise in Optical Tweezers by Allan Variance. *Opt. Express* **2009**, *17* (15), 13255–13269. https://doi.org/10.1364/OE.17.013255.

(152) Lesage, P.; Audoin, C. Characterization and Measurement of Time and Frequency Stability. *Radio Sci.* **1979**, *14* (4), 521–539. https://doi.org/10.1029/RS014i004p00521.

(153) Andersson, M.; Czerwinski, F.; Oddershede, L. B. Optimizing Active and Passive Calibration of Optical Tweezers. *J. Opt.* **2011**, *13* (4), 044020. https://doi.org/10.1088/2040-8978/13/4/044020.

(154) Lansdorp, B. M. Pushing the Envelope of Magnetic Tweezer Resolution, UC Santa Barbara, 2015. https://escholarship.org/uc/item/0g27w21k (accessed 2024-10-03).

(155) Welch, P. The Use of Fast Fourier Transform for the Estimation of Power Spectra: A Method Based on Time Averaging over Short, Modified Periodograms. *IEEE Trans. Audio Electroacoustics* **1967**, *15* (2), 70–73. https://doi.org/10.1109/TAU.1967.1161901.

(156) Gibson, G. M.; Leach, J.; Keen, S.; Wright, A. J.; Padgett, M. J. Measuring the Accuracy of Particle Position and Force in Optical Tweezers Using High-Speed Video Microscopy. *Opt. Express Vol 16 Issue 19 Pp 14561-14570* **2008**. https://doi.org/10.1364/OE.16.014561.

(157) Otto, O.; Czerwinski, F.; Gornall, J. L.; Stober, G.; Oddershede, L. B.; Seidel, R.; Keyser, U. F. Real-Time Particle Tracking at 10,000 Fps Using Optical Fiber Illumination. *Opt. Express* **2010**, *18* (22), 22722–22733. https://doi.org/10.1364/OE.18.022722.

(158) Schäffer, E.; Nørrelykke, S. F.; Howard, J. Surface Forces and Drag Coefficients of Microspheres near a Plane Surface Measured with Optical Tweezers. *Langmuir* **2007**, *23* (7), 3654–3665. https://doi.org/10.1021/la0622368.

(159) Downing, B. P. B. *Probing the mechanical properties of short molecules with optical tweezers*. https://summit.sfu.ca/item/10057 (accessed 2024-10-17).

(160) Lee, S.-H.; Roichman, Y.; Yi, G.-R.; Kim, S.-H.; Yang, S.-M.; Blaaderen, A. van; Oostrum, P. van; Grier, D. G. Characterizing and Tracking Single Colloidal Particles with Video Holographic Microscopy. *Opt. Express* **2007**, *15* (26), 18275–18282. https://doi.org/10.1364/OE.15.018275.

(161) Brouwer, T. B.; Hermans, N.; Noort, J. van. Multiplexed Nanometric 3D Tracking of Microbeads Using an FFT-Phasor Algorithm. *Biophys. J.* **2020**, *118* (9), 2245–2257. https://doi.org/10.1016/j.bpj.2020.01.015.

(162) Cnossen, J. P.; Dulin, D.; Dekker, N. H. An Optimized Software Framework for Real-Time, High-Throughput Tracking of Spherical Beads. *Rev. Sci. Instrum.* **2014**, *85* (10), 103712. https://doi.org/10.1063/1.4898178.

(163) Gosse, C.; Croquette, V. Magnetic Tweezers: Micromanipulation and Force Measurement at the Molecular Level. *Biophys. J.* **2002**, *82* (6), 3314–3329. https://doi.org/10.1016/S0006-3495(02)75672-5.

(164) van Loenhout, M. T. J.; Kerssemakers, J. W. J.; De Vlaminck, I.; Dekker, C. Non-Bias-Limited Tracking of Spherical Particles, Enabling Nanometer Resolution at Low Magnification. *Biophys. J.* **2012**, *102* (10), 2362–2371. https://doi.org/10.1016/j.bpj.2012.03.073.

(165) Carlucci, L. A.; Thomas, W. E. Modification to Axial Tracking for Mobile Magnetic Microspheres. *Biophys. Rep.* **2021**, *1* (2), 100031. https://doi.org/10.1016/j.bpr.2021.100031.

(166) Dulin, D.; Cui, T. J.; Cnossen, J.; Docter, M. W.; Lipfert, J.; Dekker, N. H. High Spatiotemporal-Resolution Magnetic Tweezers: Calibration and Applications for DNA Dynamics. *Biophys. J.* **2015**, *109* (10), 2113–2125. https://doi.org/10.1016/j.bpj.2015.10.018.

(167) Vermeulen, K. C.; Wuite, G. J. L.; Stienen, G. J. M.; Schmidt, C. F. Optical Trap Stiffness in the Presence and Absence of Spherical Aberrations. *Appl. Opt.* **2006**, *45* (8), 1812–1819. https://doi.org/10.1364/AO.45.001812.

(168) Neuman, K. C.; Abbondanzieri, E. A.; Block, S. M. Measurement of the Effective Focal Shift in an Optical Trap. *Opt. Lett.* **2005**, *30* (11), 1318–1320. https://doi.org/10.1364/OL.30.001318.

(169) Yang, Y.; Wang, W.; Peng, C.; Lei, W.; Deng, Z. Optimization of Nd-Fe-B Permanent Magnet Guideways with High-Temperature Stability. *J. Magn. Magn. Mater.* **2024**, *604*, 172290. https://doi.org/10.1016/j.jmmm.2024.172290.

(170) Desjardins, P.; Conklin, D. NanoDrop Microvolume Quantitation of Nucleic Acids. *JoVE J. Vis. Exp.* **2010**, No. 45, e2565. https://doi.org/10.3791/2565.

(171) *UV absorbance DNA quantitation | BMG LABTECH*. https://www.bmglabtech.com/en/application-notes/uv-absorbance-dna-quantitation/ (accessed 2024-07-15).

Appendix A.

Table of components

Component	Function	Specifications
N52 Neodymium magnets	Generate the magnetic fields to apply forces on magnetic beads	Size: 8mm x 5mm x 3mm Remanence magnetization: 14.3 – 14.8 kG Coercivity (Hc) ≥ 10.5 kOe.
Stepper Motor (MCL-µS2544)	Controls the height of the magnet holder	Controller: Micro-Drive® 95 nm step size 50 mm range 50 nm encoder resolution 2 mm/s maximum speed
Quad-band optical component (Chroma, ZT 405/488/561/640 rpcv2-uf2)	Reflects light in the narrow band gaps of the four laser lines, while transmitting outside these bands.	Quad-band optical component (Chroma)
LED Light Source	Provides illumination for MT	Wavelength: 780 nm Power: 300 mW
Fluorescence Camera Hamamatsu ORCA-Fusion BT C12440-20UP.	Captures fluorescence images from TIRF microscopy	CMOS 16-bit Speed: 50 fps Resolution: 2304x2304 px^2 Pixel size: 6.5 µm x 6.5 µm
MT Camera Basler acA1440-220um	Captures field of view including bead diffraction patterns for MT	CMOS Speed: 227 fps Resolution: 1.6 MP Pixel size: 3.45 µm x 3.45 µm
Converging lenses	Used for illumination of the sample and collection of light from the sample	Focusing lenses: f=150 mm f=76 mm f=25 mm f=50 mm f=100 nm
Piezo Stage (MCL)	Provides nanometer-scale positioning for sample manipulation	Controller: Nano-Drive® X,Y,Z axis movement Resolution: 0.4 nm Range: 200 µm
Micro Stage (MCL-µS2542)	Provides micrometer-scale positioning for sample manipulation	Controller: Micro-Drive® X,Y movement Step size: 95 nm Range: 25 mm
Rotational Stage (MCL-µS2545)	Allows 360° rotation of the magnets	Controller: Mad360™ Step size: 1 milliradian Angular velocity ≤ 1 rotation/s

Quadrant Photodiode (QPD) (Thorlabs, SM2CP2)	Provides feedback for adjusting the incident angle in TIRF microscopy	Controler: Mad City Labs TIRF-Lock™ Wavelength range: 350 nm – 1100 nm Sensor size: 4.98 mm diameter, quadrants with 30 µm gaps
Dichroic Mirror Chroma ZT775sp-2p	Separates long and short-wavelength light for fluorescence and MT detection	Short-pass at 775 nm
Bandpass Filter	Ensures monochromatic light for MT detection	Passes 775 nm ± 25 nm
Illuminator Controller	Controls the intensity of the LED light source	Adjustable brightness, 12V/3.0A
Objective lens Olympus UPLAPO60XOHR	Collects the light from the sample	Magnification: 60X Numerical aperture: 1.5 NA Immersion medium: Oil Back focal plane: -25.0 mm

Appendix B.

Preparation of hydrophobic glass.

This procedure is an adaptation from Kirkness et al.[126]. The glass coverslips are made of borosilicate glass (VWR: 48393 106) and the glass microscope slides are made of sodium lime glass (UltiDent Scientific: 170-7107-AS).

B.1. Glass cleaning

Starting at the wet lab:

- Place microscope slides and coverslips into the glass holder as shown in Figure B-1.
- Rinse a 1.5 L beaker with deionized (ddH_2O) water. After rinsing twice, fill the beaker with Milli-Q (18 MΩ) water.
- Place the holder with the microscope slides and coverslips inside the beaker.
- Rinse with the microscope slides and coverslips holder inside by pulling the holder up and down 3 to 4 times.
- Fill the beaker containing the holder with Mili-Q water and microwave for around 10 minutes (water should be boiling for 2-3 minutes).
- Rinse the contents again by pulling the holder up and down 3 to 4 times. You should not add any additional water. (You can cool it down by pouring water on the outside of the beaker.)
- Fill a large beaker (5L) with ddH_2O water and transport to the chemical preparation room.

Figure B-1 Microscope slide and coverslip holder.
The microscope slides are placed in the holder with slits while the coverslips are placed inside the glass cylinders. The whole holder could fit in a 1.5 L break to facilitate the rinsing.

Move to the chemical preparation room to work inside the fume hood:

Note: every time you rinse the holder with the slides, pull it up and down 3-4 times in the old solution before transferring to the new holder.

- Transfer the holder to the 1.5 L beaker designated for HCl and methanol.
- Put on the proper acid-resistant globes (black gloves).
- Fill the beaker with a 1:1 HCl:methanol mixture. The purpose of the HCl is to remove organic residue; the purpose of methanol is to remove polar contaminants.
- Sonicate for 45 minutes at room temperature.
- Place the holder in another beaker and pour the HCl:methanol mixture back into its storage bottle. (It can be reused a maximum of three times).

- Rinse the holder 4 times in a different 1.5 L beaker filled with distilled water from the 5L beaker. (Don't pour the water directly onto the slides.) The first 2 times discard the water into the designated waste bottles. The last 2 times the water can be discarded down the drain.
- After the 4th rinse, place the holder in a 1.5 L beaker filled with fresh Milli-Q water and sonicate for 5 minutes.
- While this is happening, clean all beakers by rinsing them with ddH_2O water.
- Get rid of most of the water on the slide/coverslip holder by letting it drip before placing it in the 1.5 L beaker designated for H_2SO_4 (sulfuric acid).
- Fill the beaker with H_2SO_4. (This activates the hydroxyl groups on the glass for silanization.)
- Sonicate for 45 minutes at room temperature.
- Place the holder in another beaker and place the sulfuric acid in the proper storage bottle. (It can also be reused a maximum of 3 times.)
- Rinse the holder 4 times in the 1.5 L beaker filled with distilled water from the 5 L beaker. (Don't pour the water directly onto the slides.) The first 2 times discard the water into the designated waste bottles. The last 2 times the water can be discarded down the drain.
- After the 4th rinse, place the holder in a 1.5 L beaker filled with fresh Milli-Q water and sonicate for 5 minutes.
- While this is happening, clean all beakers with distilled water by rinsing them.
- Bring the hot plate to the chem prep room, place inside the fume hood and cover it with new (clean) aluminum foil.
- Dry the slides using filtered air (there is an air outlet at one side of the fume hood) and then place them on the hot plate (covered in aluminum foil) at a low temperature (around 100°, level 1 on the old hotplate) for 5 minutes.

B.2. Hydrophobic surface preparation

These steps should be performed immediately after the acid cleaning and the glass slides have cooled down – to get better results do not wait until the next day. Sigmacote is stored at 4°C and can be reused until it stops smelling or the contact angle gets reduced. Use the small breakers previously designated for Sigmacote or ethanol.

- Rinse the beakers with ddH_2O water if they do not look clean.
- Submerge the cover glass or microscope slides in Sigmacote for 90 seconds inside a small beaker.
- Take each slide out of the Sigmacote and submerge it in ethanol for 90 seconds.
- Dry the slides with filtered air and then place them for 30 minutes on a hot plate (around 100^{o}C, level 1 on the old hotplate).
- Discard the waste into its respective waste bottle and wash the beakers with ddH_2O water.

B.2.1. Assembly of chambers

Note: This step does not have to be taken immediately after the hydrophobic surface is created. A schematic of how to fabricate the chambers is shown in Figure B-2.

- Attach double-sided tape to the microscope slide. This could be done with one layer of double-sided tape or with two layers of double-sided tape. For approach B, it is better to use two layers because it's easier to flow in the biotinylated BSA.
- Remove the other layer of backing on the tape and position the coverslip on top of it. Press carefully on the sides to make sure that the double-sided tape is sealing the chamber properly.

These chambers can now be used to flow liquids inside. When a fluid exchange is necessary, tilt the chamber slightly so that the old liquid exits from the lower side while the new liquid enters from the higher side. Once the desired contents for the experiment are in the sample chamber, it is sealed by adding melted paraffin wax over the openings. It is better to keep the coverslip facing down when the wax is added or do it as quickly as possible to get the least of beads interacting with the microscope slide before flipping.

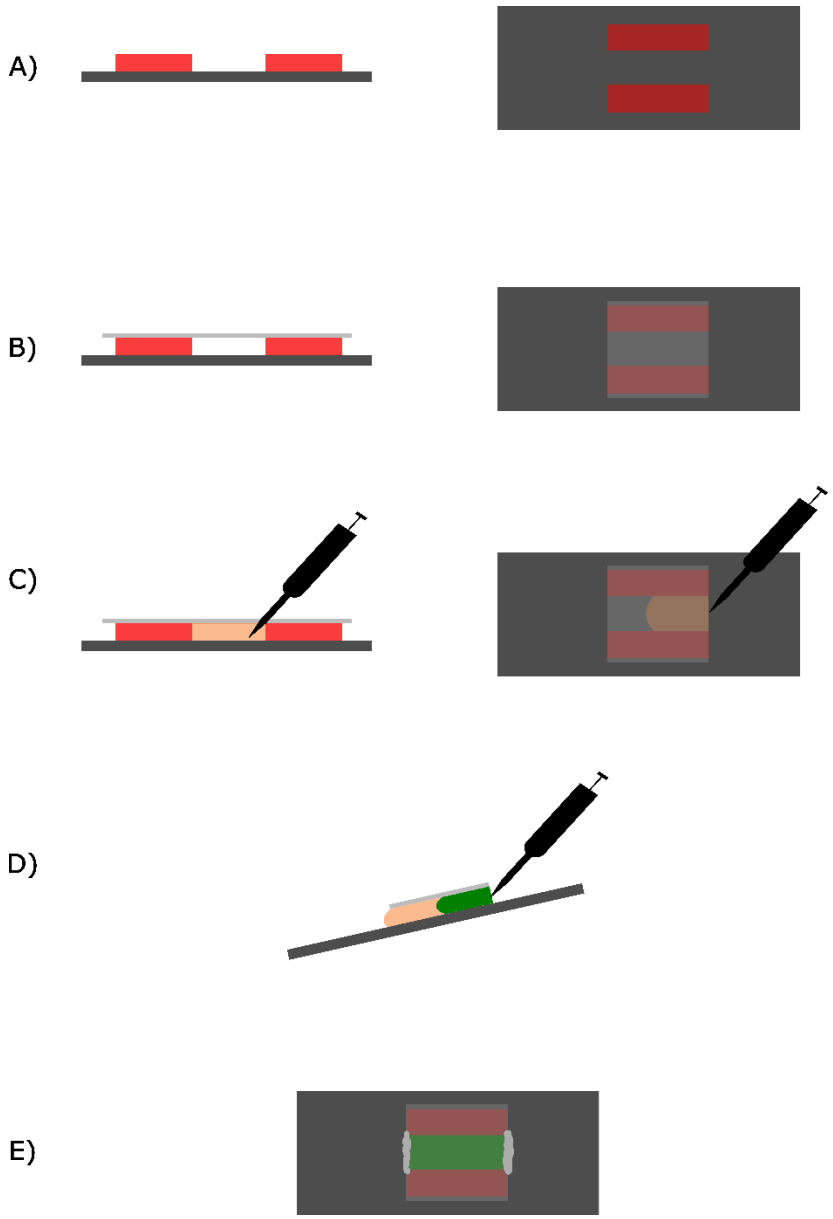

Figure B-2 Sample chamber fabrication.
This image illustrates the procedure for building and using the sample chamber. A) Two pieces of double-sided tape are placed on the microscope slide, which is then B) sealed with a coverslip. C) The chamber is filled using a pipette. D) Liquid is exchanged for different parts of the tethering process by tilting the chamber and pipetting on the high side. E) The chamber is sealed with wax.

Appendix C.

Tethering Protocol

This protocol outlines the procedures for both approaches A (DNA with a thiol at one end and a biotin at the opposite end) and B (DNA with a thiol at one end and an amine group at the opposite end). DNA is tethered between an amine bead and a functionalized glass slide. It is an adaptation from the protocols described in [42,126].

C.1. Materials needed:

- F127-NHS (only for approach A)
- F127 or Tween 20 (only for approach B)
- Sodium phosphate buffer 0.1 M (pH 6.0)
- Sodium phosphate buffer 0.1 M (pH 8.0)
- Magnetic amine beads (Dynabeads M-270 amine, $2x10^9$ beads/mL)
- Succinimidyl 3-(2-pyridyldithio)propionate (SPDP), 50 mM in DMSO.
- SPDP buffer pH 7.8 (100 mM sodium phosphate dibasic, 150 mM NaCl, 1 mM ethylenediaminetetraacetic acid)
- SPDP buffer pH 7.4
- SPDP buffer pH 8.4
- Succinic anhydride (SA), 50 mM in DMSO
- DNA with thiol and amine group at the ends (only for approach A; see Appendix B)
- DNA with thiol and biotin at the ends (only for approach B; see Appendix B)
- TCEP-HCl or TCEP gel
- Hydrophobic chambers (see Appendix B)

Note: the SA and SPDP must be disolved in DMSO 50mM (at 50x concentration)

C.2. Procedure:

Note: only the surface coating part of the procedure is different for the two approaches.

C.2.1. Microsphere coating:

- Wash 50 µL of microspheres 3 times with 1 mL of SPDP buffer pH 7.8. The final volume must be 490 µL, so on the last wash remove the volume necessary to have 490 µL remaining. Spheres can be pelleted for buffer exchange using a magnet.

- Add 10 µL of 50 mM SA in DMSO (50X) to the 490 mL solution of beads in SPDP buffer. Leave it for 30 min with continuous mixing at room temperature in a tube rotator.
- Wash 3 times with 1 mL of SPDP buffer pH 8.4, leaving a final volume of 490 µL.
- Add 10 µL of 50 mM SPDP diluted in DMSO (50X) to the 490 mL of beads in SPDP buffer. Follow this with 2h of continuous mixing at room temperature.

Note: as per Kirkness et al.[126], the reaction could be done only with SPDP. But, to reduce non-specific binding, both steps (SA and SPDP) should be done.

C.2.2. DNA reduction (activation of the thiol groups):

- Wash the TCEP gel with the SPDP buffer pH 7.4 three times. Do it by centrifuging the tube and replacing the supernatant. The volume should be approximately twice the DNA sample volume.
- Add the DNA and allow it to react for 1h with continuous mixing.
- Centrifuge the gel and remove the supernatant containing the DNA.
- Add the DNA to the microspheres and leave them to mix overnight at room temperature.

The ratio of DNA:beads should be 100 000:1 according to [126]; however, we tried also with one order of magnitude higher concentration and up to two orders of magnitude lower concentration. The beads should be diluted around 100 to 1000 times from the stock concentration ($2x10^9$ beads/mL) by adding SPDP buffer pH 7.4.

After the DNA is bound, all the microspheres are washed in 1 mL of 0.1 M Sodium Phosphate buffer pH 8.0, which is the buffer used for further assays (e.g. MAGIC assay or pulling with MT).

Note: The TCEP gel approach did not work for other laboratory members when reducing disulfide bonds. Alternatively, TCEP-HCl with a different procedure could be used. It's also important to note that TCEP is not particularly stable in phosphate buffers according to the provider's (ThermoScientific) manual. I am not including the protocol to use TCEP-HCl because I also did not get good tethering results when using it.

C.2.3. Surface coating:

A series of incubations must be done within a hydrophobic chamber assembled and used as shown in Figure B.2. For both approaches, wash the chambers between steps

with about three times the volume of the chamber using 0.1 M of sodium phosphate buffer pH 8.0.

C.2.4. Approach A:

- Add 0.5 mg/ml of biotinylated BSA in 0.1 M sodium phosphate buffer pH 8.0 until the chamber is filled [30 to 60 µl depending on the chamber size], then incubate for 10 minutes.
- Add the same volume (to fill the chamber) of 0.2% Tween-20 and incubate for 10 minutes. (This could be substituted by incubation with F127).
- Add the same volume of 0.5 mg/ml of streptavidin in 0.1 M sodium phosphate buffer pH 8.0 and incubate for 5 minutes.
- Wash with 3 times the chamber volume of 0.1 M sodium phosphate buffer pH 8.0.

C.2.5. Approach B:

- Add 10 mg/ml of F127-NHS in 0.1M sodium phospate buffer pH 6.0 until the chamber is filled [30 to 60 µl depending on the chamber size], then incubate in the fridge (4°C) for 4 h inside a humidity chamber. (The humidity chamber is made by putting wet paper towels in an enclosed Petri dish or a tip box.)
- Wash with 10 times the chamber volume of 0.1 M sodium phosphate buffer pH 8.0, then wait for 20 minutes before adding beads and DNA.

For both approaches, add the magnetic beads with DNA to the chamber, then seal the chamber with wax. It is important to minimize the time that the microscope slide is facing down; this could be done by sealing the chamber from below and maintaining the coverslip facing down.

Then let the beads settle on the coverslip for about 20 minutes.

Finish by doing a MAGIC (microsphere adhesion by gravity, inversion, then counting) assay test as described in[126].

Appendix D.

MAGIC assay details and results

In this appendix, I describe how the counting of the beads was performed and show some of the results for different samples.

D.1. Counting Algorithm:

The algorithm used to do the counting was developed in Python by lab member Koushik Bar, using mainly the libraries Scikit-image© and OpenCV©. The basic steps are: Import the image, flatten the image using a rolling-ball background correction, make the image binary using yen's algorithm, identify the objects, get the distribution of sizes, choose the population that represents individual beads, and count the number of objects in that population.

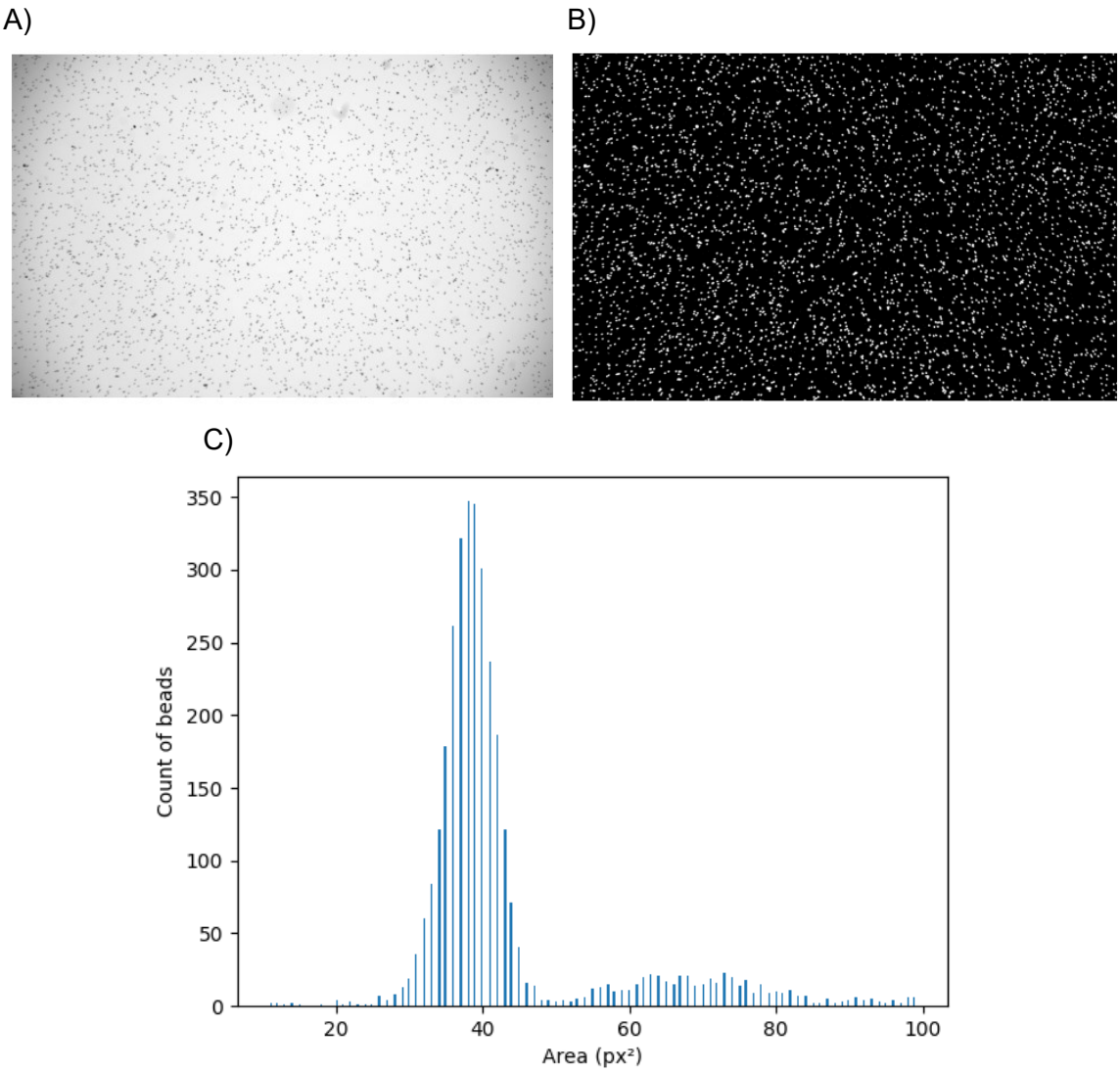

Figure D-1 Bead size distribution.
A) The original bright-field image obtained using an Olympus IX83 microscope with 10X magnification. B) The filtered and binary image of the beads resulting from image processing in Python. C) Distribution of object size has a peak around 38 pixels squared (px^2) representing the size of individual beads. The field of view is approximately 1.8 mm x 1.1 mm.

D.2. Counting Results:

After counting the beads on the top surface (coverslip) and on the bottom surface (glass slide) after flipping the sample chamber and allowing unbound beads to settle to the bottom, I count the percentage remaining on the top. The next results are presented as the percentage of beads remaining on top after flipping, with error bars representing the standard deviation among different imaged regions of a sample chamber.

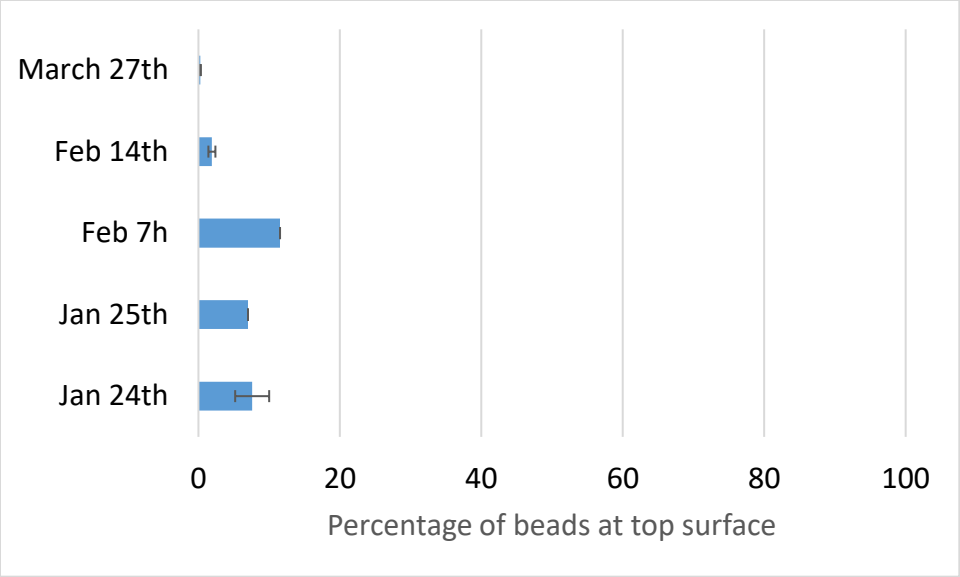

Figure D-2 Testing two SA+SA treatments of beads.
This graph shows the results for different experiments where the beads were treated twice with SA. Dates refer to 2023 measurements described in my lab notebook. Jan 25th and Feb 7th have only one image of the top surface and one image of the bottom surface, Jan 24th has two images of each surface, Feb 14th has three images of each surface and March 4th has four images of each surface. The results show that SA+SA treatment results in very little nonspecific binding of beads to the surface.

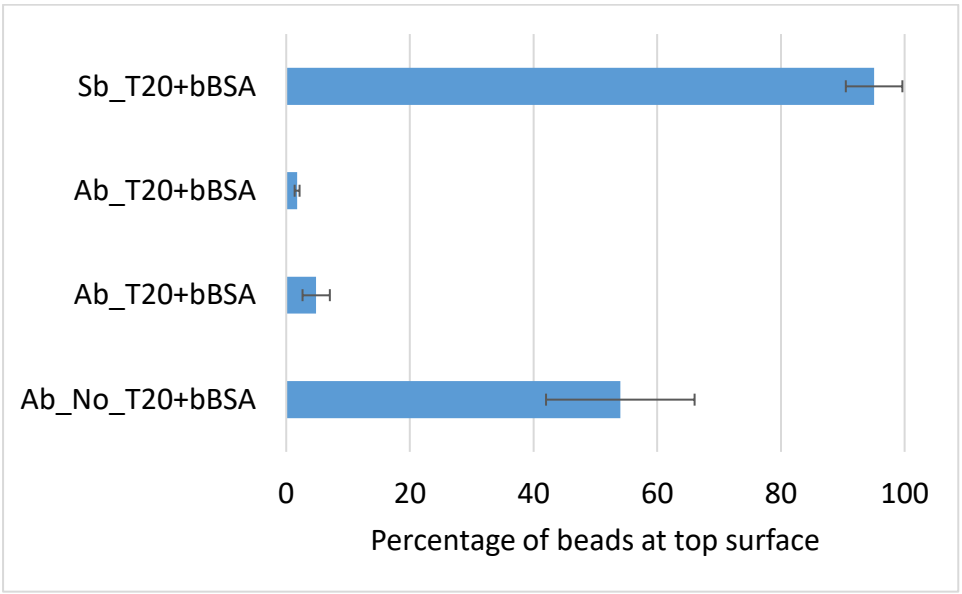

Figure D-3 Testing surface treatment with Tween20 + biotinylated BSA.
Ab mean amine beads, Sb means Streptavidin beads, T20+bBSA means that the glass surface was treated with Tween 20 and biotinylated BSA, No_T20+bBSA means that there was no treatment with Tween 20 nor biotinylated BSA. Four images of the top and bottom surfaces were taken for each condition. These results show that amine beads are blocked from binding nonspecifically by the presence of Tween 20 and BSA, and that streptavidin beads bind strongly to this surface.

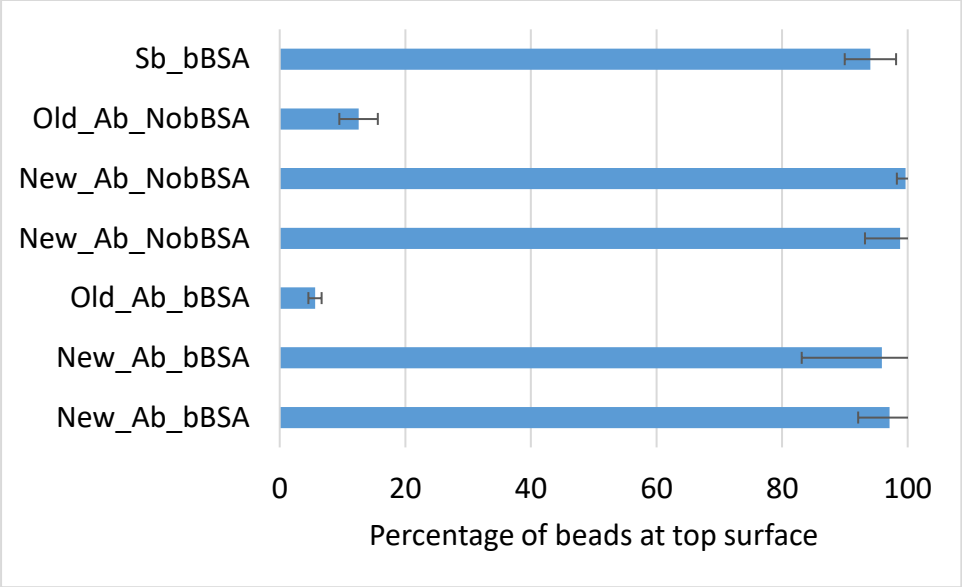

Figure D-4 Testing surface treatment with F127 + biotinylated BSA.
These sample chambers all had an F127 surface treatment. Old_Ab means the old batch of amine beads, New_Ab means the new batch of amine beads, and Sb means Streptavidin beads. bBSA means that the glass surface was treated with biotinylated BSA and NobBSA means that the sample was not treated with biotinylated BSA. Here I concluded that it's better to continue using the Old beads (Dynabeads M127®) because of their lower nonspecific binding. Four images of the top and bottom surfaces were taken for each condition.

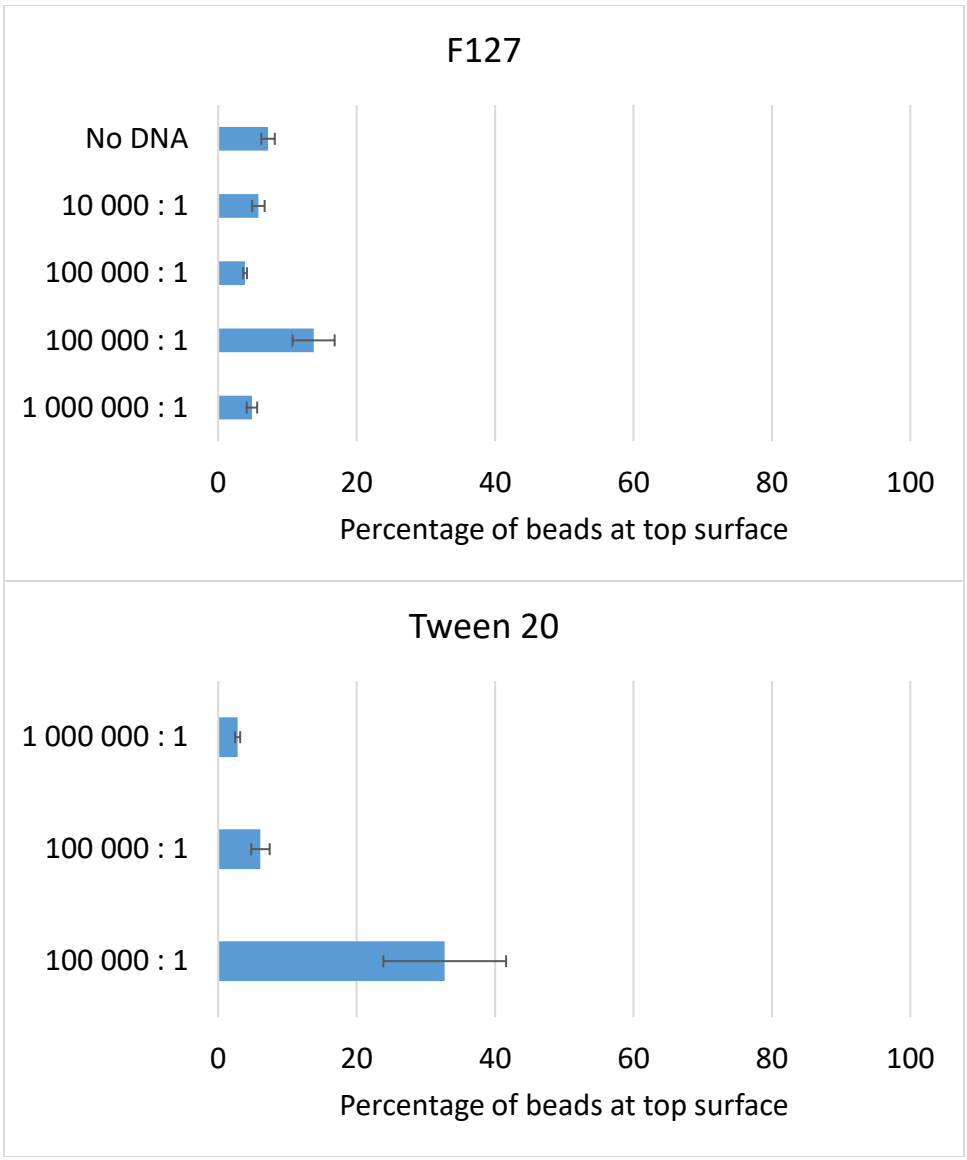

Figure D-5 Testing Approach B with DNA.
To passivate the glass surface I used F127 (Top), and Tween 20 (bottom). Surfaces also included biotinylated BSA, as outlined in Appendix C. Two images of the bottom surface and five of the top surface were taken for each of these two experiments. The results show that for neither of the passivation methods I got what I expected which is more binding as the concentration of DNA:bead is increased.

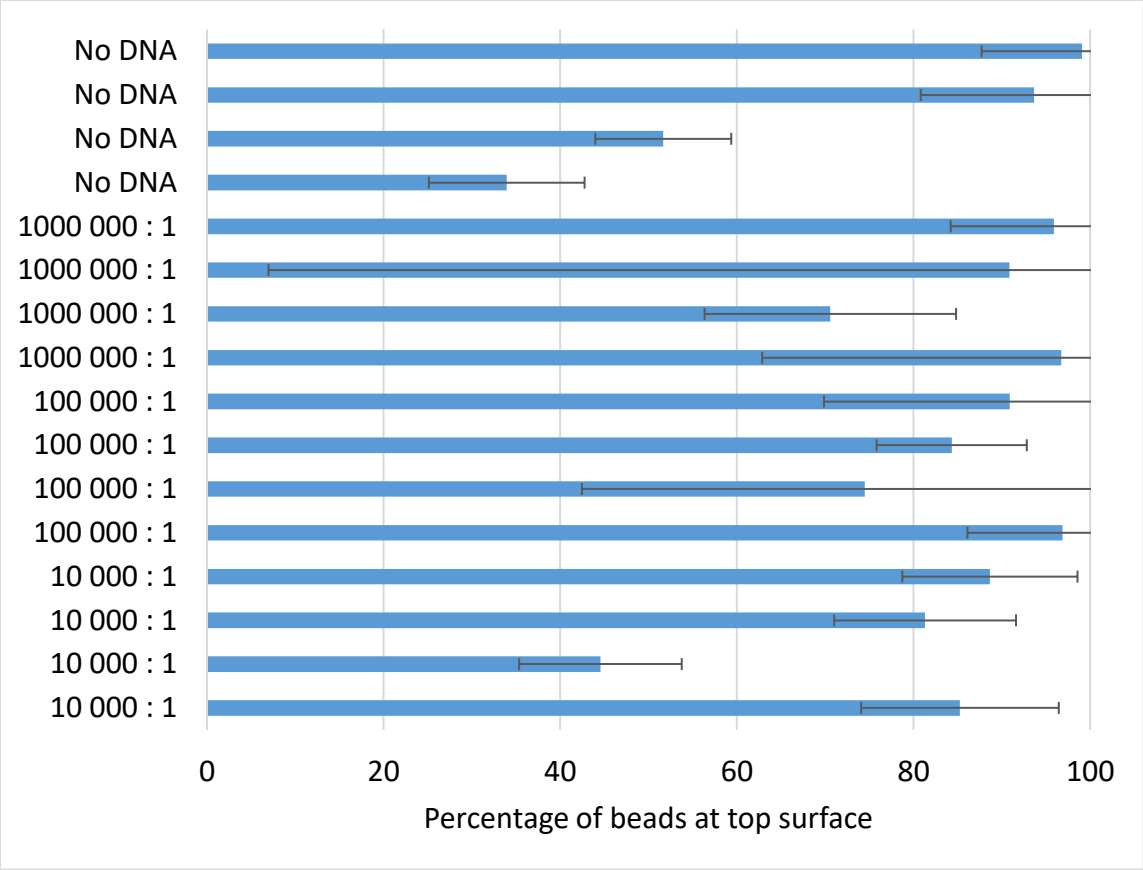

Figure D-6 Testing Approach B with DNA using Tween 20 to passivate the glass surface.

Here, 3 different DNA:bead concentration ratios were contrasted with a sample without DNA. Five images of each surface were taken for each sample chamber (separate line) in this experiment. These results indicate that for approach B I did not get what I expected which is more binding as the concentration of DNA:bead is increased.

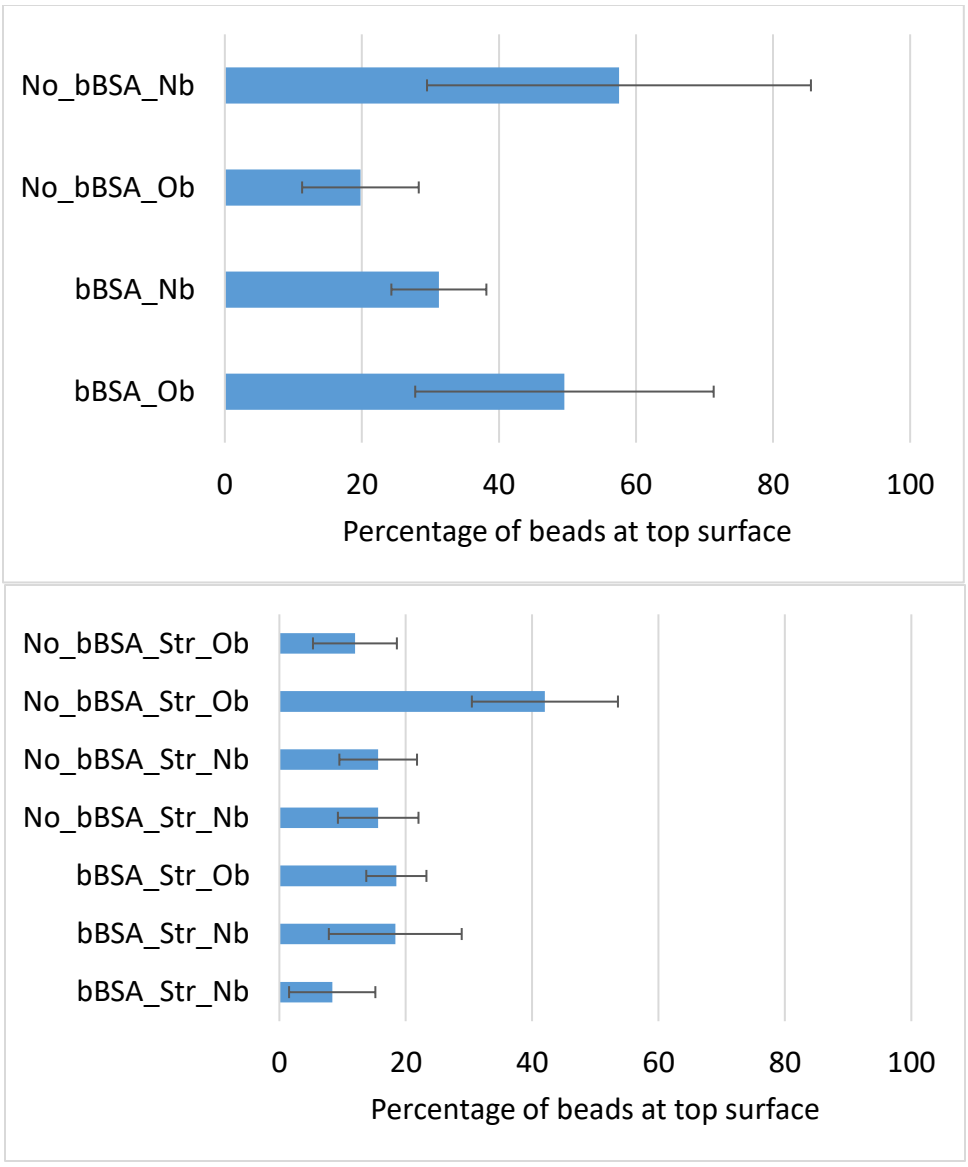

Figure D-7 Testing the non-specific binding induced by DNA incubation steps on DNA-free samples.

All these experiments used Tween 20 on the surface, some used biotinylated BSA (bBSA) and/or streptavidin (Str) or neither (No). These data also compare an old batch of Dynabeads (Ob) with a newly acquired batch of Dynabeads (Nb). This was designed to test if the bBSA, the streptavidin or the old beads influenced the non-specific binding. Five images of the top and bottom surfaces of each sample chamber (separate line) were taken for these experiments. These results indicate that neither the biotinylated BSA nor the streptavidin is causing the issue with the non-specific binding of the beads.

Appendix E.

DNA information

In this appendix, I describe and characterize the DNA used in the tethering experiments.

E.1. DNA Handles Approach A:

DNA was produced using PCR, amplifying a region of the pUC-19 plasmid replicating previous procedures [126]. The result of the PCR reaction is a 996 bp double-stranded DNA, the primers used are:

5′-[Amino C6][Spacer 18] TGT CTT AGA TCT TTT GGA GCG AAC GAC-3′ (BioSynthesis; Spacer 18 is a 6-PEG oligomer)

5′[Thio-Mod C6 S−S] TTG CTT GAT ATC TTG TAC TGA GAG TGC ACC-3′ (BioSynthesis).

E.2. DNA Handles Approach B:

DNA was produced using PCR, amplifying a region of the pUC-19 plasmid. The result of the PCR reaction is a 2075 bp double stranded DNA. Its sequence (5’ to 3’ of one strand) is: from Derek’s Dee lab at UBC

cgtcgtgactgggaaaaccctggcgttacccaacttaatcgccttgcagcacatccccctttcgccagctggcgtaatagcg
aagaggcccgcaccgatcgcccttcccaacagttgcgcagcctgaatggcgaatggcgcctgatgcggtattttctccttac
gcatctgtgcggtatttcacaccgcatatggtgcactctcagtacaatctgctctgatgccgcatagttaagccagccccgac
acccgccaacacccgctgacgcgccctgacgggcttgtctgctcccggcatccgcttacagacaagctgtgaccgtctccg
ggagctgcatgtgtcagaggttttcaccgtcatcaccgaaacgcgcgagacgaaagggcctcgtgatacgcctatttttata
ggttaatgtcatgataataatggtttcttagacgtcaggtggcacttttcggggaaatgtgcgcggaacccctatttgtttatttttct
aaatacattcaaatatgtatccgctcatgagacaataaccctgataaatgcttcaataatattgaaaaaggaagagtatgag
tattcaacatttccgtgtcgcccttattccctttttgcggcattttgccttcctgtttttgctcacccagaaacgctggtgaaagtaaa
agatgctgaagatcagttgggtgcacgagtgggttacatcgaactggatctcaacagcggtaagatccttgagagttttcgc
cccgaagaacgttttccaatgatgagcacttttaaagttctgctatgtggcgcggtattatcccgtattgacgccgggcaagag

caactcggtcgccgcatacactattctcagaatgacttggttgagtactcaccagtcacagaaaagcatcttacggatggca
tgacagtaagagaattatgcagtgctgccataaccatgagtgataacactgcggccaacttacttctgacaacgatcggag
gaccgaaggagctaaccgcttttttgcacaacatgggggatcatgtaactcgccttgatcgttgggaaccggagctgaatg
aagccataccaaacgacgagcgtgacaccacgatgcctgtagcaatggcaacaacgttgcgcaaactattaactggcg
aactacttactctagcttcccggcaacaattaatagactggatggaggcggataaagttgcaggaccacttctgcgctcggc
ccttccggctggctggtttattgctgataaatctggagccggtgagcgtgggtctcgcggtatcattgcagcactggggccag
atggtaagccctcccgtatcgtagttatctacacgacggggagtcaggcaactatggatgaacgaaatagacagatcgct
gagataggtgcctcactgattaagcattggtaactgtcagaccaagtttactcatatatactttagattgatttaaaacttcatttttt
aatttaaaaggatctaggtgaagatccttttttgataatctcatgaccaaaatcccttaacgtgagttttcgttccactgagcgtca
gaccccgtagaaaagatcaaaggatcttcttgagatcctttttttctgcgcgtaatctgctgcttgcaaacaaaaaaaccacc
gctaccagcggtggtttgtttgccggatcaagagctaccaactctttttccgaaggtaactggcttcagcagagcgcagatac
caaatactgttcttctagtgtagccgtagttaggccaccacttcaagaactctgtagcaccgcctacatacctcgctctgctaat
cctgttaccagtggctgctgccagtggcgataagtcgtgtcttaccgggttggactcaagacgatagttaccggataaggcg
cagcggtcgggctgaacgggggttcgtgcacacagcccagcttggagcgaacgacctacaccgaactgagataccta
cagcgtgagctatgagaaagcgccacgcttcccgaagggagaaaggcggacaggtatccggtaagcggcagggtcg
gaacaggaga

Forward primer: 5'biotin-cgt cgt gac tgg gaa aac cct ggcg

Reverse primer: 5' SH-tct cct gtt ccg acc ctg ccg ctta

E.3. DNA characterization:

Spectroscopy is used to confirm the purity of the DNA sample and to calculate its concentration. Nucleic acids absorb 260 nm of light, proteins absorb around 280 nm, and other organic compound contaminants like phenolate, carbohydrates, and thiocyanate at 230 nm. So, the ratios of the intensities between absorbance at 260 nm and 280 nm ($\frac{I_{260}}{I_{280}}$), and 260 nm and 230 nm ($\frac{I_{260}}{I_{230}}$) give us an idea about the purity of the sample [170,171]. As a rule of thumb, the ratios should be > 1.7 and > 2.0 respectively to consider the sample as pure. Using the Beer-Lambert Law, the concentration can be calculated by measuring the absorbance at 260 nm.

Agarose gel electrophoresis is a widely used technique to separate and visualize DNA fragments based on their size. In this method, DNA samples are loaded into a gel matrix made of agarose and subjected to an electric field. DNA, being negatively

charged, migrates toward the positive electrode, with smaller fragments moving faster through the gel's pores than larger ones. The separated DNA fragments can be visualized under UV light after staining with a DNA-binding dye, allowing for the assessment of DNA size distribution by comparing it with a ladder with known DNA lengths. In our experiments, we used 0.5 g of Agarose in 50 mL of TAE and 125 V.

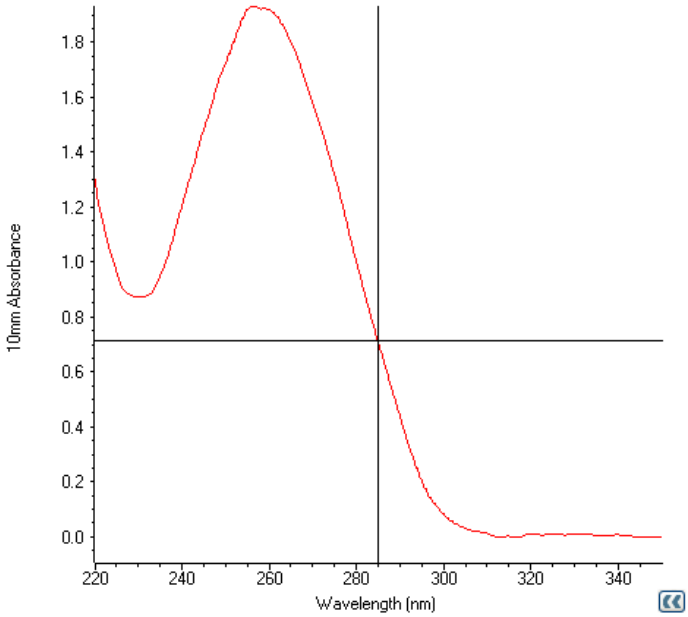

Figure E-1 DNA spectra Approach A.
This graph shows the spectrum for the 1 kbp DNA used in Approach A. For this sample the ratios between the relevant peaks are $\frac{I_{260}}{I_{280}} = 1.91$ and $\frac{I_{260}}{I_{230}} = 2.21$. This spectrum was also used to calculate the DNA concentration using Beer-Lambert law, giving 95.8 µg/ml or 4.43×10^{13} DNA molecules/ml.

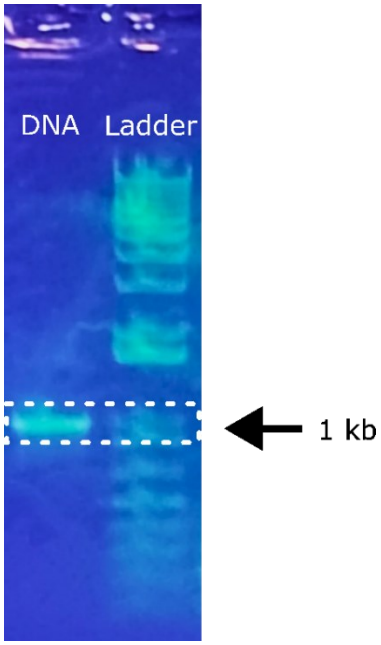

Figure E-2 DNA agarose gel Approach A.
This image shows the electrophoresis gel results of the 1 kbp DNA used in approach A. The left column has the PCR product and the right column has the DNA ladder.

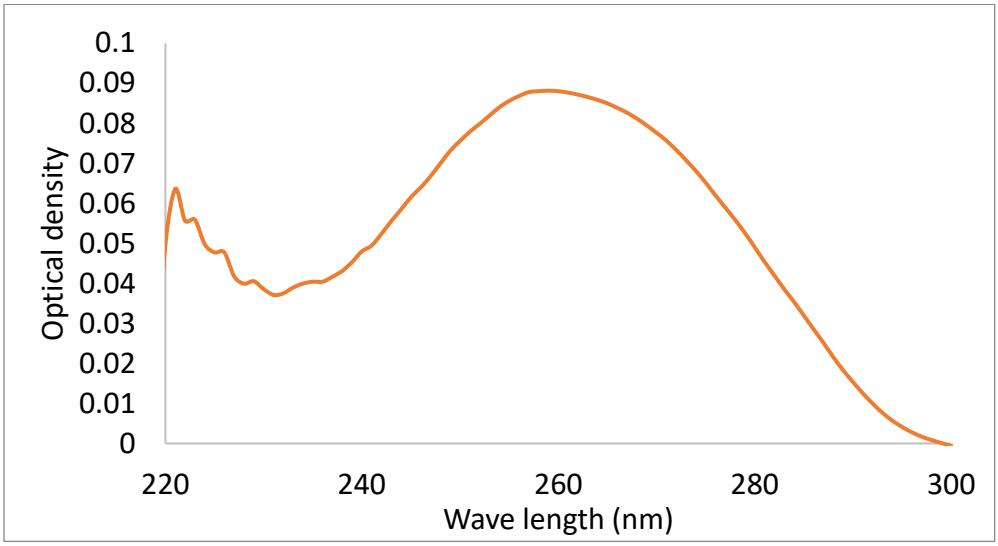

Figure E-3 DNA spectra Approach B.
This graph shows the spectrum for the 2 kbp DNA used in Approach B. For this sample the ratios between the relevant peaks are $\frac{I_{260}}{I_{280}} = 1.79$ and $\frac{I_{260}}{I_{230}} = 2.47$. This spectra was also used to calculate the DNA concentration, giving 1765 µg/ml or 8.154x10^{14} DNAs/ml.

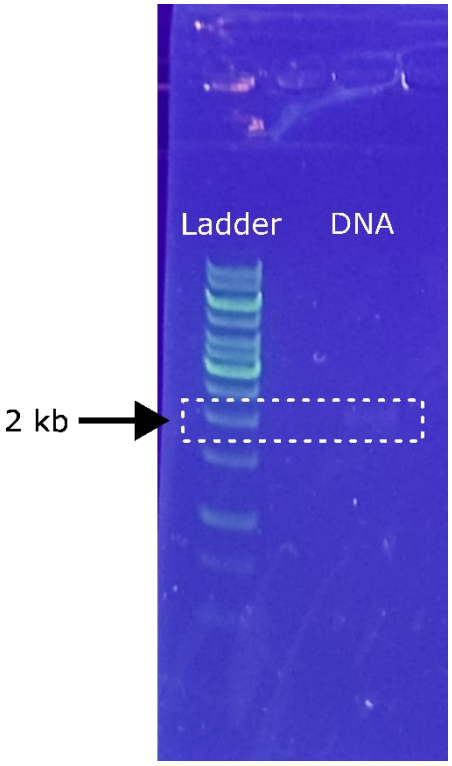

Figure E-4 DNA agarose gel Approach B.
This image shows the electrophoresis gel results of the 2 kbp DNA used in approach B. The right column has the DNA and the left column has the DNA ladder.

Appendix F.

Additional information about bead height detection

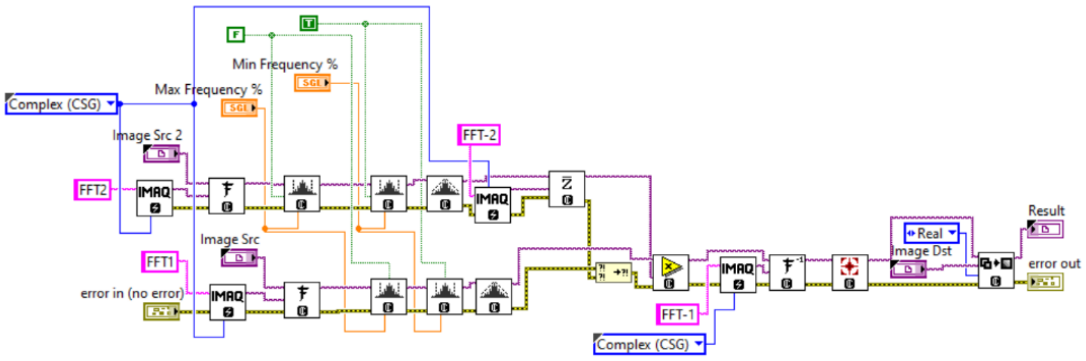

Figure F-1 Cross-correlation LabVIEW.
The two inputs are an image of a bead (Image Src) and an image of the same bead at a later time (Image Src 2). Both images are transformed using a Fast Fourier Transform (FFT) into complex images. The resulting images are then processed by applying low and high pass filters followed by attenuation. The complex conjugate of Image Src is then multiplied by Image Src 2. The product is transformed back using an inverse Fast Fourier Transform (FFT^{-1}), and the frequencies are inverted. Finally, the real part of the resulting image is used to proceed with the next steps.

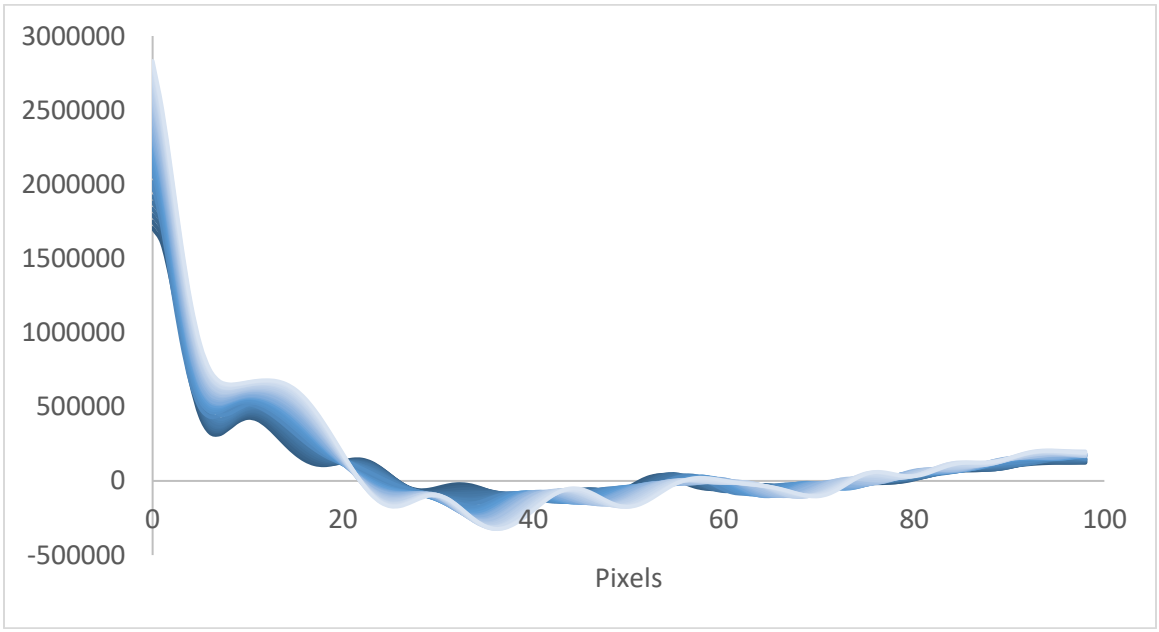

Figure F-2 Radial profile of diffraction patterns used in calibration.
This plot shows the radial profiles of a bead at different heights separated by 100 nm from the objective lens in a 2.8 µm range. The darkest color is the closest distance to the objective and the lightest color is the furthest away distance. The y-axis is the real part of the diffraction pattern of

the bead after being processed using FFT and transformed back to real space using FFT^{-1}. The center of the bead was found as described in section 4.1.1.

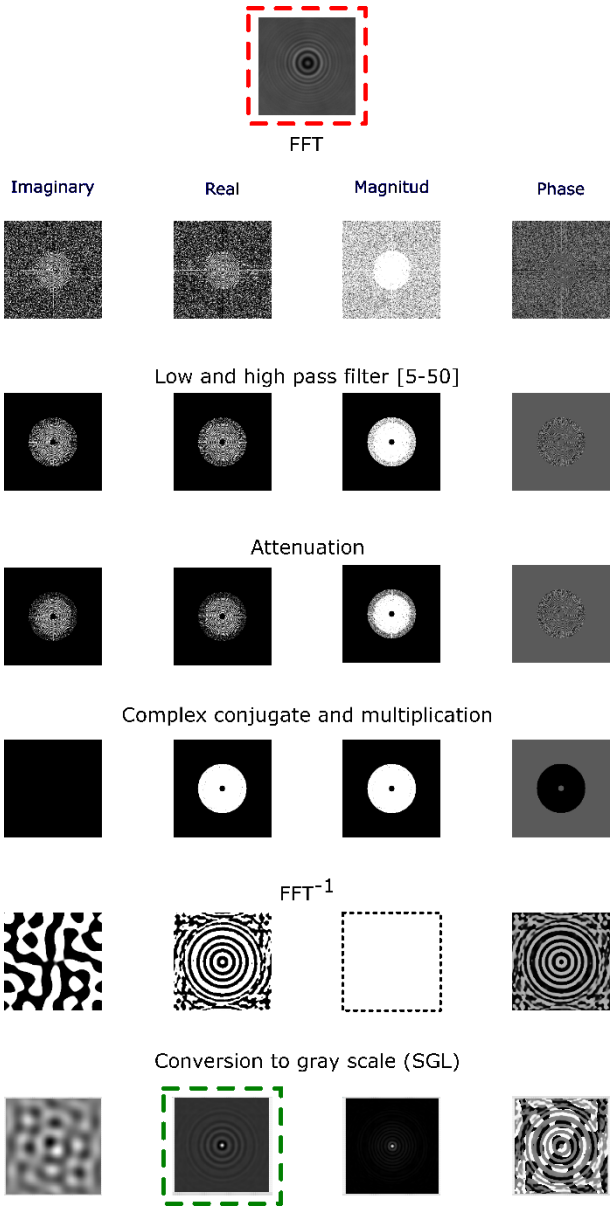

Figure F-3 Image processing in reciprocal space.
Steps of image processing that occur in the Poirier lab's RMS algorithm used to analyze the diffraction pattern of the beads. I am depicting this using 8-bit images in grayscale. The original image (top, red box) is transformed using a Fast Fourier Transform (FFT) into a complex image that has an imaginary part, real part, magnitude, and phase. The subsequent transformations include applying low and high pass filters (in this case, 5 to 50% of the full range of frequencies), followed by attenuation that reduces the intensity of the pixels in the image to reduce the impact on glare. The image is then multiplied by its complex conjugate and transformed back using an inverse Fast Fourier transform (FFT^{-1}). Finally, the Image is transformed into an SGL grayscale image (each pixel values is stored as 32-bit floating-point numbers) and the real part (bottom, green box) is used to continue with the next steps.

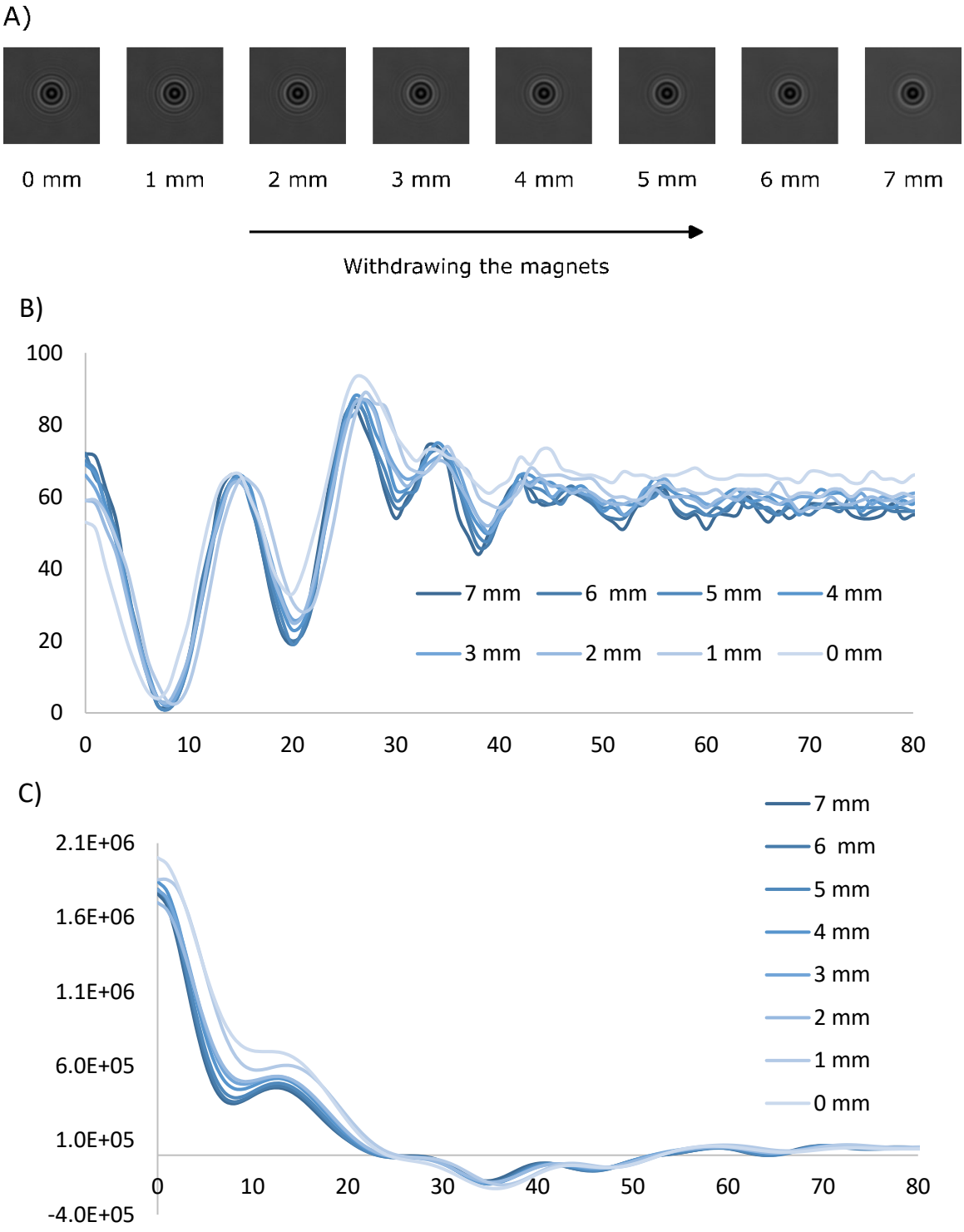

Figure F-4 Bead diffraction pattern re-scaled different magnet heights.
A) Images of the full re-scaled ROI when the magnets are withdrawn. B) Radial profile of diffraction pattern of the beads at different magnet heights. The radial profile was extracted by manually selecting the bead's center and plotting the line of pixels to the right of that center from the raw images. The x-axis represents pixel distance, and the y-axis represents pixel intensity.. C) Radial profile of the bead diffraction pattern after processing in the reciprocal space. The bead's center was determined using the algorithm described in Section 4.1.1. The x-axis

represents pixel distance, and the y-axis represents the real part of the image after transforming back to real space using the inverse Fourier transform.

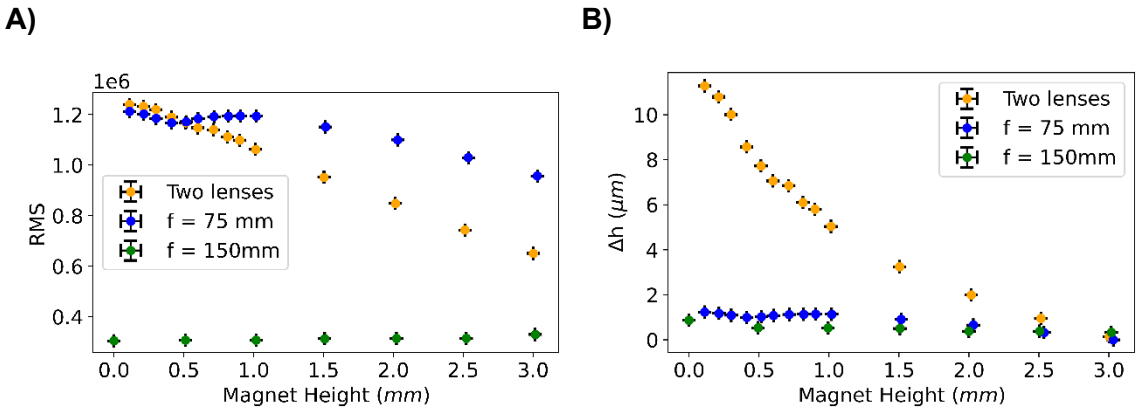

Figure F-5 RMS and bead height at different magnet heights for original and one-lens illuminations.

A) RMS for the original light illumination (two lenses) compared to the configurations using just one converging lens of *f*=75 mm and *f*=150 mm. B) Change in terms of measured bead height (Δh) at different magnet heights. *h*=0 is where the calibration curve was done, in this case *h*=3 mm. This experiments only spam a magnet movement of 3 mm, rather than 7 or 8 mm as like the others.

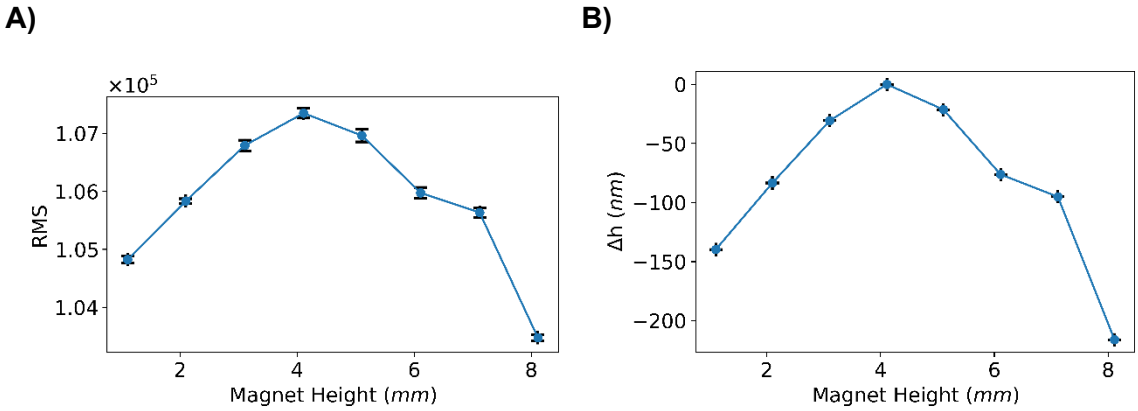

Figure F-6 RMS and RMS and bead height at different magnet heights for re-scaled ROI and two-lens and iris illumination.

This experiment was done by rescaling the intensities of the bead images from 0 to 100 before processing in the Fourier space, the new illumination configuration was used with the iris 2 mm wide. A) RMS change with magnet height and B) Change in terms of measured bead height (Δh) at different magnet heights. *h*=0 is where the calibration curve was done, in this case *h*=4 mm.

Appendix G.

LabVIEW code information

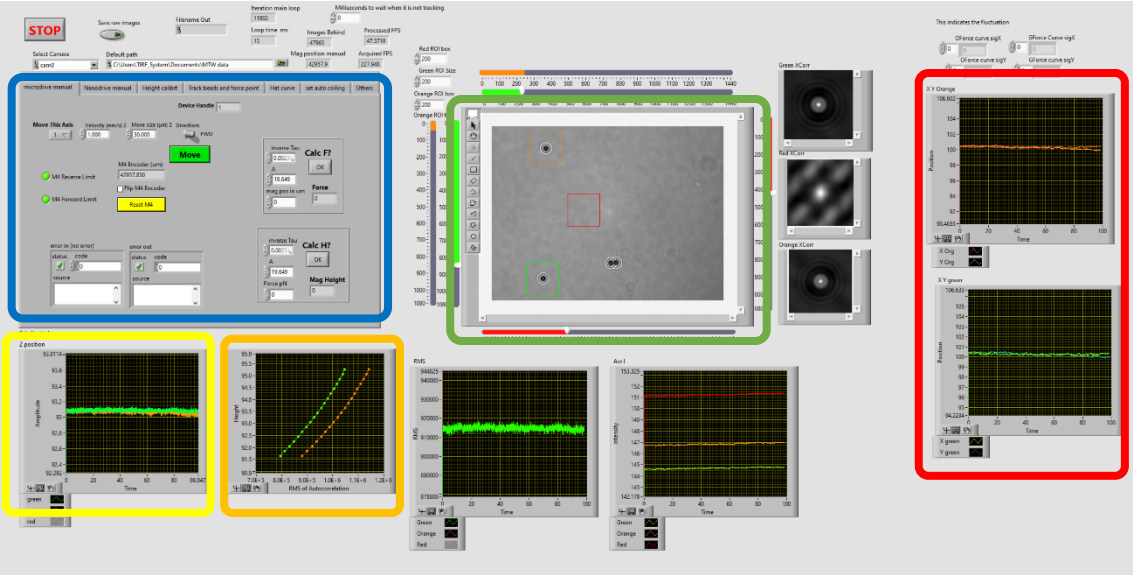

Figure G-1 LabVIEW program using RMS to measure extension of the polymer. `Magnetic Tweezers for Instrument final RMS and record.vi`. This program allows you to extract the necessary information to calculate the force exerted to a tethered bead. It was provided from Michael Poirier at Ohio State University, via Maria Mills at the University of Missouri. The beads in the field of view (green box) are selected by moving the regions of interest. The program is written so that the red ROI is to track the bead that would work as a fiduciary bead. There is a control part of the program (blue box) where you can control the different parts of the instrument like step motors and piezo stages, also to create a calibration curve as shown in the orange box, and to track the bead positions as shown in the plot in the red box (*x,y*) and yellow box (*z*). Several parameters can be adjusted, including the high and low bandpass filters for the Fourier process, the size of the ROIs, how many micrometers the piezo will move to create the calibration curve, the number of points per micrometer in the calibration curve, and the polynomial degree used to fit the calibration curve. Additionally, this program allows you to save the raw data of the whole field of view, and of the ROIs for calibration images and images of the current experiment.

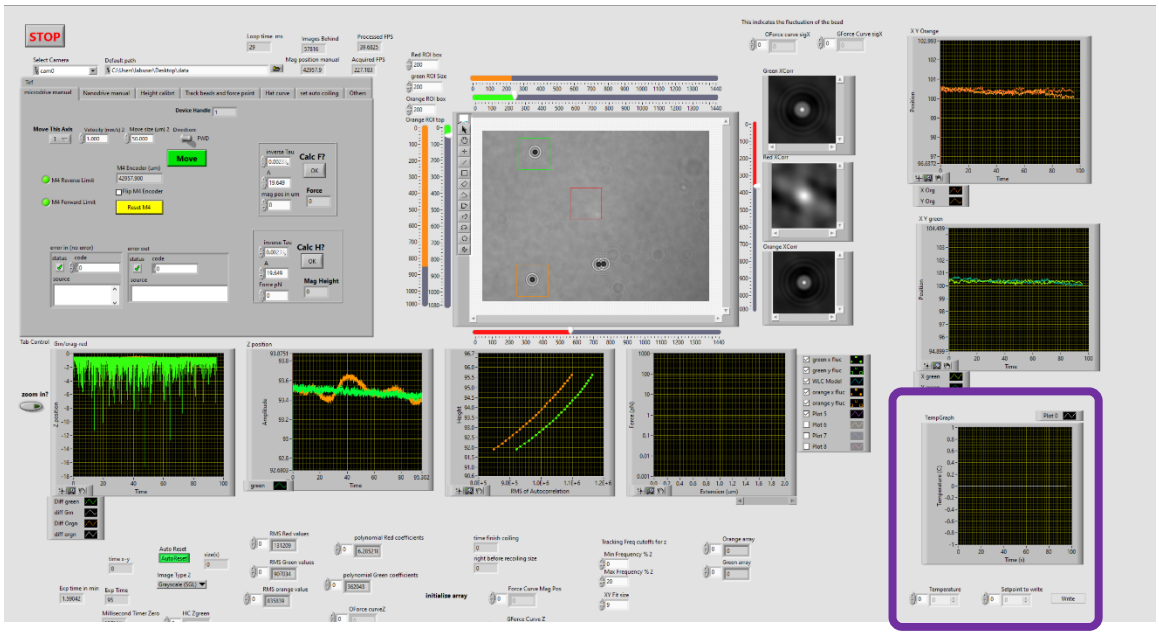

Figure G-2 LabVIEW program with temperature chamber incorporated.
`Magnetic Tweezers instrument with temperature control.vi`. The same program as in Figure G-1, but I include the temperature control. The temperature can be set and monitored (purple box). I wrote this part of the code.

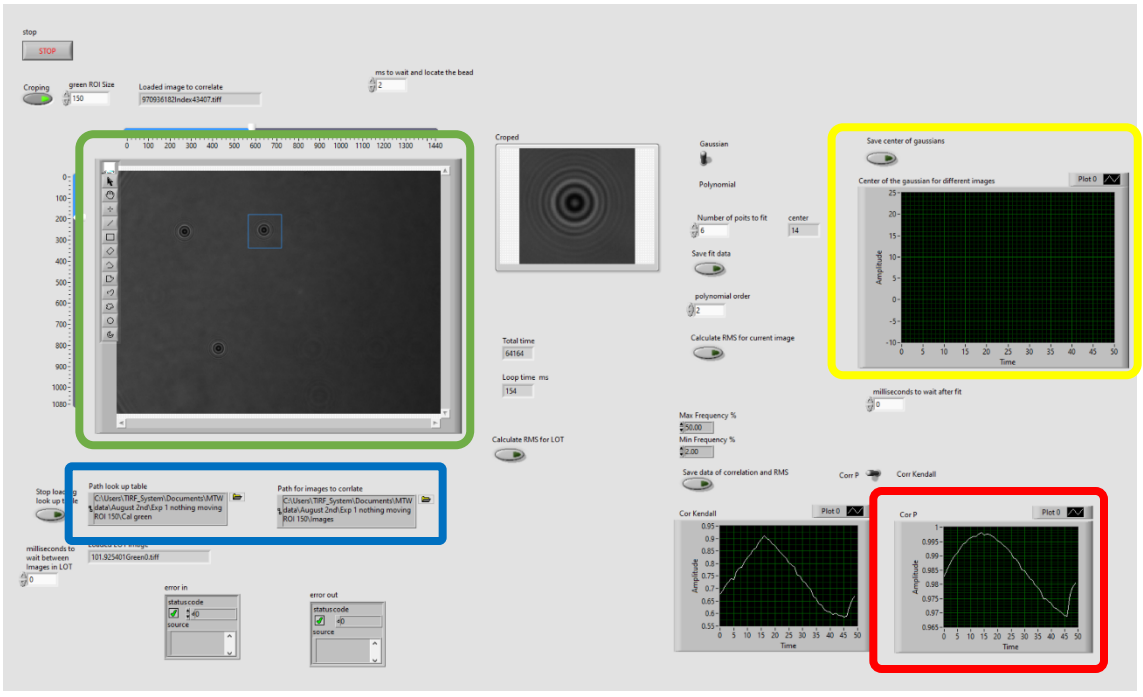

Figure G-3 LabVIEW program of correlation algorithm to measure height.
`Correlation algorithm final.vi`. In this program, written by me, you first select the images that will serve as the LUT, followed by the set of images containing beads of unknown heights for analysis (blue box). The program enables you to select the specific bead to be

analyzed from the full field of view (green box). It then displays the correlation between the image in the ROI and the LUT images (red box). Several parameters can be adjusted, including the high and low bandpass filters for the Fourier process, the type of function (Gaussian or second-degree polynomial), and the number of points around the maximum correlation to be fitted. Once all images have been processed, the center of the fitted function is displayed (yellow box). Additionally, this program allows you to save data such as the radial profiles of both the LUT and the bead under analysis, the full correlation, the points near the maximum correlation, the corresponding fitted function, and the center of the fitted function for each bead.

A) **B)**

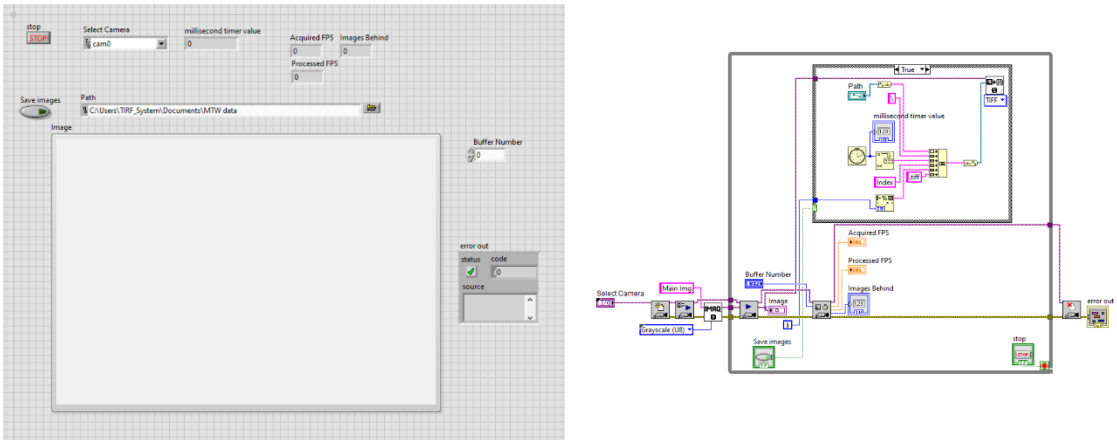

Figure G-4 Lab VIEW program to record images from the camera.

`Saving images.vi`. This shows a small program I wrote that simply captures images from the camera. This allows it to record images at close to the maximum speed at which the camera can capture them (~220 frames per second).